Physical Processes Governing Ocean Heat Content Variability

University of Rome Tor Vergata

PhD in Physics
Coordinator: Massimo Bianchi
XXXIV Cycle

Candidate

Vincenzo de Toma
ID number 0272642

Thesis Advisors

Prof. Luca Biferale
Dr. Vincenzo Artale
Dr. Alessandra S. Lanotte

Academic Year: 2020/2021 - March 10, 2022

Thesis defended on 30th March 2022
in front of a Board of Examiners composed by:

Prof. Luca Biferale (University of Rome Tor Vergata) (chairman)
Dr. Federico Falcini (Institute of Marine Sciences CNR-ARTOV-ISMAR)
Dr. Gianmaria Sannino (Research Center ENEA Casaccia)
Dr. Vincenzo Artale (Research Center ENEA Frascati)
Dr. ssa Alessandra Sabina Lanotte (CNR Nanotec of Lecce)

Physical Processes Governing Ocean Heat Content Variability
Ph.D. thesis. Tor Vergata – University of Rome
ISBN: N.A.

This thesis has been typeset by LaTeX and the tvthesis class.

Version: March 10, 2022

Author's email: vincenzodetoma.vdt@gmail.com

This PhD Thesis is dedicated to
My Sister Paolina,
who just always got my back,
My Mother Francesca and My Father Tommaso,
who have never had a doubt on my success,
and to the beloved Stefania,
who gave me strength in all good and bad times.

Abstract

This thesis summarizes the research program of the XXXIV PhD cycle of University of Rome Tor Vergata, falling within the European Union Project *Copernicus Climate Change Service C3S_511: Quality Assessment of Essential Climate Variable (ECV) Products.*

The general objectives of this project regards the validation of all the data, both observed or simulated by climate models available through the C3S Climate Data Store (CDS). To pursue this aim, the project should have applied analysis methodologies already partly developed, such as the Earth System Model Validation Tool (ESMValTool), to evaluate statistical averages, climate variability, uncertainty evaluation, ability to capture extreme events. In one word to assess the suitability of available data to identify changes and variability of the Earth climate system, through the production of IPCC-style Assessment Reports (IPCC stands for Intergovernmental Panel on Climate Change) [1].

In the first part I will go through the definition, description, current understanding and evaluation of the Atlantic Meridional Overturning Circulation in state-of-art ocean reanalyses.

The focus will be on describing and interpreting an ocean circulation regime change characterizing one of the data sets, proposing a mechanism to explain the observed variability[2]. In particular, we find out that state-of-the-art reconstructions show signs of a reduction in the northward transport of watermasses, reflecting the possible existence a stronger circulation regime prior to mid-1990s, and a weaker one afterwards. We explored the effects of these circulation changes on key components of the ocean climate, finding a tilt of the Gulf Stream Path toward lower latitudes passing from one period to the other, consistently with diminished Deep Water Formation in high latitude seas. Finally, observing the correlation with the North Atlantic Oscillation index we proposed a mechanism by which it is possible to interpret this ocean variability as a response to a persistent atmospheric perturbation. We also argue that this response appear overamplified in two of these datasets, and probably the flux-adjustment carried out in order to reduce Sea Surface Temperature biases along the Gulf Stream front is among the causes for this[3].

Indeed, given the limitations in computational power of current High Performance Computing facilities, the resolution of global general circulation models (GCM) is still limited to about 25 km for the ocean component, which implies that all physical

[1] I know that these activities are not strictly connected to the objectives of this manuscript, but still I would like to stress the importance of validation step when using data for scientific purposes - indeed our efforts have been summarized in a publication: *Yang, C., Leonelli, F. E., Marullo, S., Artale, V., Beggs, H., Nardelli, B. B., Toshio M. Chin, Vincenzo de Toma, ... & Pisano, A. (2021). "Sea Surface Temperature Intercomparison in the Framework of the Copernicus Climate Change Service (C3S)". Journal of Climate, 34(13), 5257-5283.*

[2] On this topic I presented a poster at the European Geophysical Union - *de Toma, V., Yang, C., & Artale, V. (2020, May). "Climate shift of the Atlantic Meridional Overturning Circulation (AMOC) in Reanalyses (ORAS5): possible causes, and sources of uncertainty". In EGU General Assembly Conference Abstracts (p. 3461).*

[3] This work has been summarized into a publication, which is currently under review - *de Toma, V. Yang, C., & Artale, V. (submitted to MDPI Climate) "Exploring AMOC Regime Change Over the Past Four Decades through Ocean Reanalyses"*

processes below the grid spacing must be parameterized, in order to account for their average effect on the whole grid cell - this is a primary cause for biases in circulation features.
Given this non negligible aspect, vast uncertainties still remain about the effects of small scale processes in large scale dynamical features of the ocean, and this is an open research topic in the scientific community. There are two ways to tackle this problem: one is to deal directly with a general circulation model and study with sensitivity experiments the effect of choosing a certain scheme for sub grid physics; an other approach could be to study the effect of smaller scales in a numerical setup which is able to focus directly those scale of motions which have to be parameterized in an ocean GCM.
In a nutshell, this second approach motivate the last part of the thesis, in which I will describe a more general and theoretically oriented study on rotating stratified turbulence in an ideal, thin, tri-periodical box (which should be close to represent an open-ocean domain), without including the effect of topography.
Namely the aim is to disentangle the relative role of waves with respect to vortices, and one possible way to do it is to employ a linear eigenmode decomposition introduced by Peter Bartello in 1996. We studied a recent version of Bartello's approach, using it to selectively forcing only waves, or only vortices in the system under investigation from the beginning.
Aiming to understand how the energy is partitioned amongst these modes, especially when different forcing projections (which will excite only waves or vortices) are used, this approach would help to characterize respectively the importance of rotation or stratification to nonlinear terms while varying their corresponding dimensionless parameters[4]; then, in a future development it will be possible to explore where and why one particular setup gets close to real ocean conditions. Conclusions and a trace of my future line of scientific investigation will follow.

[4]In this regard there's a paper in preparation - *Lanotte, A., S., Lvov, Y., Biferale, L., Artale, V., de Toma, V., - "Wave-Vortex Energy Repartition for Rotating Stratified Turbulence in Slab Domains" (in prep.)*

Acknowledgments

I remember well the first meeting with Dr. Vincenzo Artale and Prof. Luca Biferale. One of the clearest memories are the words of Luca: "usually we set up the PhD leaving a high level of autonomy to the student, in the hope to help him finding by himself satisfaction in the research project: if, on one hand this choice can be a good experience, on the other hand it can be a disastrous shipwreck". If on one side these words let me with a sense of happiness in front of this opportunity to become a researcher, on the other side I had also a little sense of uncertainty about my capacities to overcome the future difficulties inside my stomach. At the end of this path I can surely say that without the precious help of my supervisors I would never have reached this point.

Thanks also to the other people I met during these three years, which supported and withstood me, such as Dr.ssa Chunxue Yang, which I want to thank not only for all the fruitful scientific discussions, but also for your kindness, comprehension and humanity; now more than ever you taught me the importance of sometimes leave aside for a moment the work and just asking "is everything ok?".

Another huge thanks goes to the group which is forming at CNR: Andrea Storto, Yassmina Mahmoud, Davide Cavaliere, Eva Le Merle, Jacopo Busatto; it's not take for granted that in a weekly discussion everyone makes the effort to join with suggestions in the work of the others. Moreover, also the experience with C3S reports have been of great value for me, I've understood how research sometimes need also technical validation and assessment work: thanks to Francesca Elisa Leonelli, Andrea Pisano, Salvatore Marullo, Emanuele Organelli, Marco Bellacicco, Jaime Pitarch, Rosalia Santoleri for sharing the efforts.

Part of my gratefulness goes to the guys in and out of the PhD room. Without Alfredo Grillo, Dario Consoli, Francesca Pelusi, Fabio Guglietta, Guilherme Goedert (I remember with pleasure the time spent together at Les Houches School of Physics - thanks my friend), Lokahith Agasthya, Augusto Mellini, Alice Aldi, Maurizio Firrotta, Fabio Bonaccorso, Martino Scarpolini, Gianmarco Parise, the department of physics of University of Rome Tor Vergata would be only an ugly yellow-gray institute without any sense of existence.

A special thought goes to Alessandra Sabina Lanotte. We met in a period where I felt like I lost a bit in the middle of nowhere: the more theoretical problem we are facing reminded me some of my origins as theoretical physicist. We met just once because of CoViD-19, but I remember with pleasure our brainstormings and skype calls, often delayed by other urgencies and at the same time always useful. "Our work has to be a pleasure, not a nightmare. If it stresses you, it's better you stop a moment. Try also to find your breath from troubles of real life in your work" - your words have been precious to keep going on, I will treasure them.

Another acknowledgment goes to Prof. Yuri Lvov, with whom I had the pleasure to discuss with during our meetings with Dr.ssa Lanotte, Prof. Biferale and Dr. Artale. Michele Feyles, Andrea De Cosmo and Leticia Maria, Augusto Mellini, Yacopo Damizia, Federico Centrone, Anita Camillini, Alberto Orellana, Giacomo Scettri: there are no words to express the time together, which has been food for my soul and for my mind - I love you guys!

To be short, I will gather here also other people which are not aware of the role they had in my path: thanks to the fiends of youth, Andrea Vellucci, Alessia Di Tota and Michele Sparano, Giancarlo Manca and Silvia Sforza. Not of least importance also all my martial friends from Sakitama Dojo: Sensei Valter Francia, Sensei Isabella Folletti, Jury and Fiorenza, Sorcio and Susanna, Gazzella and Silvia, Mauro, Fabio, Valentina, Michele, Alberto: as my second family, your support is priceless - you have always taught me how to stand up after a fall.
Another very special aknowledgment to the Innocenzi family: thanks to the young Vittorio, whose birth woke me up on Sunday morning at 5 am, Jacopo and Miriam, because I'm always a little child when I'm with you, Martina and Luigi, Flavia, Giovanna and Fiero, Maria, Osvaldo and Assunta.
A special thanks also to all my family who supported me in every moment of this adventure: Tommaso and Francesca, for being my safe place in all the turbulence offered by life, Paolina, because I'm always available to you as you will constantly be present to me, as any brother and sister do. Thanks also to Stefano, Angela, Gigi, Silvia, Andrea, Gaia, Valentina, Giuseppe, Edoardo Giovanni, Mary, Franco, Antonio, Arianna, Paolo, Malwina, Aurelia, Paolina, and also to who will stay always in my heart, Gioacchino, Vincenzo and Concetta.
Thanks also to Lorenzo for all the good moments together which gave me rest from the work. Many thanks also to all friends met thanks to Stefania: Pietro, Marianna, Alfredo, Giulia, Lucio, Erica, Ludovico, Giulia, Federica.
In the end, last but definitely not least, to the woman my heart belongs to: Stefania, we began our life together almost by accident, then we stayed side by side facing good as well as bad times, and I can't wait to build my family with you - thanks for all your love, support, endurance and patience with me. Beside you I realize that I had to pursue this achievement for myself and not for other people surrounding me. Sorry to delay the beginning of the manuscript with these goofy acknowledgment, but they were absolutely necessary. Thanks for the attention and have a good reading!

Ringraziamenti

Ricordo bene il primo incontro con il Dr. Vincenzo Artale e il Prof. Luca Biferale. Uno dei ricordi più chiari è legato alle parole di Luca: "di solito noi impostiamo il dottorato lasciando un'ampia autonomia al dottorando, nella speranza di aiutarlo in questo modo a trovare la soddisfazione nel progetto di ricerca: se questo da una parte può essere un bene, dall'altra può rivelarsi un disastroso naufragio". Se da un lato queste parole mi lasciarono all'epoca con un senso di felicità di fronte a questa opportunità di diventare un ricercatore, dall'altro lato avevo in fondo al mio stomaco anche un senso di incertezza riguardo le mie capacita di superare le future difficoltà. Alla fine di questo percorso posso dire con certezza che senza il prezioso aiuto dei miei supervisori non avrei mai raggiunto questo punto.
Grazie anche alle altre persone che ho incontrato durante questi tre anni, che mi hanno supportato e sopportato, come la Dr.ssa Chunxue Yang, che vorrei ringraziare non solo per tutte le fruttuose discussioni di carattere scientifico, ma anche per la sua gentilezza, comprensione e umanità; ora più che mai mi ha insegnato l'importanza di tralasciare a volte per un momento le questioni lavorative per chiedere semplicemente

"è tutto ok?".
Un altro grosso ringraziamento va al gruppo che si sta formando attorno a lei al CNR: Andrea Storto, Yassmina Mahmoud, Davide Cavaliere, Eva Le Merle, Jacopo Busatto; non è per niente scontato che nelle discussioni settimanali ogniuno tenti di entrare nel lavoro del suo collega offrendo suggerimenti costruttivi come quelli che ci siamo dati. In più, anche l'esperienza con i report del progetto C3S è stata di grande valore, non solo formativo, per me; ho capito come la ricerca abbia bisogno a volte anche di aspetti tecnici come la validazione e valutazione dell'adeguatezza dei dati: grazie allora a Francesca Elisa Leonelli, Andrea Pisano, Salvatore Marullo, Emanuele Organelli, Marco Bellacicco, Jaime Pitarch, Rosalia Santoleri per la condivisione degli sforzi.
Parte della mia gratitudine va ai ragazzi della stanza dei PhD. Senza Alfredo Grillo, Dario Consoli, Francesca Pelusi, Fabio Guglietta, Guilherme Goedert (Ricordo con piacere il tempo speso assieme alla Scuola di Fisica di Les Houches - grazie amico mio), Lokahith Agasthya, Augusto Mellini, Alice Aldi, Maurizio Firrotta, Fabio Bonaccorso, Martino Scarpolini, Gianmarco Parise, il Dipartimento di Fisica dell'Università di Roma Tor Vergata sarebbe solo un brutto edificio giallo-grigio senza alcuna ragion d'essere.
Un pensiero speciale va ad Alessandra Sabina Lanotte. Ci siamo incontrati in un periodo in cui mi sentivo un pò in mezzo al nulla: il problema di carattere più teorico che stiamo affrontando mi ha ricordato in qualche modo le mie origini di fisico teorico. Ci siamo incontrati solo una volta a causa del CoViD-19, ma ricordo con piacere le riflessioni e le chiamate skype, spesso ritardate da altre urgenze, ma sempre utili. "Il nostro lavoro deve essere un piacere, non un incubo. Se ti stressa, è meglio che ti fermi un momento. Ricorda però anche che a volte il lavoro può offrirti, quando è sano, una buona occasione per respirare in mezzo ai guai della vita vera" - le tue parole sono state preziose per continuare, e quindi ne farò tesoro.
Un altro ringraziamento va al Prof. Yuri Lvov, con cui ho avuto il piacere di discutere durante i nostri incontri con la Dr.ssa Lanotte, il Prof. Biferale e il Dr. Artale.
Michele Feyles, Andrea De Cosmo e Leticia Maria, Augusto Mellini, Yacopo Damizia, Federico Centrone, Anita Camillini, Alberto Orellana, Giacomo Scettri: non ci sono parole per esprimere il tempo insieme, che è stato fonte di nutrimento per l'anima e la mente - Vi amo ragazzi!
Per cercare di essere breve, raccoglierò qui anche qualche persona non conscia del ruolo avuto nel mio cammino: grazie agli amici della giovinezza, Andrea Vellucci, Alessia Di Tota e Michele Sparano, Giancarlo Manca e Silvia Sforza. Di non minore importanza anche tutti gli amici marziali del Sakitama Dojo: Sensei Valter Francia, Sensei Isabella Folletti, Jury e Fiorenza, Sorcio e Susanna, Gazzella e Silvia, Mauro, Fabio, Valentina, Michele, Alberto: come la mia seconda famiglia, il vostro supporto è senza prezzo - mi avete sempre insegnato a rialzarmi in piedi dopo una caduta.
Un altro ringraziamento molto speciale alla famiglia Innocenzi: in breve grazie al giovanissimo Vittorio, la cui nascita ci ha svegliato di Domenica alle 5 di mattina, Jacopo e Miriam, perchè ricordo cosa vuol dire tornare bambino quando sono con voi, Martina e Luigi, Flavia, Giovanna e Fiero, Maria, Osvaldo e Assunta.
Un grazie speciale anche a tutta la mia famiglia che mi ha supportato in ogni momento di questa avventura: Tommaso e Francesca, per essere il mio posto sicuro in tutta la turbolenza offerta dalla vita, Paolina, perchè sono sempre disponibile per te come

tu lo sarai per me, come solo fratello e sorella sanno fare. Grazie anche a Stefano, Angela, Gigi, Silvia, Andrea, Gaia, Valentina, Giuseppe, Edoardo Giovanni, Mary, Franco, Antonio, Arianna, Paolo, Malwina, Aurelia, Paolina, e anche a chi sarà nel mio cuore sempre, Gioacchino, Vincenzo e Concetta.
Grazie anche a Lorenzo per tutti i buoni momenti insieme che mi hanno offerto tregua dal lavoro. Molte grazie anche a tutti gli amici incontrati tramite Stefania: Rita, Pietro, Marianna, Alfredo, Giulia, Lucio, Erica, Ludovico, Giulia, Federica.
Infine, ma non definitivamente meno importante, alla donna a cui appartiene il mio cuore: Stefania, abbiamo iniziato a vivere insieme quasi per un caso (s)fortuito, poi siamo rimasti fianco a fianco affrontando i buoni come i cattivi tempi, e non vedo l'ora di costruire la mia famiglia con te - grazie per tutto il tuo amore, il tuo supporto, la tua sopportazione e la tua pazienza con me. Accanto a te ho realizzato che dovevo raggiungere questo conseguimento per me stesso in primis, e non per le persone che mi circondano. Scusate se vi ho tediato con questi goffi ringraziamenti, ma erano assolutamente necessari. Grazie per l'attenzione e buona lettura!

Contents

List of Tables

List of Figures

Acronyms

3D-FGAT 3D First Guess at Appropriate Time. 20

AABW Abyssal Antarctic Bottom Water. 8

AMOC Atlantic Meridional Overturning Circulation. viii, x–xiii, 5, 7–16, 19–22, 25–27, 29–34, 36–41, 45, 46, 72

C3S Copernicus Climate Change Service. iii, iv, vi, 18, 25, 41

CDS Climate Data Store. iii

CGLORS Cmcc GLobal Ocean Reanalysis System. 21

CICE Community Ice CodE, ice model from Los Alamos. 21

CMEMS Copernicus Marine Environmental Monitoring Service. viii, xiii, 18, 20, 23, 37, 41

CTD Conductivity, Temperature and Depth. xi, 3, 21

DWF Deep Water Formation. viii, 9, 10, 14, 30, 33, 34, 36, 38, 39, 45, 46

ECMWF European Center for Medium Weather Forecast. viii, 4, 18, 20–22, 26

ECV Essential Climate Variable. iii, 22

EOF Empirical Orthogonal Function. viii, xii, 22, 23, 28–32, 34, 36, 45

EOS Equation Of State. 2

ERSSTv5 Extended Reconstructed Sea Surface Temperature version 5. xii, 28

ESA European Space Agency. 3

FOAM Forecast Ocean Assimilation Model. 21, 42, 44

GCM General Circulation Model. iii, 5, 14, 46, 56, 61

GIN Greenland-Iceland-Norwegian. 27, 33, 34, 36

GLORYS GLobal Ocean ReanalYsis and Simulation. 21

GPE Gravitational Potential Energy. 38

GREP Global Reanalysis multi-model Ensemble Product. viii, 20, 21, 25, 37, 41

HPC High Performance Computing. 72

IPCC Intergovernamental Panel on Climate Change. iii

KE Kinetic Energy. xiii, 38, 39

LIM2 Louvain-la-nueve Ice Model version 2. 20, 21

MBT Mechanical BathyTermographs. xi, 3, 20

MDT Mean Dynamic Topography. 21

MEOP-CTD Marine mammals Exploring Oceans Pole to pole CTD. 3

MLD Mixed Layer Depth. xiii, 19, 34, 35

NADW North Atlantic Deep Water. xi, 7, 14, 15, 36

NAO North Atlantic Oscillation. xiii, 5, 19, 30, 31, 33, 34, 36, 39, 45

NCEP/NCAR National Centers for Environmental Prediciton / National Center for Atmospheric Research. 3

NEMO Nucleus European for the Modeling of the Ocean. 4, 5, 20, 21, 56, 72

NEMOVAR NEMO VARiational data assimilation scheme. 20, 22

OGCM Ocean General Circulation Model. 72

OHC Ocean Heat Content. viii, xii, xiii, 19, 23–25, 28–31, 41–46

OHT Ocean Heat Transport. 16, 17

ORAS4 Ocean Reanalysis Analysis System 4. viii, xii, xiii, 20–22, 25–27, 33, 34, 45

ORAS5 Ocean Reanalysis Analysis System 5. viii, xii, xiii, 18, 20, 21, 23, 25–30, 32, 33, 35–37, 39, 41, 45, 72

PC Principal Component. xii, 23, 28–32, 36

RAPID-MOCHA Rapid Climate Change - Meridional Overturning Circulation and Heatflux Array. viii, xii, 19, 20, 22, 25–27, 41

SAMBA South Atlantic Moc Basin-wide Array. viii, 20, 22, 26

SIC Sea Ice Concentration. 21

SKE-EEs Surface Kinetic Energy - Extreme Events. 38, 39

SODA Simple Ocean Data Assimilation. viii, xii, xiii, 21, 25, 26, 33, 34, 45

SPG Sub Polar Gyre. 33, 36, 45

SSS Sea Surface Salinity. 21

SST Sea Surface Temperature. viii, xii, 20, 21, 24, 28–31, 39, 45

TEOS Termodynamic Equation Of Seawater. 2

TKE Turbulent Kinetic Energy. 21

USA United States or America. 3

XBT eXpendable BathyTermographs. xi, 3, 20, 21

1

Introduction

"Begin at the beginning,"
the King said, gravely,
"and go on
till you come to an end;
then stop."

Lewis Carroll,
Alice in Wonderland

1.1 Dynamics of the oceans

Oceanic motions take place on a vast range of space and time scales, and they are the result of a complex interplay with atmospheric, radiative, turbulent and chaotic internal intrinsic variability. Their governing equations are primitive equations of geophysical fluid dynamics, whose aim is to describe all naturally occurring fluid motions. These are nonlinear partial differential equations involving all variables characterizing the ocean state, i.e. momentum, pressure, density, temperature, salt, with forcing factors as well, like atmospheric heat fluxes and wind stress at the ocean surface. Nonlinearities constitute the richness of this world: coupling different scales, they give rise to large scale structures (as vortices and meanders in major currents as Gulf Stream and Kuroshio, which are visible even from space), as well as to smaller scale processes (like wave-breaking, observable just by sitting on a beach). Despite the importance of boundary conditions such as topography and orography in constraining oceanic and atmospheric motions, Earth's rotation is the main factor that distinguishes geophysical flows from ordinary fluid motions, like the ones we can observe every morning stirring our cup of coffee. The rotating environment is responsible for the western-boundary intensification of oceanic wind-driven currents (Stommel (1948)). In the atmosphere, the combination of Earth's rotation, uneven distribution of land and water masses and the differential heating provided by the sun leads to the existence of Hadley, Ferrel and Polar convective cells (Vallis (2019)). Indeed large scale motions are commonly defined as those for which rotation is non-negligible (Pedlosky (2013)). In the ocean, the nonlinear equation of state, which

relates density (hence seawater's buoyancy) to temperature and salt, complicates the situation. Processes as air-sea interactions, differential heating of the globe, precipitation, river runoff, ice melt and evaporation contribute to modify the density distribution of water masses, leading to a long timescale circulation which commonly goes under the name of *thermohaline* circulation (i.e. the circulation regime driven by thermal and saline differences) (Broecker (1991)).
The seawater equation of state is the thermodynamical relationship whose determination descend from the first principle of thermodynamics applied to a parcel of fluid, and it has a long history of empirical derivations (Millero (2010)). From the theoretical and numerical point of view, it is often convenient to cast the density of seawater ρ into a nonlinear function of Absolute Salinity S_A, Conservative Temperature Θ and Geopotential Depth Z:

$$\rho = \rho\left(\Theta, S_A, Z\right) \tag{1.1}$$

The TEOS-10 EOS has been defined by the International Oceanographic Community in 2010 (IOC et al. (2015)), in substitution with the previous EOS-80 and has the main advantage of being consistent with Maxwell cross-differentiation relations. In theoretical studies and simplified numerical models, the use of a linear version of the EOS consists of neglecting the pressure/depth dependence, retaining a linear expression in term of temperature and salinity anomalies to reference values:

$$\rho \approx \rho_0 + \alpha\left(T - T_0\right) + \beta\left(S - S_0\right), \tag{1.2}$$

in which $\rho_0,\ T_0,\ S_0$ are reference values for density, temperature and salt, $\alpha = \partial\rho/\partial T,\ \beta = \partial\rho/\partial S$ are the *thermal expansion* and the *haline contraction* coefficients respectively. However, ongoing research shows that using a nonlinear polynomial form allows for the inclusion of effects due to nonlinearities (Roquet et al. (2015)), such as the Cabbelling effect (i.e. due to the curvature of density lines in the T-S diagram, it is possible sometimes to observe a water mass stemming from mixing processes which has density higher than its parent ocean parcels).
Another element that makes the ocean so important to climate variability is the large heat capacity of seawater C_p, which has a typical value of about $\sim 4000\ J/KgK$ in SI units (Talley (2011)). Through this high value, the ocean can absorb, store and transport an astonishing amount of heat, exerting a controlling role in climate and weather variability. Moreover, current estimates attribute more than 90% of anthropogenic heat storage to oceans (Meyssignac et al. (2019)).
Therefore, now more than ever, it is of paramount urgency to improve the current monitoring, understanding and modelling of the world ocean circulation.

1.2 In-situ, satellite and reanalysis data

Scientific exploration of the oceans has quite a long history, dating back to the first exploring voyages at the end of the eighteenth century, with the three principal expeditions of Captain James Cook between 1768 and 1780. In those and the following oceanographic campaigns, British naturalists observed winds, currents and subsurface temperatures, using methods that are in use still today, such as

Nansen bottles. The development of technology brought a great contribution to the ways in which we can retrieve ocean data, and today we have a very differentiated landscape of instruments, such as CTD, XBT, Argo floats, MEOP-CTD, and many others (Abraham et al. (2013), Treasure et al. (2017)). As a result of statistical optimal interpolation methods, it has been possible to have nearly gap-free ocean surface temperature data which date back to the 1860, gathering together sources of measurements which go from the so-called ship of opportunities (in remote times), to satellite data (Marullo et al. (2011)). An example of the historical development of subsurface temperature observations is depicted in figure 1.1, which displays the evolution of instruments deployment through the recent years. Remote sensing of

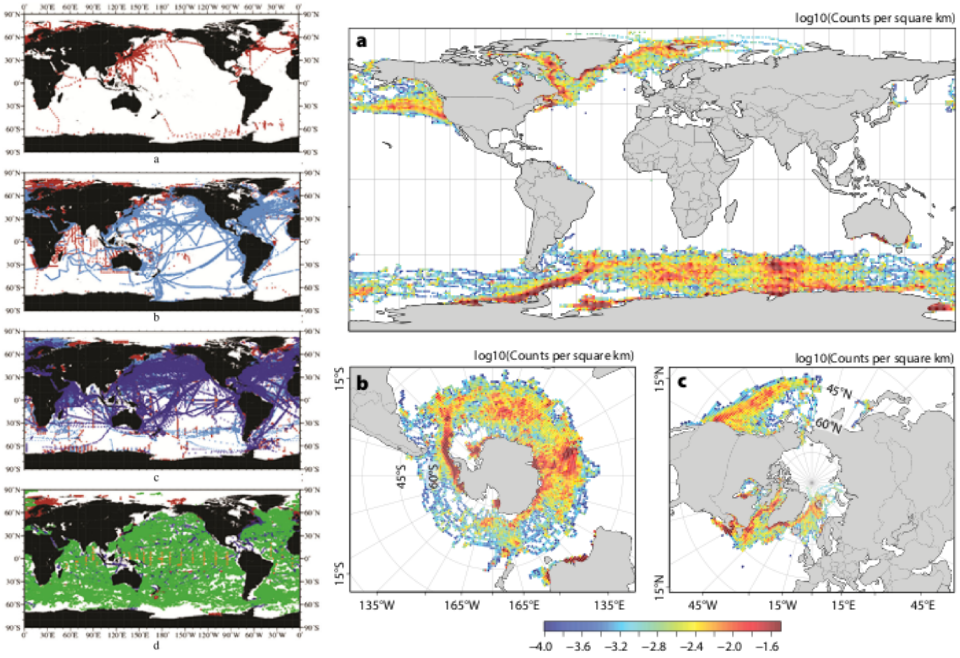

Figure 1.1. Left panel: (a), (b), (c), (d) show respectively the geographic distribution of subsurface temperature profiles for 1934, 1960, 1985, and 2009. Red = Nansen bottle or conductivity-temperature-depth (CTD), light blue = mechanical bathythermograph (MBT), dark blue = expendable bathythermograph (XBT), orange = tropical moored buoy, green = profiling float (figure from Abraham et al. (2013)); Right panel show the distribution of marine mammal-attached CTD from 2002 onward (figure from Treasure et al. (2017)).

the oceans started in the 1970s in the United States. The following decades (the 1980s and 1990s) saw Europe (through its European Space Agency - ESA) and Japan starting their missions, motivated by growing interest around USA programs success. A large number of ocean data from space is available nowadays as a heritage of those days. The sampling frequency and spatial accuracy are in a constant growth process (Martin (2014)).

Together with the development of both in-situ and satellite observations, in the 1990s, efforts within the National Centers for Environmental Prediction / National Center for Atmospheric Research (NCEP/NCAR) gave birth to the use of data assimilation to create uniformly gridded reconstructions of the evolving state of the

global atmosphere at time scales ranging from days to decades, which led to the first reanalysis dataset (Kalnay et al. (1996)). Reconstructing also air-sea momentum and heat fluxes, a side product of this effort was the ocean reanalysis, which then developed independently as the modern paradigm to combine in-situ, satellite and model data for reconstructing the ocean's past history (Lee et al. (2009), Balmaseda et al. (2013a)).

1.3 Governing equations: a modelling perspective

With the advent of ocean reanalyses (i.e. the assimilation of data into an ocean circulation model, which is used to provide a 4D spatially and temporally consistent ocean state reconstruction), even modelling details such as parameterizations of small scale physics, forcing factors, approximations and assumptions on any of the ingredients in governing equations became important. It seems worthwhile here to briefly introduce governing equations solved by the Nucleus European for the Modeling of the Ocean (NEMO), whose version 3.4 is at the core of the reanalysis data from the European Center for Medium Weather Forecast (ECMWF) treated in this thesis. As reported in its manual (Madec et al. (2017)), NEMO integrates primitive equations, which describe ocean behaviour at a good level of approximation. Primitive equations are Navier-Stokes equations equipped with a nonlinear equation of state coupling to fluid velocity two active tracers (here temperature and salt, but with coupled model it is possible to include also other tracers such as carbon dioxide or chlorophyll concentration), within the following additional assumptions:

1. spherical Earth approximation: geopotential surfaces are assumed to be spheres - meaning that gravity is everywhere perpendicular to the Earth's surface;
2. thin-shell approximation: compared to Earth's radius, ocean depth is negligible;
3. turbulent closure hypothesis: it is possible to describe the effect of small-scale processes with large scale terms;
4. Boussinesq approximation: density is assumed constant in every term except in the contribution to buoyancy force;
5. Hydrostatic hypothesis: vertical pressure gradient and buoyancy forces are in balance (need to parametrize convective processes);
6. Incompressibility condition: velocity of the fluid is divergence-free.

These assumption work pretty well for the ocean motions, especially because of its low aspect ratio: in particular, large scale ocean motions are almost horizontal, with the vertical velocities which are much smaller than horizontal components. In a coordinate system built upon an orthogonal set of unit vectors $(\mathbf{i}, \mathbf{j}, \mathbf{k})$ such that $\mathbf{k}$ is the local upward vector perpendicular to the Earth's surface and $(\mathbf{i}, \mathbf{j})$ lie along geopotential surfaces, the vector invariant formulation of primitive equations

provides the following system of six equations:

$$\frac{\partial \mathbf{U}_h}{\partial t} = -\left[(\nabla \times \mathbf{U}) \times \mathbf{U} + \frac{1}{2}\nabla \mathbf{U}^2\right]_h - f\mathbf{k} \times \mathbf{U}_h - \frac{1}{\rho_0}\nabla_h p + \mathbf{D}^{\mathbf{U}} + \mathbf{F}^{\mathbf{U}}, \quad (1.3a)$$

$$\frac{\partial p}{\partial z} = -\rho g, \qquad \nabla \cdot \mathbf{U} = 0, \qquad \rho = \rho\left(T, S, p\right), \quad (1.3b)$$

$$\frac{\partial T}{\partial t} = -\nabla \cdot (T\mathbf{U}) + D^T + F^T, \quad (1.3c)$$

$$\frac{\partial S}{\partial t} = -\nabla \cdot (S\mathbf{U}) + D^S + F^S. \quad (1.3d)$$

In the system of eqs. 1.3, the following notation has been used: $\mathbf{U} = \mathbf{U}_h + w\mathbf{k}$ is the three-dimensional velocity field (being $\mathbf{U}_h$, w the components on $(\mathbf{i}, \mathbf{j})$ plane and along direction $\mathbf{k}$ respectively - this latter is diagnosed via the incompressibility condition in eq. (1.3b)); T, S, ρ potential temperature, salinity, and in-situ density; ∇ is the generalized derivative vector operator along each direction of the reference frame, t, z are time and vertical coordinates, in-situ density is determined from its equation of state, ρ_0 is a reference density, p is the pressure, $f = 2\boldsymbol{\Omega} \cdot \mathbf{k}$ is the Coriolis parameter ($\boldsymbol{\Omega}$ being the Earth's angular velocity vector), g is the gravitational acceleration; D terms account for the parametrizations of small scale physics and F for surface forcing terms. More detailed information about the nature of each term is largely discussed in the NEMO manual (Madec et al. (2017)).
Despite its wide usage, this formulation is not the best available to model the oceans, being possible also to have different approximations and formulations (see for example Casulli (1999) and references therein).

1.4 Motivations for this study

The first part of the PhD activities focused mainly on large scale circulation in a situation closer to reality. Despite improvements, there are still vast uncertainties in the modelling and understanding of the mechanisms determining the variability and stability of Earth's climate tipping points (Lenton et al. (2008)), such as the Atlantic Meridional Overturning Circulation (AMOC). Indeed, due to the combined effect of having a broad range of physical processes at play, and limitations in our current ability to sense the ocean, mechanisms producing certain variations are still poorly understood. Combining models and observations in Reanalyses, which are thus historical, gap-free and dynamically consistent reconstructions of the ocean past history, it is possible to explore how the ocean circulation changed in the last decades or so, allowing for the possibility develop hypotheses for future model sensitivity experiments and gaining more insights on how these various actors interact one with each other (with the hope to improve even our ability to model and predict). These factors can include complex oceanographic and atmospheric processes (such as the effect of North Atlantic Oscillation (NAO) variations, deep water formation in high latitude seas, Gulf Stream front variations, salt advection feedback mechanisms within the basin), as well as technical aspects (such as the impact of data assimilation scheme, parameterization of unresolved scales, strength of relaxation imposed by flux adjustment procedures, different model physics, see Storto et al. (2019) for a

recent discussion).
Moreover, large uncertainties are directly connected with the impossibility to include all scales of motions in a global climate model simulation at the current stage, which comprise important processes such as the inclusion of wave effects (of different origin) on the large scale circulation of the ocean. One approach could be to attempt an estimate on real data available (Nikurashin and Ferrari (2013)), or to use a General Circulation Model (GCM)and test for the effect of changing parameterization (Perezhogin (2020)).
Another possibility is to tackle the challenge from the other side, i.e. using a high resolution simulation which does not employ any parameterization, directly resolving wave processes and small scales [1].
This will cost us to adopt a more theoretically-oriented point of view, which imply the neglection of some real world aspects, such as boundaries and topographic features, straits and so on, but at the same time will allow us to study the behavior of governing equations avoiding some approximations, such as the hydrostatic balance (through the use of Boussinesq equations).
With this spirit, in the last part of the thesis we focus the attention on more fundamental questions regarding small-scales and turbulence, i.e. how the energy is partitioned between waves and vortices, how their presence affects the evolution and dynamics of an ideal rotating stratified turbulent flow and to what extent they are able to reproduce or deviate from a known scaling behavior (such as the Garrett and Munk spectrum for inertial-gravity waves).
The presence of a vast range of temporal and spatial scales (see figure 1.2) in the dynamics of both atmospheric and oceanic flows (e.g. in a broad sense, the climate system) and their mutual nonlinear interactions and feedbacks raise the computational cost of any attempt toward a seamless simulation of the Earth's climate system. Again, there are two main strategies to fill this gap: explicitly increase model resolution, or develop parametrizations that account for the average effect of the unresolved scales. While the latter has been developed and constitute a well-established paradigm, the first relies on the constant increase of computational power, but both strategies are still in a continuous improvement process (Perezhogin (2020), Kjellsson and Zanna (2017)).

On a long term perspective, the hope is to succeed in casting our results with the idealized, open-ocean, simplified and rather theoretical situation into new parameterizations, which accounts for the effect of the inverse energy backscatter on large scales (Wunsch and Ferrari (2004), Ferrari and Ferreira (2011)), or at least to understand what are the still missing pieces or paradigm shifts we need to have a seamless simulation of a *digital twin of the Earth* (Bauer et al. (2021)).

[1] We notice that there are examples, such as ECMWF ERA5 which implements fully-coupled atmosphere-ocean-wave-ice dynamics, in which some wave effects are included, but there are still smaller scales whose treatment relies on the use of parametrizations.

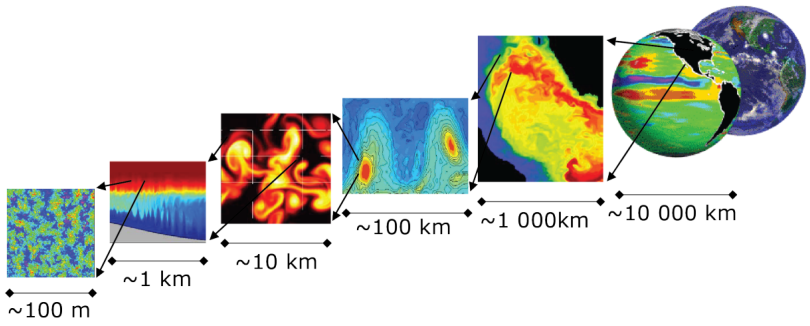

Figure 1.2. The vast range of nonlinear interacting spatial scales which an ideal climate model should encompass and resolve (taken from Adcroft et al. (2018)).

2

The Atlantic Meridional Overturning Circulation

"All work
and
no play
makes Jack
a dull boy."

Stanley Kubrick,
Shining

This chapter will describe current understandings, definitions, main processes and open questions behind the AMOC, briefly reviewing its structure, variability, driving physical processes and simplified models.

2.1 Current understanding of the AMOC

The Hadley overturning circulation is a central part of the atmospheric general circulation, with the troposphere heated from below, mainly at tropical latitudes. In the ocean, buoyancy loss in the upper surface drive meridional overturning cells emanating from the poles. Topographical features make the Atlantic unique among world oceans, being the only one characterized by sinking of water masses in the northern hemisphere. This makes possible to observe, in the global conveyor belt picture (Broecker (1991)), a pole-to-pole circulation, which is central in regulating Earth's climate stability. Indeed, a net northward flow of light waters in the upper thousand meters across the northern hemisphere characterizes the basin. Compensating this surface northward flow, a net southward flow of denser North Atlantic Deep Water (NADW) crop up between the upper one and three kilometres in the southern hemisphere. Transformations from lighter to denser waters occur in polar regions, the North Atlantic being the hotspot for buoyancy loss, and buoyancy gain characterizing the Southern Ocean (Buckley and Marshall (2016)). Here, Ekman transport and upwelling of dense waters arise as a response to strong westerly winds blowing around Antarctica, causing outcropping of isopycnals (surfaces of constant density), i.e. inducing baroclinic instability and creating eddies that oppose the

wind-driven circulation. Being the result of pressure and density gradients being not aligned, baroclinic instability drives a residual overturning directed along isopycnals in the ocean interior and across them in the surface mixed layer (i.e. the layer in which there are most important variations in seawater density or temperature - there are many criteria to define it, we will see some of them in the following). Part of the isopycnal upwelled intermediate waters become denser, forming Abyssal Antarctic Bottom Water (AABW), subsequently downwelling down the continental slope toward Indian and Pacific oceans. Here, upwelling to mid-depths will take place, eventually leading to re-insertion of AABW in the Atlantic. Meanwhile, the short extent of the African continent favours the import of salty and warm subtropical waters from the Indian Ocean via the Aghulas leakage from the east. In North Atlantic, mesoscale eddies and wind-stress modulate the buoyancy budget, with vortices connecting regions of buoyancy loss to downwelling zones. Rossby and boundary waves propagation are the primary mechanisms for large scale adjustment of this (AMOC) to changes in wind-stress and buoyancy fluxes (see the sketch in figure 2.1 - see (Kuhlbrodt et al. (2007), Buckley and Marshall (2016), Johnson et al. (2019)) for complete reviews on the subject). The most common way to represent

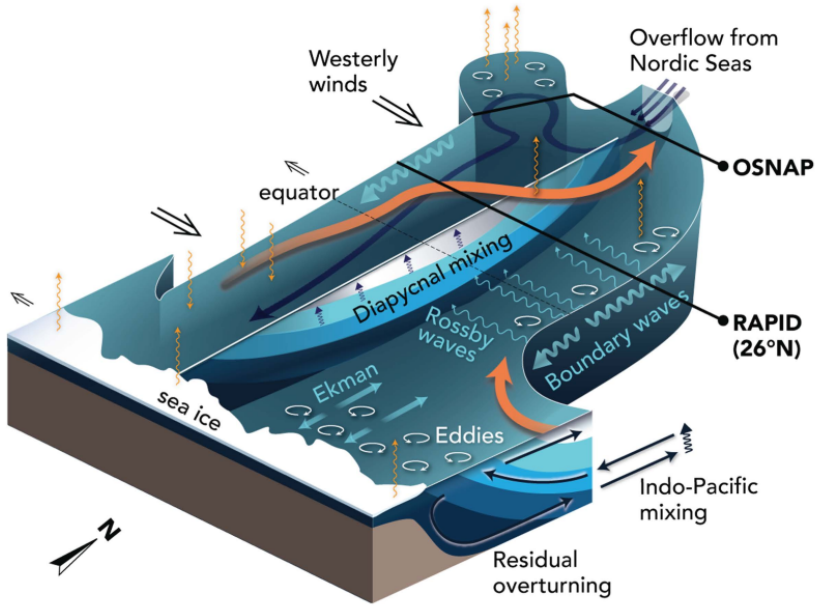

Figure 2.1. Current overview of the AMOC main mechanisms and dynamics as depicted in a recent review paper by Johnson et al. (2019).

the AMOC and its associated *meridional* volume transport is through a stream function in depth-latitude-time space, e.g. as the following equation prescribes:

$$\psi(y,z,t) = \int_{\eta}^{z} dz' \int_{x_e(z')}^{x_w(z')} dx\ v(x,y,z',t), \tag{2.1}$$

where (x, y, z', t) are respectively the coordinates axes for longitude, latitude, depth (increasing downward) and time. Zonal integration of the meridional velocity v (i.e.

the volume flux through a given parallel) is carried out from the western boundary x_w to the eastern boundary x_e of the Atlantic basin, while the integration in depth is accumulated from the free surface η to the given depth z (Buckley and Marshall (2016)). Positive values indicate northward, while negative one southward volume transport, which are commonly measured in Sverdrups ($1Sv = 10^6 m^3/s$).
Alternatively, another approach consists into substituting depth with potential density anomalies, motivated by the fact that in this way one can keep track of the transformation among different density classes due to surface heat and freshwater fluxes, interior diapycnal mixing and bottom geothermal heating (Cessi (2019)).
It is very important to keep in mind the three dimensional structure of pathways composing the AMOC: Lagrangian methods are an invaluable tool in complementing the Eulerian description of this zonally averaged meridional flow, revealing the non-continuous character of the Atlantic Overturning. Indeed, as can be seen by the figure 2.2, there are many possible re-circulation regions and interior pathways, which can somehow delay the water mass transport both in the surface and at depth.

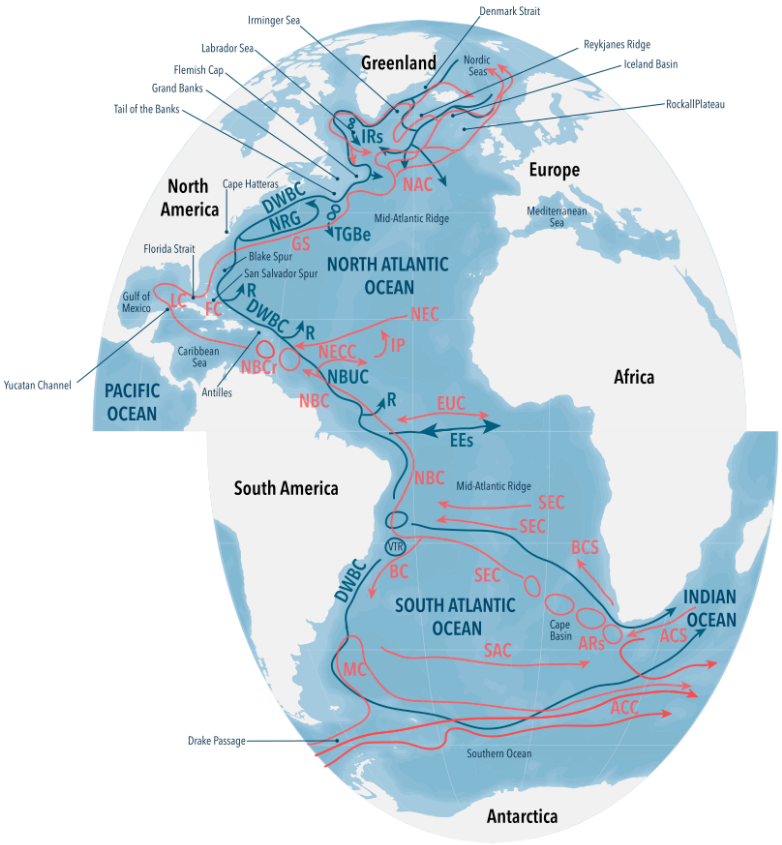

Figure 2.2. Overview of the upper (red) and lower (blue) limbs of the AMOC as observed by the Lagrangian method. This figure includes most geographic features and currents mentioned in text. Bathymetry is shaded at 1,000-m intervals. In alphabetical order the main pathways: ACC, ACS, ARs, BC, BCS, DWBC, EEs, EUC, FC, GS, IP, IRs, LC, MAR, MC, NAC, NBC, NBCr, NBUC, NEC, NECC, NRG, R, SAC, SEC, TBGe VTR. Taken from Bower et al. (2019)

2.1.1 Key processes involved in AMOC dynamics

One of the main oceanic processes in the AMOC dynamics is Deep Water Formation (DWF) in the Northern North Atlantic. Lateral eddy fluxes in the ocean interior and direct cooling with the atmosphere heat fluxes are the principal responsible for the buoyancy loss within these regions, determining dense water formation in northern seas (Labrador, Irminger and Greenland Seas). Net sinking taking place along the boundaries of these basins, commonly known as Eulerian downwelling, produce stretching of planetary vorticity, balanced by lateral diffusion of vorticity near topographic features (Pickart and Spall (2007)). This water mass transformation constitutes a connection between the northward-flowing upper limb to the southward-flowing lower limb of the AMOC. Geostrophic balance characterizing the leading order approximation to large-scale upper ocean flows prescribe the net inflow to outflow from a marginal sea to be proportional to pressure changes across its opening. Density field variations are an indirect proxy for diagnosing net downwelling strength, being the pressure field almost everywhere in hydrostatic balance. Understanding the buoyancy budget of the marginal sea is thus a necessary step in searching for causes of downwelling. Cyclonic boundary current surrounding weak mean flows in the basin's interior is a common characteristic of deep convection areas in the North Atlantic (Luo et al. (2016)). Figure 2.3 summarizes how DWF takes place in semi-enclosed basins (e.g. the Labrador Sea). A warm inflow boundary current coming from southern latitudes begins cooling and freshening while wrapping the basin interior. Thanks to buoyancy loss occurring throughout a significant fraction of the sea surface, this warm inflow sheds buoyant eddies and downwells along with the topography while wrapping the semi-enclosed basin. Lateral eddy

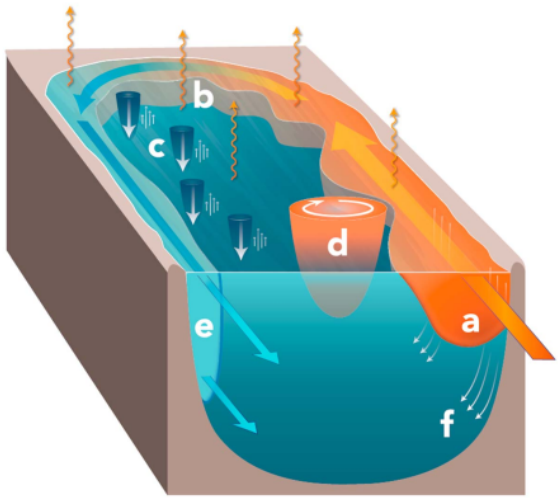

Figure 2.3. Main processes in semi-enclosed, dense-water-forming basins: (a) warm inflowing boundary current, (b) buoyancy loss to the atmosphere, (c) convective plumes, (d) buoyant eddies shed from the boundary current, (e) cooler outflowing boundary current, and (f) downwelling along the topography. Taken from Johnson et al. (2019).

fluxes provide the connection between diapycnal mixing (deep convection in the ocean's interior) and eulerian mixing near the boundaries (vertical transport),

determining, together with mean horizontal advection and air-sea exchanges (remote and local control effects respectively), temperature and salinity of the water masses participating in deep convection (Straneo (2006)).
The stability of the boundary current strongly influences the presence of mesoscale eddies, which are crucial to provide a balancing mechanism between heat, salt and air-sea fluxes. Indeed, if the southward coming boundary current reaches northern latitudes, deep convective areas are warmer (increased air-sea fluxes), owing to the shedding of warm and salty eddies into the basin interior; if on the other hand, the boundary current is very stable, reaching lower latitudes, eddies are not able to carry much heat in the interior, and the atmosphere cools down the sea surface more efficiently (air-sea fluxes reduced). These processes contribute to modify substantially the preconditions for DWF. Kuhlbrodt et al. (2007), analyzing driving processes of the AMOC, pointed out that surface buoyancy forces alone are not able to sustain a steady state overturning in the ocean, this conclusion being supported by Sandström theorem (Sandström (1908)). Though, it is also true that DWF processes are an important part of the overturning path, contributing to push the thermohaline loop in the Atlantic ocean, together with other processes such as winds, tides and salt advection feedback. Box models have been very useful to understand the properties of thermohaline motions in the ocean, viewed under the lens of simpler dynamical systems. In order to have a big picture on the current and past understanding of the AMOC, we think it is worthwhile to review the first simpler box model of the thermohaline circulation, which will give us the opportunity to introduce the important concept of the salt advection feedback mechanism.

2.1.2 Multiple equilibria: conceptual models of the AMOC

Stommel (1961) paper is a cornerstone of the theoretical understanding of thermohaline motions in the oceans. Indeed with this elegant box model, it is possible to cast the dynamics of a hemispheric flow on very long time scales into a system of ODEs, showing the appearance of multiple equilibrium states depending on the parameter variations. This simple but highly nontrivial result opened an entire field of research: generalizations of the box model were proposed, leading to a substantial improvement in the development of the search for analytical models for the AMOC (Stommel (1961), Andrews and Mcintyre (1976), Nikurashin and Vallis (2011), Nikurashin and Vallis (2012), Wood et al. (2019), Alkhayuon et al. (2019)). In its original formulation, he created a simple dynamical system of two equations describing the long-term dynamics of the temperature and salt differences in both hemispheres, modelled as a system of two boxes with porous walls connected by a channel overflow. Notwithstanding its rewriting in modern terms, we think it is interesting to track the calculation in the original paper. The most interesting situation is when you have two vessels coupled by a surface overflow at the top and a capillary tube at the bottom. In this instructive case, it can be shown that this system presents multiple equilibria in the steady regime. Thermohaline circulation is schematically depicted as free convection between two interconnected reservoirs, which arise in response to density difference maintained by salt and heat transfer to the reservoirs, and has been shown to occur in two different stable regimes. This, to cite the words of Stommel:

maybe be possibly analogous to certain features of the oceanic circulation.

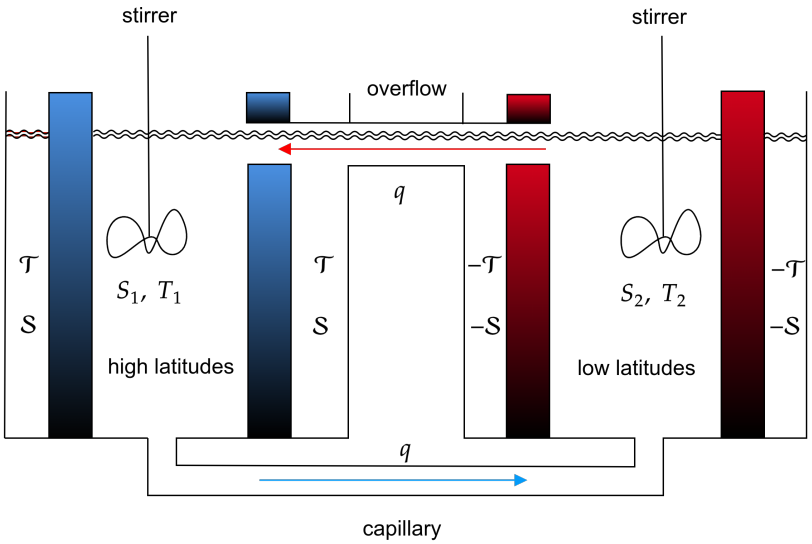

Figure 2.4. Stommel's 1961 Box model for thermohaline circulation. Box 1,2 respectively represent equatorial and polar latitudes. Porous walls made up of a material allowing heat and salt transfer with environmental values $\mathcal{T}$, $\mathcal{S}$ (regarded as constant) are marked in orange.

The set of equations for the two vessel can be written in the form:

$$\begin{aligned}
\tfrac{dT_1}{dt} &= c\,(\mathcal{T} - T_1) - qT_1 + qT_2, \\
\tfrac{dS_1}{dt} &= d\,(\mathcal{S} - S_1) - qS_1 + qS_2, \\
\tfrac{dT_2}{dt} &= c\,(-\mathcal{T} - T_2) - qT_2 + qT_1, \\
\tfrac{dS_2}{dt} &= c\,(-\mathcal{S} - S_2) - qS_2 + qS_1,
\end{aligned} \tag{2.2}$$

where c, d are respectively the relaxation coefficients for temperature and salinity, and $\mathcal{T}, \mathcal{S}$ are respectively the temperature and salinity of the external environment, which is so large that they can be regarded as constant. The relaxation of inner values toward equilibrium takes place through porous walls permitting heat and salt transfer in a simple linear fashion, as shown by figure 2.4. The other element is the overflow q, which is proportional to the density difference, and represent the coupling flow between the two vessels, i.e. the thermohaline circulation strength:

$$kq = \rho_1 - \rho_2 \tag{2.3}$$

for the density in each box, a linear equation of state is assumed to be valid:

$$\rho_i = \rho_0 \left[1 - \alpha T_i + \beta S_i\right], \qquad i = 1, 2 \tag{2.4}$$

where ρ_0 is a reference density, α, β are coefficients measuring the relative importance of temperature and salinity in the density equation of state.
In his original article, Stommel is interested in the symmetric case, in which it is possible to write the system in terms of single values for temperature and salinity $T = T_1 = -T_2$, $S = S_1 = -S_2$. In this way is it possible to rewrite the system in eqn. 2.2 as

$$\begin{aligned} \tfrac{dT}{dt} &= c\,(\mathcal{T} - T) - |2q|\,T \\ \tfrac{dS}{dt} &= d\,(\mathcal{S} - S) - |2q|\,S \\ -\tfrac{dT}{dt} &= c\,(T - \mathcal{T}) + |2q|\,T \\ -\tfrac{dS}{dt} &= d\,(S - \mathcal{S}) + |2q|\,S \end{aligned} \tag{2.5}$$

and observe that the four equations are not independent one from another: the first and the third, and the second and the fourth are telling the same story. The use of symmetry helps us to reduce the degrees of freedom of the system. It is possible to bring this system into a non-dimensional form by scaling all the variables. If we choose to describe the system in terms of the new set of coordinates and parameters

$$\tau = ct, \quad \delta = \frac{d}{c}, \quad y = \frac{T}{\mathcal{T}}, \quad x = \frac{S}{\mathcal{S}}, \quad f = \frac{2q}{c}, \quad \lambda = \frac{4\rho_0\alpha\mathcal{T}}{ck}, \quad R = \frac{\beta\mathcal{S}}{\alpha\mathcal{T}} \tag{2.6}$$

it is possible to rewrite the system of the two coupled equation and the condition expressing the flux in terms of density differences as

$$\begin{aligned} \tfrac{dy}{d\tau} &= (1 - y) - |f|\,y, \\ \tfrac{dx}{d\tau} &= \delta\,(1 - x) - |f|\,x, \\ \lambda f &= (-y + Rx)\,. \end{aligned} \tag{2.7}$$

We can observe the non-triviality of the system resides in the coupling term f. By putting this information in the above equations for non-dimensional variables, we obtain:

$$\begin{aligned} \tfrac{dy}{d\tau} &= (1 - y) - \tfrac{y}{\lambda}\,|-y + Rx|\,, \\ \tfrac{dx}{d\tau} &= \delta\,(1 - x) - \tfrac{x}{\lambda}\,|-y + Rx|\,. \end{aligned} \tag{2.8}$$

We will start form these to study the stability of this system. First of all, we observe the behaviour of the system is governed by three parameters δ, λ and R. Their separate role can be understood by looking explicitly at the terms in which they appear:

- if $\lambda \to \infty$, the system decouples into two independent equations, which predict an exponential decay in time, the delay between the decaying behaviour for temperature and salinity being controlled by δ, and the role of R becomes irrelevant;
- if $R = 0$, with all the other parameters being different from zero and finite, the dynamic of the temperature field is decoupled from the salinity, but the

converse does not hold. This means the dynamic evolution of the system being driven exclusively from temperature.

- if $\delta \to 0$, the equation for the salinity is purely nonlinear and coupled with temperature, which instead has a linear part in its evolution.

It is necessary to solve the system when the derivative terms vanish to study the stability points. We will show this lead to multiple equilibria, depending on the values of the parameters:

$$\begin{aligned} \tfrac{1-y}{y}\lambda &= |-y + Rx| \\ \delta\lambda\tfrac{1-x}{x} &= |-y + Rx| \,. \end{aligned} \tag{2.9}$$

Equating these two, we get for y in term of x:

$$\frac{1-y}{y} = \delta\frac{1-x}{x} \to \frac{1}{y} - 1 = \delta\frac{1-x}{x} \to y = \frac{x}{x(1-\delta)+\delta}, \tag{2.10}$$

putting this expression inside the equation for y we get, after manipulating terms

$$R\,(\delta-1)\,x^3 + \left(\delta^2\lambda - \delta\,(\lambda+R) + 1\right)x^2 + \left[(1-2\delta)\,\delta\lambda\right]x + \delta^2\lambda = 0 \tag{2.11}$$

and from this, we can clearly see that, depending on the values of the parameters, the order of this last equation can change, modifying the number of equilibrium points in the system (see figure 2.5). It can be easily shown that, also in the non-symmetric

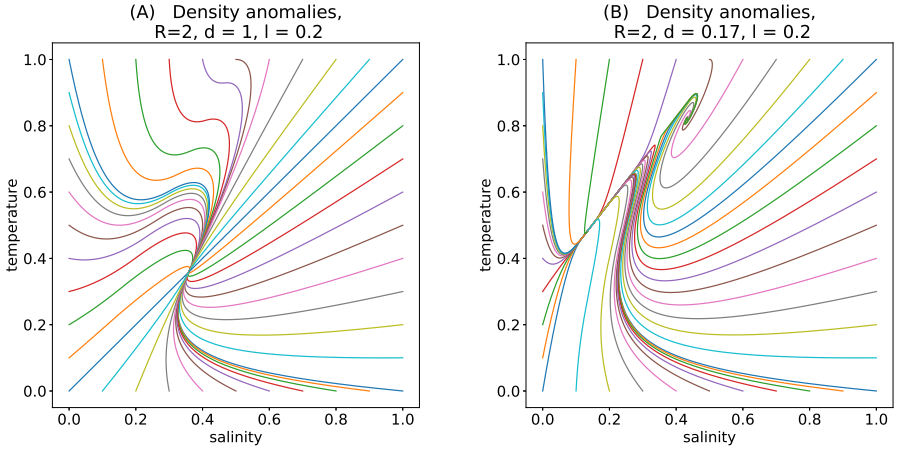

Figure 2.5. (A): single stable node for the case $R = 2$, $\delta = 1$, $\lambda = 1/5$; (B): the three equilibria for the case with $R = 2$, $\delta = 1/6$, $\lambda = 1/5$.

case, it is possible to write the system in the same form, with exactly the same parameters, but defining non-dimensional variables as

$$y = \frac{T_1 - T_2}{2\mathcal{T}}, \qquad x = \frac{S_1 - S_2}{2\mathcal{S}}. \tag{2.12}$$

This lead to the conclusion that multiple equilibria can also appear in the more general non-symmetric case. In the three equilibrium points scenario, only two are

attractive, the third one being repelling. This can be shown by doing a little step further, which is the linear stability analysis of the system near its fixed points. More details have been gathered in a review paper by Wunsch, in which also the Sanström theorem is treated Wunsch (2005).
The existence of thermohaline multiple equilibrium states raises fundamental (still open) questions on the AMOC dynamics, such as: is it possible to observe transitions between monostable and multistable regimes of the AMOC? What is the stability regime of the AMOC in a changing climate? What are the current limitations of indicators describing whether the AMOC in climate models is in a monostable or multistable framework? Is the representation of the zonal mean stream function adequate to describe the circulation, or is it necessary to consider other additional important east-west factors and processes? Transitions between different stability regimes have indeed already observed through the use of GCM model experiments (Rahmstorf (1996) constitutes a seminal work, Liu and Liu (2013), Liu et al. (2017), Castellana et al. (2019) give some example of the modern development of the research on the subject).

2.1.3 Feedback mechanisms and AMOC stability indicators

Stommel (1961) paper is so important because of the so-called positive salt advection feedback. According to this mechanism, the NADW cell of the AMOC transports salt northward, maintaining seawater salinity relatively high in DWF regions despite the freshwater input in the northern midlatitudes. These waters sink downward because they are heavier than the surrounding. A positive advective feedback results: the round-the-clock circulation keeps on the DWF, and conversely, with a halted NADW formation, there is no northward salt transport, and hence DWF is suppressed.
This mechanism gives rise to a parabola-shaped stability diagram that shows the bistability of the overturning strength plotted vs the atmospheric freshwater transport (see figure 2.6): for a fixed freshwater flux, there is one stable state with and one stable state without an overturning circulation.
Additional, convective feedback regards the specific DWF site, such as the Labrador Sea. A net freshwater input characterizes the DWF site. If convection happens regularly, mixing with deep saline waters trigger a densification process of the inflowing freshwater. This results in having high surface density and thus feeds the occurring of convection events in the following winter. However, owing to variability in the surface fluxes, freshwater can accumulate at the convection spot. Indeed, when convection has not occurred for a couple of years, decreasing the surface density, convection events may not crop up anymore, and convection sites may be switched off. Following the pioneering ideas of Stommel, a vast number of studies applied these concepts to ocean models (Bryan (1986), Marotzke and Willebrand (1991), Tziperman et al. (1994), Rahmstorf (1995), Rahmstorf (1996)). These feedback mechanisms imply bistability: there can be an on-off state of thermohaline circulation depending on constant boundary conditions.
The Stommel model for the large-scale Meridional Overturning Circulation (MOC) assumes that the boxes in his model, undergoing a continuous stirring mechanism, are well mixed, so surface buoyancy fluxes directly affect the deep flow. Rahmstorf

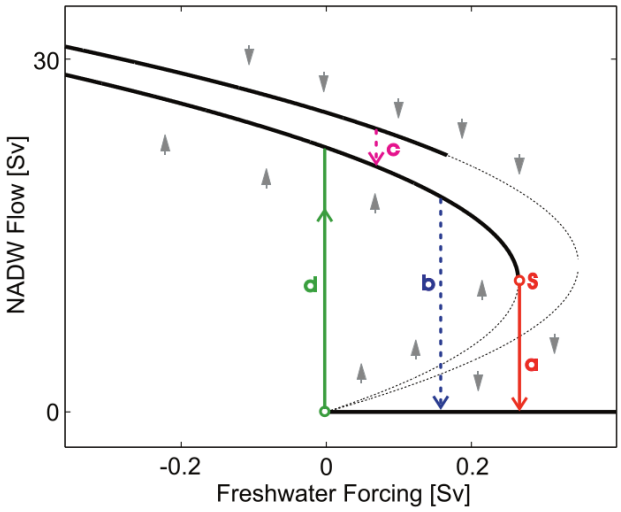

Figure 2.6. Stability diagram for the volume flux of NADW cell from a modified version of Stommel (1961) model. Solid black lines indicate stable equilibrium states, and dotted black lines indicate unstable states. Changing the freshwater flux into the North Atlantic shifts the position on the branches and may trigger transitions, indicated by arrows. a, NADW cell spin down due to advective feedback; b, shutdown due to the convective feedback; c, transition between different deepwater formation sites induced by the convective feedback; and d, restart of the NADW cell. "S" marks the Stommel bifurcation point beyond which no North Atlantic Deep Water formation can be sustained. Taken from Kuhlbrodt et al. (2007).

(1996) first and then Dijkstra (2007), Liu and Liu (2013), Liu et al. (2017) proposed an indicator to diagnose the AMOC bistability regime. According to their definitions, stable (unstable) phases of the AMOC can be characterized by positive (negative) dynamical metric named ΔM_{ov}, or Σ, which is defined as the freshwater transport difference advected by the AMOC across the southern and northern boundaries of the Atlantic ocean. These contributions can be calculated approximately as

$$M_{ov}(\phi) = -\frac{1}{S_0}\int_{-D}^{\eta} V^*(\phi, z)\,\langle S(\phi, z)\rangle\, dz, \tag{2.13}$$

where $S_0 = 34.8PSU$ is a reference salinity, z represent the depth, $-D$ is the depth of the ocean bottom and η the free surface of the ocean, $V^*(\phi, z)$ is the zonally integrated meridional baroclinic velocity, and $\langle S(\phi, z)\rangle$ is the zonal mean salinity along the section at the selected latitude ϕ. The definition of the freshwater convergence (if positive) or divergence (if negative) is:

$$\Delta M_{ov} = M_{ov,S} - M_{ov,N}. \tag{2.14}$$

In eqn. (2.14), the first term on the r.h.s. is the AMOC-induced freshwater transport across the Southern Boundary of the Atlantic (along the zonal section at 34° S); the second term on the right side is the AMOC-induced freshwater transport across the Northern Boundary of the Atlantic (along the zonal section at 80° N).
The second term is composed of three main contributions: the Canadian Arctic

Archipelago, the Fram Strait, and the western shelf of the Barents Sea. The negative sign of ΔM_{ov} indicates an unstable AMOC because of the divergence of freshwater transport, resulting in larger buoyancy forcing and vice versa.
However, the suitability of this indicator to give a precise answer on the AMOC stability regime is still a matter of debate. Indeed, suppose that the AMOC is in its stable regime. This means that if the AMOC freshwater transport is negative, then the gyre freshwater transport must be greater than the AMOC transport for the total freshwater transport across 33°S to be positive. Recent model experiments at eddy-permitting resolution (1/4°) have shown that the gyre circulation freshwater transport can be twice as large as the AMOC freshwater transport change at 33°S. This casts strong doubts on the usefulness of the simple AMOC stability criterion, which assumes that other freshwater transport processes, such as the gyre circulation, do not change in response to AMOC changes (Gent (2018)).

2.2 What processes drive Ocean Heat Transport?

In the North Atlantic, the maximum northward Ocean Heat Transport (OHT) is about 1 PW, primarily due to the presence of the AMOC.
As we already pointed out, the surface fluxes of momentum (winds), heat (solar radiation) and freshwater (river and glacier runoff or precipitation), gravity and tides (action from the Moon) force oceanic motions on a wide range of scales, but vertical mixing and wind-driven upwelling are the most probable candidates to provide enough energy to sustain this overturning circulation.
Winds and tides generate internal waves in the oceans, which dissipate into small-scale motion causing turbulent mixing. This mixing of heat lightens water masses in the deep layers and causes them to rise in low latitudes, and then advected poleward into the North Atlantic, where they are transformed into dense waters by atmospheric cooling and salt rejection during sea ice growth. These waters sink to depth and spread, setting up the deepwater mass of the ocean. This mixing is across isopycnals, thereby establishing a meridional density gradient between high and low latitudes.
Observational proxy data suggest that mixing alone cannot provide the necessary energy input to sustain a volume transport characteristic of the AMOC, so it must be accompanied by a wind-driven process. The westerly circumpolar winds blowing around Antarctica induce vigorous northward Ekman transports near the ocean surface. The horizontal divergence of the Ekman transport causes upwelling from depths, which is associated with the so-called Drake Passage effect (Kuhlbrodt et al. (2007) and references therein).
Both winds and high latitude convection sensibly affect the OHT associated with deep circulation in the North Atlantic. When convection in North Atlantic is suppressed, at the same time increasing the winds by 50%, it has been shown that there are minor changes in OHT in the northern hemisphere, while significant changes take place in the southern hemisphere, where winds are the principal driving mechanism for the circulation (Ferrari and Ferreira (2011)).
At the same time, the OHT seems to be weakly sensitive to changes in the eddy diffusivity, which represents eddy mixing strength in the most used parametrization

(Gent and Mcwilliams (1990)), though there are signs that this parametrization underestimates the role of eddies in driving the ocean heat transport (Perezhogin (2020)). Moreover, in current state-of-the-art general circulation models, internal gravity waves are often parameterized or not treated at all (Jochum et al. (2013), Nikurashin and Ferrari (2013), McWilliams (2016)). Whether or not small scale processes such as vortex-wave interactions could impact the large scale OHT and energy transfer across scale (and how to include these effects, if any) is still a totally open field of research.

3

Assessment of the North Atlantic Variability

"The Road goes ever on and on
Down from the door where it began.
Now far ahead the Road has gone,
And I must follow, if I can,
Pursuing it with eager feet,
Until it joins some larger way
Where many paths and errands meet.
And wither then? I cannot say.
The Road goes ever on and on
Out from the door where it began...

J.R.R. Tolkien,
The Lord of the Rings

In this chapter, I will summarize my scientific activity, which started during the assessment and evaluation phase of the Copernicus Climate Change Service (C3S) project and led my interests toward an attempt to describe and characterize an ocean circulation regime change observed in the Atlantic Meridional Overturning Circulation, diagnosed from the ECMWF Ocean Reanalysis-Analysis System 5 (ORAS5) dataset. Combining modelling with observation in a spatial and temporal consistent way, these data reconstruct the ocean's past history from 1979 to 2018. The first part of the chapter will be devoted to describe data and methodologies used in this study. Last part will summarize the attempt to characterize possible causes for this regime change, and to assess its effect on the Ocean Heat Content variability at a global and regional scale via the comparison with other Reanalysis data offered within the Copernicus Marine Environmental Service (CMEMS).

Despite its pivotal role in modulating North Atlantic climate variability and stability, the AMOC is not the only factor to consider. Indeed, the surface circulation of the North Atlantic includes an anticyclonic subtropical gyre and a cyclonic subpolar gyre, which are wind-driven for the most part. While the dynamics of the first strongly depends on the Gulf Stream and the south part of North Atlantic Current path variations, the latter is more symmetric and strongly constrained by topography (Talley (2011) - section 9.3). Moreover, atmospheric phases of positive and negative North Atlantic Oscillation (NAO) can have a great resonance in North Atlantic dynamics. In particular, in Robson et al. (2014) paper, it has been suggested that the decline in AMOC strength from 2004 to 2012 measured at the RAPID-MOCHA section is part of a substantial reduction on decadal timescales. Furthermore, simulations with a coupled model highlighted that there can be a tight connection between AMOC and deep water formation in the Labrador Sea, especially when density anomalies spread southward and influence the east-west density gradient, with major impacts on the large-scale circulation (Delworth and Zeng (2016), Putrasahan et al. (2019)). In a previous paper (Robson et al. (2012)), the causes of the rapid warming of the North Atlantic in the mid 1990s were investigated through the comparison between ocean analyses and model experiments. According to their findings, there is persuasive evidence that a slowdown of the AMOC strength can arise as a lagged response to a persistent positive phase of the NAO prior to 1995. Another important outcome of their analysis is that this lagged response was primarily caused by changes in the ocean circulation triggered by buoyancy fluxes, rather than by wind stress variations. In this view, not only short term wind induced variations, but also long term modes of climate variability, such as the Atlantic Multidecadal Oscillation (AMO), can play a role in modulating AMOC changes. However, such connections between AMOC and AMO are not yet fully understood (Talley (2011), Marullo et al. (2011), Trenary and DelSole (2016), Zhang et al. (2019)), and still constitute a matter of active debate.
Several studies (Robson et al. (2016) and references therein) have demonstrated that the AMOC is a principal factor in determining the evolution and dynamics of the Ocean Heat Content (OHC) at both the regional and global scale, and the main reason is the overturning net northward transports of heat and salt. Intercomparison studies constitute a precious way to push our knowledge further. Indeed, both the AMOC and the OHC have been the subject of many fundamental intercomparison papers (Karspeck et al. (2017), Palmer et al. (2017), Jackson et al. (2019)), showing that the AMOC representation in different ocean reanalyses is inconsistent (Karspeck et al. (2017)), and displaying disagreements in OHC trends and mean state in different reanalyses (Palmer et al. (2017)). Uncertainties permaining, at the same time it is also true that most ocean reanalysis datasets agree on the positive OHC trend, supporting evidence for ocean's warming without a robust consensus on the warming rates (Palmer et al. (2017)).
More detailed studies have been carried out recently to understand the capability of ocean reanalysis in representing North Atlantic dynamics in ensemble ocean reanalyses. For example, Jackson et al. (2019) show that reanalyses present wide discrepancies on Labrador Sea Mixed Layer Depths (MLD), variability in the AMOC at different latitudes, underestimation of the ocean heat transport, and misrepresentations of the Gulf Stream path, especially in the period previous to the Argo era

(from mid-2000 onward). Several factors are responsible for the discrepancy of ocean reanalysis datasets, such as model physics, technical aspects as SST nudging related processes, data assimilation scheme, flux adjustments that can induce significant changes in the Labrador Sea density, AMOC and subpolar gyre strength (Pohlmann et al. (2013)): implementation of two-way, ice-wave coupled GCM could significantly improve their performances. In this view, assessment of ocean reanalyses, investigation of differences across different products, their causes and impacts on the climate system is of paramount importance to overcome the new source of challenges and open questions posed by previous studies.

3.1 Data description

In this section we will briefly describe all the data used in this study, which are publicly available, and distributed through web infrastructures such as the Integrated Climate Data Center (ICDC) of Hamburg[1], the RAPID-MOCHA website[2], and the CMEMS portal[3]. Brief description of other sources of data used to corroborate our results are included, such as the previous version of ECMWF reanalysis ORAS4, Simple Ocean Data Assimilation and in-situ data of SAMBA in the southern hemisphere.

3.1.1 ORAS5 Ocean Reanalysis by ECMWF

The data we use in this study are an ensemble (5 members) of global ocean reanalyses (ORAS5) produced by the ECMWF, covering the period from 1979 to 2018. The ocean model of ORAS5 is based on NEMO in its global configuration ORCA025, (NEMO 3.4) with a horizontal resolution of 0.25 degree (about 9 km in the Arctic, and 25 Km at the equator) and 75 vertical levels, coupled with the Louvain-la-Neuve sea-ice model version 2 (LIM2) sea ice model. From 1979 to 2018 the atmospheric forcing comes from the ERA-Interim ECMWF reanalysis. The data assimilation scheme is NEMOVAR in its 3D-FGAT (First-Guess at Appropriate Time) configuration, and it is used to assimilate temperature and salinity profiles (EN4 with XBT/MBT correction, Gouretski and Reseghetti (2010)), sea-ice concentration (reprocessed from OSTIA) and altimeter derived along-track sea-level anomalies (SLA - AVISO) data (Zuo et al. (2018), Zuo et al. (2019)). SST (reprocessed HadISST2 + OSTIA) is assimilated via a simple nudging scheme by modifying the surface non-solar total downward heat flux using a global uniform restoration term of 200 W/m^2K (Tietsche et al. (2020)).
Members of the ensemble are obtained from slight perturbation in the assimilated observations, forcing, and initial conditions.

3.1.2 GREP from CMEMS

The other source of data we used is an ensemble of four global reanalysis products gathered together by Copernicus Marine Environment Monitoring Service (CMEMS)

[1] `http://icdc.cen.uni-hamburg.de/projekte/easy-init/easy-init-ocean.html`
[2] `https://www.rapid.ac.uk/`
[3] `http://marine.copernicus.eu/about-us/about-producers/glo-mfc/`

within the Global Reanalysis multi-model Ensemble Product (GREP) as detailed below.

- CGLORSv05: NEMO v. 3.4 + LIM2, surface forcing given by nudging of SST, SSS, SIC (Sea Ice Concentration), 7-day assimilation window of model Mean Dynamic Topography (MDT), Reynolds SST and EN4 data.
- FOAM GLOSEAv13: NEMO v. 3.4 + CICE v. 4.1, surface forcing given by nudging of SST, SSS, 1-day assimilation scheme of EN4 data.
- GLORYS2V4: NEMO v. 3.1 + LIM2, surface forcing given by precipitation, flux correction Climatological runoff and ice shelf and iceberg melting, with no surface nudging, 7-day assimilation window of Reynolds SST and CORA (Coriolis Ocean database for ReAnalysis) data, Merge MDT (model+observation).

We excluded ORAS5 from GREP because its ensemble mean was already included in the 1979-2018 time series.

All these products are based on NEMO, ORCA025 (1/4 o horizontal resolution), 75 vertical levels, with TKE, Altimetry ERA: 1993-2017 ERA-Interim and bulk formulae, and assimilate observations: SST, SLA, T/S profiles, SIC, Multivariate assimilation, monovariate for the sea ice concentration.

Major differences between the three analyzed members are in the version of the NEMO model, coupling with different Sea Ice Model, (LIM2 or CICE), data assimilated and the assimilation scheme used.

Further detailed and referenced information can be found in the product user manual [4].

3.1.3 SODA

Simple Ocean Data Assimilation (SODA 3.4.2) covers the period going from 1980 to 2017, based on MOM 5.1 and data assimilation scheme as linear deterministic sequential filter and forced by ERA-Interim (the same forcing as in ORAS5, but with a different flux correction procedure). Monthly files on the regular 0.5°×0.5° Mercator grid with 50 vertical levels have been used to extract the AMOC streamfunction at given latitudes to assess the robustness of results across different products. Further information about this dataset and comparison in the recent period (from 1993 onward) can be found in Carton et al. (2019).

3.1.4 ORAS4

Preceding the new generation of ECMWF's Ocean Reanalysis ORAS5, ORAS4 is based on NEMO v3.0, has lower horizontal and vertical resolution (1°×1° grid with equatorial refinement of 0.3° and 42 unevenly spaced vertical levels).The assimilated data include temperature and salinity profiles from the EN3 v2a XBT bias corrected database (1958-2009, Gouretski and Reseghetti (2010)), including XBT, CTD, Argo, Mooring, and from realtime GTS thereafter. Moreover, along track altimeter sea level anomalies and global trends from AVISO, SST and sea-ice are from the ERA-40

[4] http://resources.marine.copernicus.eu/documents/PUM/CMEMS-GLO-PUM-001-031.pdf

archive prior to November 1981, from the NCEP OI v2 weekly product (1981 until December 2009) and from OSTIA analysis from January 2010 onwards. The SST and sea-ice information is used to constrain the upper level ocean temperature via a Newtonian relaxation scheme. The assimilation method is NEMOVAR in its 3D-var FGAT mode with an assimilation window of 10 days. A bias correction scheme is used to correct the model/forcing errors. Forcing and relaxation used include daily surface fluxes of heat, momentum and freshwater. Prior to 1989, the surface fluxes are from the ERA-40 atmospheric reanalysis. From the period 1989-2009, the surface fluxes are from ERA-Interim reanalysis. From 2010 onwards, when ORAS4 started operational running, daily surface fluxes were derived from the operational ECMWF atmospheric analysis (Balmaseda et al. (2013a)).

3.1.5 RAPID-MOCHA in-situ measurements

The RAPID-MOCHA array is the first system able to monitor a basin-wide transport at a latitude (26.5^o N) continuously since 2004. It is designed to estimate the AMOC as the sum of three observable components namely, Ekman transport, Florida Current transport and the upper mid-ocean transports, and of course the total maximum volume transport (Buckley and Marshall (2016), Balan Sarojini et al. (2011)). We used the last available version of the data, whose details are specified in Moat et al. (2020).

3.1.6 SAMBA in-situ measurements

MOC transport anomalies at 34.5°S retrieved from moored instrumentations which provide density profiles on each side of the basin across a line of latitude has been used in this paper to search for a validation of the different reanalysis products. The South Atlantic Moc Basin-wide Array (SAMBA) provides estimates of Meridional Overturning Circulation Transport Variability from 2009 to 2017, with a gap from December 2010 to October 2013 (see Chidichimo et al. (2021) for one of the last publications using this data).

3.2 Methods

In this section, we will give a brief overview of the main methods used for this assessment.

3.2.1 SVD for determining EOF patterns and PCs

Here we briefly describe the method of Singular Value Decomposition (SVD) to compute EOF solutions, which do constitute an orthonormal basis in the space of the covariances of the data: each mode explains a percentage of the data variance (Preisendorfer and Mobley (1988), Jolliffe (2003)).
Specifically, the larger the variance associated with the mode, the greater is the weight of that particular mode in the reconstruction of the dynamical behaviour of the data under decomposition. The idea of this decomposition is that we have a matrix whose rows are maps of an ECV at any given time of the dataset, and

columns are time-series at any particular location of the domain under investigation. Supposing the dataset is represented by an $N \times M$ matrix F in which rows $t_1, ..., t_N$ and columns $x_1, ..., x_M$ are entries representing records in time and space respectively, we can calculate the matrix of anomalies A within the dataset by subtracting the time-average over the whole time coverage of the dataset:

$$A_{ij} = F_{ij} - \frac{1}{N} \sum_{k=t_1}^{t_N} \delta_{ik} F_{kj}, \qquad i = t_1, ..., t_N, \quad j = x_1, ..., x_M. \tag{3.1}$$

Notice that columns of this matrix have zero mean. The method consists of using this anomaly matrix to construct the covariance matrix R, defined as:

$$R = A^T A, \tag{3.2}$$

which is an $M \times M$ matrix. The diagonal element R_{ii} is the time-variance of the data at the given location x_i, while the off-diagonal element R_{ij} is the time-covariance between the data at location x_i and the data at location x_j. Solving the eigenvalue problem for the covariance matrix (which is a real-valued symmetric matrix) yields an orthonormal basis to decompose the signal in the space of covariances.

$$\sum_{k=x_1}^{x_M} R_{ik} C_k = \lambda^{(i)} C_i, \qquad i = x_1, ..., x_M. \tag{3.3}$$

The eigenvectors C_i of the matrix are M-component vectors which represent patterns accounting for a given percentage $\sqrt{\lambda^{(i)}}$ of the total standard deviation of the signal, and their projections on the anomaly matrix are N-component vectors which represent how they vary in time: the firsts are the M EOFs and the latter the corresponding Principal Components (PCs).
Since the computation of the covariance matrix can be expensive in computational cost, we used a python package that employs Singular Value Decomposition (SVD[5]) (a mathematically equivalent method with less computational cost with respect to traditional methods - Kelly (1988), Cherry (1997)) to determine EOF solutions.

3.2.2 Diagnosing OHC trends

Starting from Temperature data within the datasets (ORAS5 and CMEMS data), we have chosen to calculate the OHC in four different layers: the top 300m, the top 700m, the top 2000m, and the whole water column. The following diagnostics are applied to all these contributions: calculation of the climatology, trend slope analysis, and time-series of globally integrated trends for each ensemble member and the ensemble mean.
For the calculation of each contribution, we convert the Temperature data from Celsius to Kelvin degrees and carry on the integration on the desired layer, multiplying by the constant reference values for the heat capacity and seawater density:

$$OHC_{\Delta z}(x, y, t) = \rho_0 C_p \int_{z_0}^{z} T(x, y, z', t)\, dz' \tag{3.4}$$

[5] `https://ajdawson.github.io/eofs/latest/index.html`

in which we have used the reference density value $\rho_0 = 1026Kg/m^3$ and the heat capacity $C_p \approx 4000J/kgK$. This definition implies that the OHC has units of J/m^2: then, following the traditional definition of OHC calculated as an anomaly to a reference period, we referred our calculation to the baseline ranging from the beginning of 1993 to the end of 1999. In this way our units of measurement for maps of OHC are in J/m^2, and trend slope maps are expressed as W/m^2. By contrast, the globally integrated contributions are in $Joules$, and the trend counterpart in $Watts$. The choice of baseline climatology is an essential step in calculating the OHC mid and long-term trends (Cheng and Zhu (2015)). Unfortunately, this is a topic on which there's no consensus in the literature (see Palmer et al. (2017), Liu et al. (2016), Levitus et al. (2009), Levitus et al. (2012) Balmaseda et al. (2013b), Willis et al. (2004), Abraham et al. (2013), Storto et al. (2016), Cheng et al. (2017) to have just a vague idea of this statement). Furthermore (Cheng and Zhu (2015)), the problem of how this fundamental choice influences the results and uncertainties in the long-term estimation has been raised, and it has been proposed by them to use the Argo period, which goes from 2004 onward, but there is again no consensus in the literature about this delicate problem. The baseline for the calculation of anomalies should be chosen according to the World Meteorological Organization climate standard normals (i.e. the last available thirty-year long period ending with zero - that is 1981-2010), (WMO (2017)). Given the dataset time coverage (not allowing the use of a standard baseline), we chose a baseline period ranging from January 1993 and ends in December 1999: changes are referred to as the pre-Argo era. With this convention, it is strongly evident that globally speaking, Oceans are warming at all depths, with a higher rate when considering the whole column contributions. OHC trends have been estimated using the X-11 seasonal adjustment procedure (see Pezzulli et al. (2005)). Given X_t an input time series (namely, an SST time series), the X-11 method generates the following decomposition:

$$X_t = T_t + S_t + I_t. \tag{3.5}$$

In this expression, T_t is the trend, S_t the seasonal and I_t the irregular component, this latter accounting for the residual variations, such as irregular sub-annual fluctuations. The decomposition is obtained through iterative application of different running means, which mimic a low-pass filter for T_t estimation (like 24-month window running mean) and a seasonal filter for S_t estimation. In addition, the Mann-Kendall test is used to estimate the confidence in the sign of T_t (whether a monotonic upward or downward trend exists), Sen's method to estimate the slope of T_t,(as the median of the slopes of all pairs of sample points), and a bootstrap procedure to estimate the 95% confidence interval of the trend (Mann (1945), Sen (1968), Kendall (1975), Efron and Tibshirani (1994)).

3.3 Results

In this section, we will resume the main results of our study, investigating possible causes for the AMOC regime change, showing how it is possible to interpret it. We then present the global and regional OHC assessment carried out on GREP members from 1993 onward within the C3S_511 framework, which aims to show that, despite the presence of the AMOC regime change, ORAS5 shows consistency with the other reanalyses in the time coverage common to all datasets (from 1993 onward).

3.3.1 The AMOC variability

In this section, we will describe the analysis of the AMOC, proposing possible causes for this decline in circulation strength. Moreover, employing a regime stability indicator, we show that the two different circulation periods are characterized by opposite stability regimes.

The AMOC stream function has been extracted from the ORAS5 dataset basing the calculation on its traditional representation of a zonally integrated, depth accumulated meridional volume transport, as prescribed by equation (2.1).

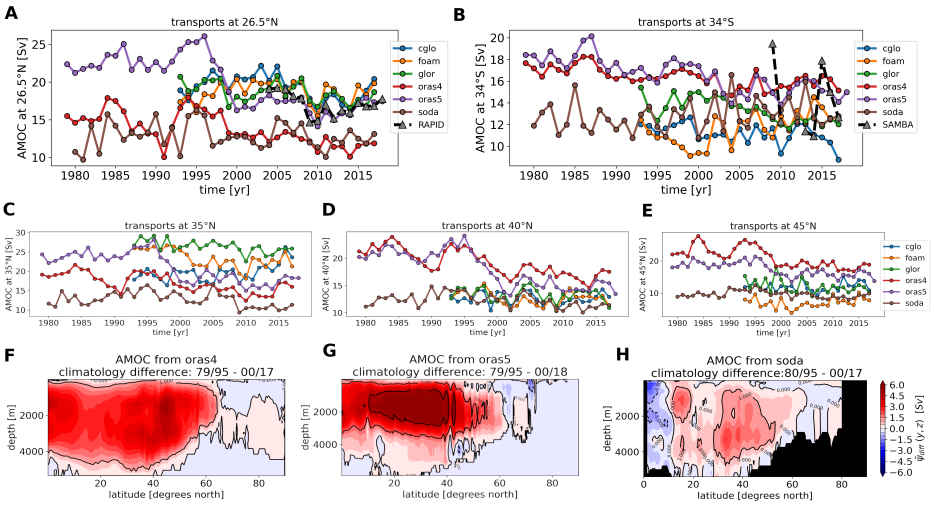

Figure 3.1. Time series of AMOC Strength at different latitudes: 26.5°N **(A)**, 34°S **(B)**, 35°N**(C)**, 40°N **(D)**, 45°N **(E)**, difference between periods of stronger and weaker circulation for the ORAS4 (contours mark 0, 1 Sv) **(F)**, ORAS5 (contours mark -1,0,1,5 Sv) **(G)**, SODA (contours mark -1, 0, 1 Sv) **(H)** data on the entire northern cell of the Overturning Streamfunction.

First we calculated the ensemble mean of the maximum AMOC transport at 26.5° N in ORAS5, GREP, SODA, ORAS4, to compare with the RAPID-MOCHA array AMOC observations (which is shown in fig. 3.1**(A)**). Aside from displaying prominent decadal variability, the most evident feature is a change in its mean state during the mid-1990s characterizing ORAS5 data, quantifiable in about 5 Sv in 5 years, which appear not to be present SODA and ORAS4, neither GREP members

(whose shorter extent - from 1993 onward - does not allow to assess if a similar change shows up also in these data).
One common feature of the time-averaged streamfunctions (see equation 2.1) from different reanalyses consist in a core located in the upper thousand meters of the ocean or so, reaching the maximum value at around 20 Sv in the Northern Hemisphere, with an interannual variability of around 3 Sv over the 1960-2007 period Karspeck et al. (2017).
Seasonal variations of different amplitudes have been largely attributed to wind variations in the past (Kanzow et al. (2010)). One very strong feature, present even in the in-situ data of RAPID-MOCHA, is the sharp negative peak around 2010, and it can be related to large yearly zonal wind stress negative anomalies (model studies by Polo et al. (2014)). Differences across the products become smaller in the last two decades of the time series, all reproducing the negative peak around 2010. Owing to the critical role of the AMOC to the global climate, especially the significant poleward heat transfer, we expect extraordinary consequences on ORAS5 climate (given also the magnitude of changes in it's overturning mean state).

At 34°S, ECMWF products (ORAS4/ORAS5) are closer to the data of SAMBA (fig. 3.1 **(B)**). From inspection of what happens at higher latitudes, it seems that at 35°N (fig. 3.1 **(C)**) the shift is present, at 40°N (fig. 3.1 **(D)**) is masked by the greater variability across ensemble members of ORAS5 (not shown - the line is only the ensemble mean), and then appears again also at 45°N (fig. 3.1 **(E)**), being present with some variations also in the previous version of the reanalysis ORAS4. In order to see what happens at all northern latitudes, we plot the climatological differences between two periods (2000-2018 and 1979-1995) (fig. 3.1 **(F)**, **(G)**, **(H)**). It can be noticed a weakening and shrinking of the upper cell together with the spreading and little enhancement of the lower counterflow cell of the AMOC. ORAS4 and ORAS5 present very similar patterns, and SODA present slight positive differences between two similar periods. The larger differences between the two periods are located at upper and intermediate depths (between 1000m and 3000m) and at midlatitudes (between 20° N and 45° N): in these regions there are clearly complex and competing interactions between the Gulf Stream, and the Labrador Sea waters, winds and net downward solar radiation, which contribute to the meridional overturning variability (Biastoch et al. (2008), Polo et al. (2014) and references therein, Wang et al. (2019)). Discrepancies across models (fig. 3.1 **(F)**, **(G)**, **(H)**) could be due to differences in the modeling of diapycnal mixing (Kuhlbrodt et al. (2007), Zhang et al. (2019)).

This declining signal of the AMOC is a robust sign present in all the ensemble members of ORAS5, and also in its previous version ORAS4. The dynamical decomposition[6] in different contributions at the RAPID-MOCHA section carried on ORAS5 ensemble mean (shown in fig. 3.2), suggests that major changes took place in the Gulf Stream and upper mid ocean contributions, though an excellent agreement with these in-situ data is confirmed for the last period, which unfortunately does not cover the years of changing regime.

This clue guided our analysis toward the Gulf Stream path and also to deep water formation in the Labrador and Nordic (GIN) Sea.

[6]this decomposition has been carried out using CDFTOOLS, which can be found at `https://github.com/meom-group/CDFTOOLS`

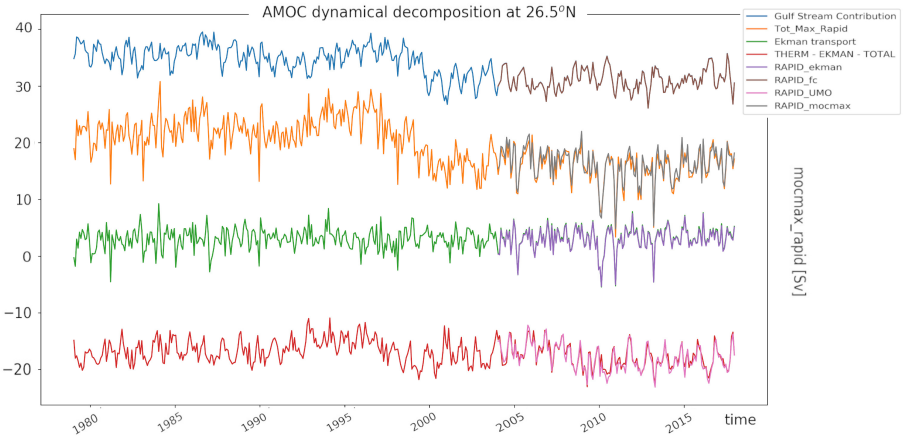

Figure 3.2. Dynamical decomposition of the AMOC signal at the RAPID-MOCHA latitude, carried out with CDFTOOLS (see `https://github.com/meom-group/CDFTOOLS` for details): the total signal (orange and grey curves) is decomposed in the Gulf Stream (i.e. zonal integration restricted to Florida Channel, blue and brown curve), the Ekman transport (involving wind stress over the ocean surface, as in Buckley and Marshall (2016), green and purple curves), the Upper Mid Ocean (i.e. what is remaining subtracting the Ekman and the thermocline part from the total signal, red and pink curves) contributions.

3.3.2 EOF modes for SST, OHC and Wind Stress.

The first two EOF modes from ORAS5 SST and OHC in the upper 300m, together with their corresponding PCs are reported in figure 3.3(panels **(A)**, **(E)** for EOFs, **(B)**, **(F)** for PCs). It shows that the first mode explains about 40% of the

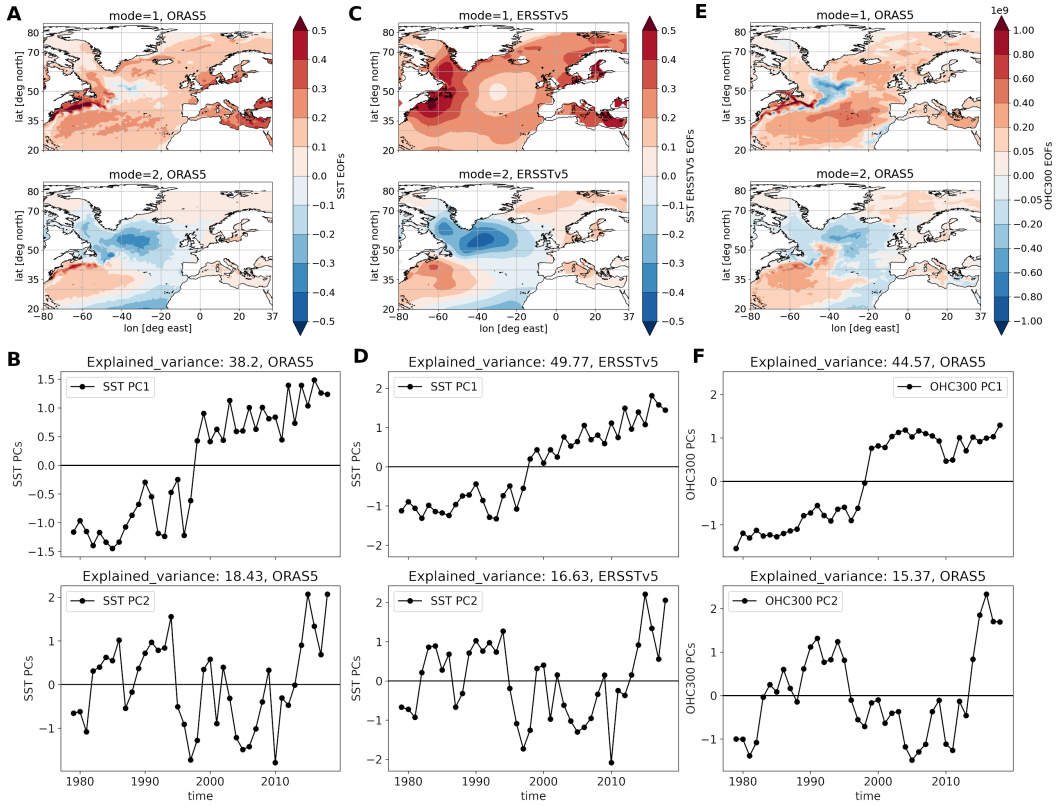

Figure 3.3. **(A)** EOF patterns for the SST, **(B)** corresponding rescaled PCs with explained variances in the title of the subplot. Data from ORAS5; **(C)** EOF patterns for the SST, **(D)** corresponding rescaled PCs with explained variances in the title of the subplot. Data from ERSSTv5 (Extended Reconstructed SST data). It's interesting to note a similar regime change, less pronounced, and more like an increasing trend from the mid-1990s than really a shift as in ORAS5 data; **(E)** EOF patterns for the OHC in the upper 300m, **(F)** corresponding PCs with explained variances in the title of the subplot. Data from ORAS5.

variance of the data, indicating that a significant part of the signals are characterized by a change around 1995 from negative to positive anomalies of the SST and OHC fields. The warming trend covers almost the whole North Atlantic Area, with a cooling signal placed offshore Newfoundland basin. Here we have only shown the first 300m for conciseness and similar features presented also for the contributions at greater depths, i.e. 700m, 2000m, top to bottom integration (not shown). All PCs and EOFs have been scaled with the square root of the eigenvalue to allow having PCs with unitary variances, and EOF patterns with values representative of typical anomaly order of magnitude in the units of measurement for the variable, i.e. °C for the SST, J/m^2 for the OHC values, $Sv = 10^6 m/s$ for mass transport. Similar kind

of regime change feature, but with less pronounced intensity is presented as well in lower resolution SST data (an objective reconstruction ERSSTv5, fig. 3.3 **(C)**, **(D)**): in this case it seems more like an increasing trend in the second period, than really a change between two regimes as it appears in ORAS5 data. Higher modes explain less variance of the data, being consistent with both previous EOF SST patterns (Jung et al. (2017)).

Retaining significant information about patterns of circulation in the basin (see Fontela et al. (2016), fig. 1), the second mode of either SST (fig. 3.3 **(A)**, **(B)**) or OHC300 (fig. 3.3 **(E)**, **(F)**) EOF decompositions explain about the 15-20% of the variance of the data. It shows a tripole pattern with centers located respectively in the Western Tropics (Gulf Stream), Subpolar Gyre Area (Labrador Sea and Newfoundland basin), and the Eastern Northern part (Nordic Seas and Mediterranean Sea). Similar pattern, reversed in sign, is shown in the third EOF mode (not shown), though with less percentage of explained variance. The corresponding PC time series shows the same alternance between positive and negative phases, implying strong interannual to decadal variability (i.e. on shorter time scales with respect to the leading mode).

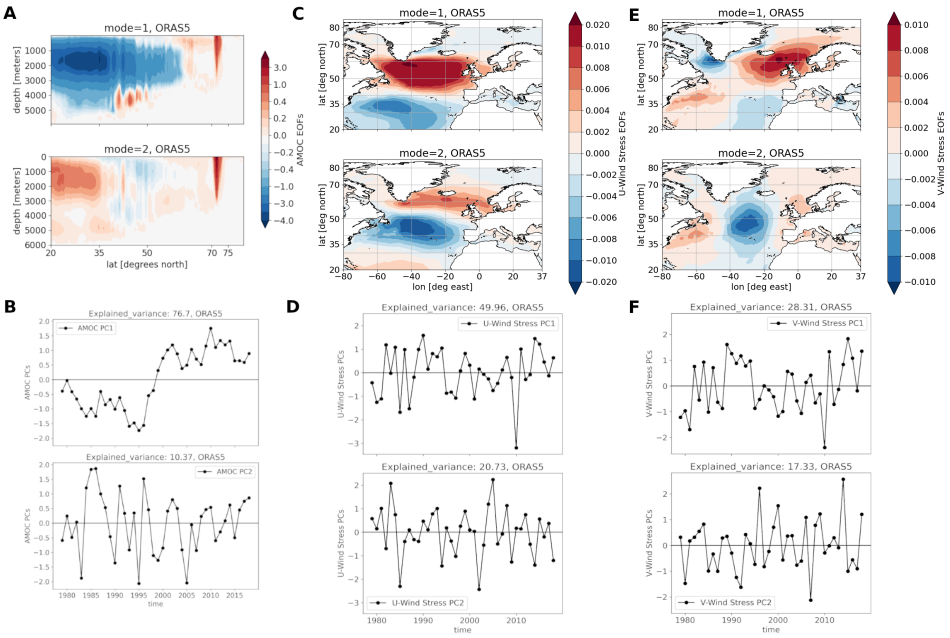

Figure 3.4. **(A)** EOF patterns for the AMOC streamfunction, **(B)** corresponding PCs with explained variances in the title of the subplot, data from ORAS5; **(C)** EOFs patterns for zonal component of wind stress, data from ORAS5; **(D)** correspondent PCs rescaled to have unitary variance; **(E)** EOFs patterns for meridional component of wind stress, **(F)** correspondent PCs rescaled to have unitary variance, data from ORAS5.

It is interesting to note that the fourth mode (for SST or OHC), only represents 6% of variance, though it is the only one that displays a zonal oscillation involving the European marginal seas (not shown). This zonal variability could be representative of the eastern and western oscillation of the spatial pattern of zonal salinity redistribution (Stendardo et al. (2016)). A similar mechanism was observed for the

atmospheric counterpart in the North Atlantic Oscillation (NAO) (Luo et al. (2010)), but in our case it seems to be in relation with the Gulf Stream (GS) shift and Deep Water Formation (DWF) in high latitude seas, that are discussed more in detail in next sections.

EOF analysis for the AMOC (cfr. fig. 3.4 **(A)**, **(B)** - negative values in the PC time series indicate stronger northward transport), reveals that a change is present also in its leading mode, and accounts for 76% of the total variance of the signal. The second and third (not shown) account for a smaller percentage of explained variance but showing the same tripole pattern, which is likely associated with the tripole mode observed for SST and OHC. To understand the mechanisms that are responsible for the change of SST, OHC and AMOC, we first look at wind stress EOFs patterns (figures 3.4 **(C)**, **(D)**, **(E)**, **(F)**). It is interesting to note that both in the zonal and meridional components, there is a marked negative peak around 2010, which has a strong impact also on AMOC variability (Polo et al. (2014)) (first zonal and meridional modes account respectively for the 50% and 30% of data variance). The second for wind stress components show strong interannual variability, reflecting the faster timescales of the winds, and capturing respectively around the 20% and 6% for the zonal component and the 17% and 10% of the variance for the meridional component. These modes have patterns which can be related to subpolar-subtropical gyre variability (Häkkinen et al. (2011) - see also the discussion in the Labrador Sea section about the AMOC regime change). Significant correlations are present between the leading modes for the AMOC and SST, OHC, while for the wind stress the modes seem to be less (negatively) correlated, and with less significance (see table 3.1).

Variables	SST	OHC300	OHC700	OHC2000	OHC6000	τ_u	τ_v
Pearson R	0.840	0.840	0.907	0.937	0.941	-0.141	-0.126
P Value	0.999	0.999	0.999	1.0	1.0	0.616	0.562

Table 3.1. Correlation coefficient between AMOC leading mode and leading modes for the other variables.

However, higher significance in correlations have been found between the AMOC leading mode and PC2, PC3 of the wind stress components (discussed in the following - section on Deep Water Formation). In terms of physical processes, as pointed out by Häkkinen et al. (2011), strong positive (negative) wind stress curl anomalies over the subpolar (subtropical) gyre region should enhance the strength of subpolar gyre, at the expenses of subtropical gyre, favouring the entering/blocking of salt anomalies propagation toward the eastern part of the Atlantic, ultimately affecting also AMOC variability and stability.

As in previous studies, our analysis shows that the wind is related to the short time scales variations for the AMOC, rather than those addressed in the present paper, which are mid-long term climatic fluctuations (Polo et al. (2014)). Indeed we find low correlation between leading PCs of AMOC decomposition and PCs of wind components, suggesting that the change in ORAS5's North Atlantic circulation is driven by NAO induced buoyancy variations, rather than a direct oceanic response to a change in the wind forcing (Robson et al. (2012)).

Their study suggests that once the wind stress induced Ekman transport component has been removed, there is more meridional coherence between AMOC signals at low (20-30°N band) and high latitudes (50-55°N band). However, our results show that wind variations have a less important role, because the effect of winds is present only in the PC3 of the AMOC EOFs (not shown), inconsistently with Wang et al. (2019) that uses a regional model with higher resolution. It is likely due to the differences between resolutions of the data used in the present paper (1/4° - eddy permitting), and the data in Wang et al. (2019) 1/12° - eddy resolving with the inclusion of smaller scale processes.

One notable difference between the upper layer and the deep ocean is that higher modes in OHC2000, OHC6000 exhibit prominent long-term decadal variability, which constitute a distinguishing factor with respect to SST, but at the same time explaining less variance percentage (figures not shown). However, the quite high correlation (see table 3.1) between the first EOF and PC among these variables is clearly due, at a first level of approximation, to changes in the mid-1990s following a persistent positive phase of the NAO.

3.3.3 The Gulf Stream Path Variations

Gulf Stream (GS) path variations have been shown to be closely tied to AMOC variability in reanalyses and coupled general circulation models. For example, De Coetlogon et al. (2006) found that northward GS path shifts lag positive NAO phases by 0-2yr, albeit stronger correlations have been found with AMOC variability as well. These results were based on a definition of the GS Index (GSI) relying on the temperature at 200m, though the temperature at 400m depth has been shown to be a good proxy to describe front variations as well. Indeed, later studies by Joyce and Zhang (2010) used this slightly different formulation for the index, finding that when the AMOC is strong, the GS path tends to be more southerly oriented. In this section, we investigate the role of Gulf Stream path change in the AMOC variability. The Gulf Stream Index, constructed from the temperature field at 400m depth (Joyce and Zhang (2010)), (fig.3.5 A, B in which northward shifts are identified by positive values in the time series for the PC1), show similar variabilities as the AMOC in the leading modes, indicating a repentine variation of the front of the Gulf Stream Separation path as a response of NAO prolonged positive phase prior to 1995, which drives North Atlantic state as a response of the subpolar-subtropical gyre interplay (see discussion in the next section).

Moreover, secondary modes show as a general characteristic a peak around 2010 which can be addressed to wind stress components. The tilt of the Gulf Stream path is further investigated by looking at climatology of the barotropic stream function (which is the sum of depth-integrated zonal - u dy and meridional - v dx volume transports - fig. 3.6 **(A)**, **(B)**). It is evident a general weakening of the circulation pattern when looking at the two periods.

The subpolar gyre expands southwards and the subtropical gyre shrinks in the second period compared to the first period (fig. 3.6 **(C)**). Thus, there's a sort of breathing of the gyre circulation systems in this area, in the sense that when SPG shrinks at the expenses of the STG, also GS would be affected, being its path in the middle of these two gyres (Lozier and Stewart (2008)). Moreover, it can

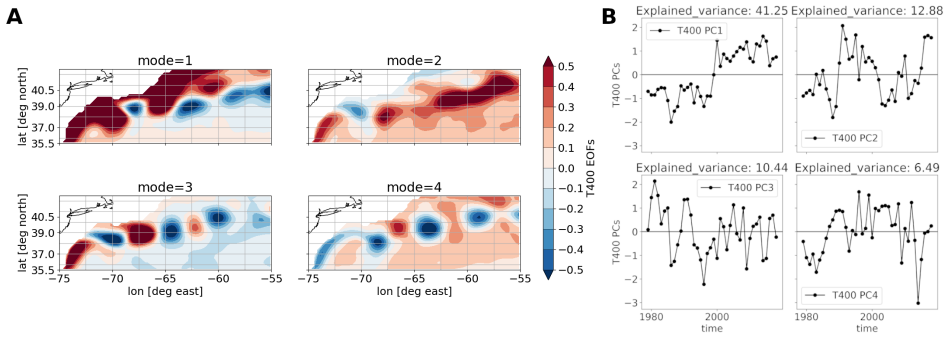

Figure 3.5. **(A)** EOFs of the temperature field at 400m, **(B)** corresponding PCs, from ORAS5 data. The Gulf Stream Index is the first mode in the decomposition.

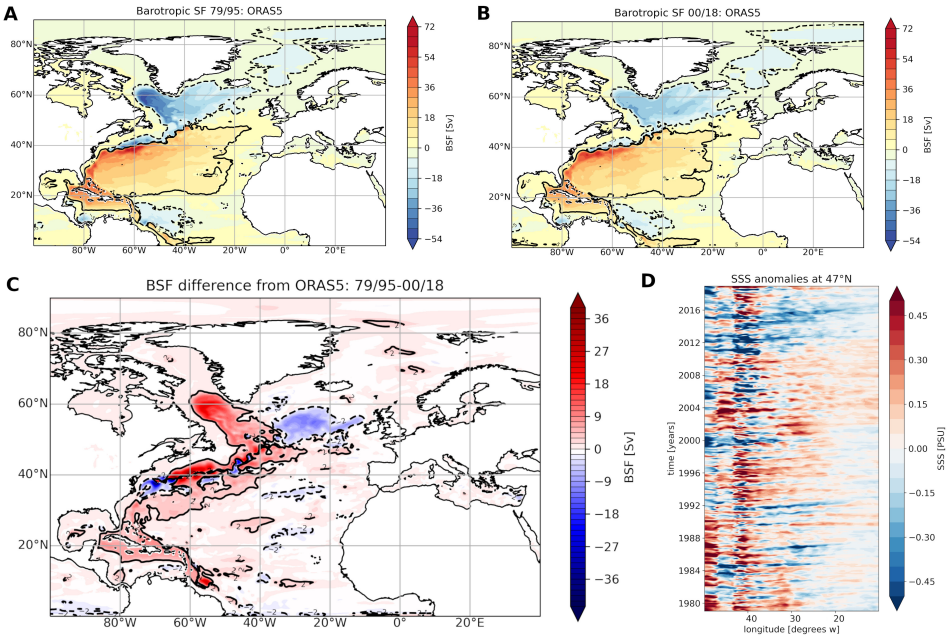

Figure 3.6. Barotropic Stream Function (BSF) in the two periods. The GS path is marked by the black contour levels (-5 Sv the dashed, 5 Sv the continuous). Positive values indicate clockwise circulation while negative ones counter-clockwise circulation. Panel **(A)** shows the average over the period of stronger AMOC, while panel **(B)** shows the average over the weaker AMOC period. Panel **(C)** shows the difference of the modulus of **(A)** minus the modulus of **(B)**, in such a way to indicate, regardless of the clockwise or anticlockwise circulation, that the first period has a stronger circulation than the second one. Dashed and continuous contours level in panel **(C)** indicate respectively difference of -2 and 2 Sv. Panel **(D)** shows the longitude-time Hovmoller diagram of Salt at 47 °N, showing the redistribution between the west and the east after the AMOC regime change.

be noticed that in the first period deep convection processes in the Labrador are more intense and spatially concentrated, while the second period is characterized by the entire pattern having less strength, and being more delocalized. At the same time, the strength and extent of circulation over the eastern Nordic Seas (GIN) seems to stay unaltered passing from one period to the other. Quantifying if this behavior is intermittent or it has a multidecadal typical timescale would require longer timeseries, in order to have more oscillations like the one we observed in the mid-1990s.

The difference between the two periods, shown in figure 3.6 **(C)**, confirms all the above-mentioned observations, showing major changes in the Labrador Sea and along the GS path. The reduction of intensity of SPG circulation has been linked to NAO and wind stress curl variations (Robson et al. (2012), Häkkinen et al. (2011)), which should favour the intrusion of salt anomalies toward the eastern part of the north Atlantic. Indeed we can see from fig. 3.6 **(D)** (showing the hovmoller diagram of Sea Surface Salinity across 47°N), important salinification of the eastern part of the section in the pentads following years of changing regime.

This depletion of salt from the western part of the basin, through the well known salt advection feedback, causes the AMOC to transport less salt into the SPG, which thus becomes cooler and fresher in the second period. Diminished deep convection within the Labrador Sea results with less Deep Water Formation (DWF), contributing to a further reduction of the AMOC strength (Weijer et al. (2019)).

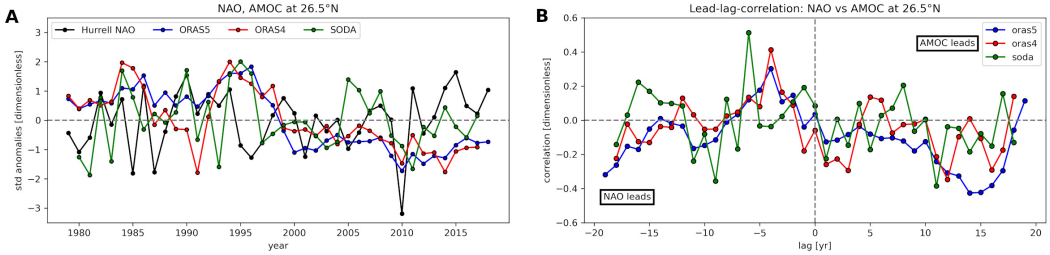

Figure 3.7. **(A)** time series for the NAO index, AMOC at 26.5°N from ORAS5 (blue), ORAS4 (red), SODA (green). **(B)** lag correlation of the AMOC strength time series of each model vs annual NAO index. The NAO index is from `https://climatedataguide.ucar.edu/climate-data/hurrell-north-atlantic-oscillation-nao-index-station-based`. For all the time series, anomalies normalized to the standard deviation in time were used, in order to have dimensionless and directly comparable values. It's interesting to note that all products indicate NAO driving AMOC variations with a lead-time close to 5 years.

The phase of higher AMOC strength at 26.5°N, higher salinity in the west Atlantic, and stronger deep convection in Labrador Sea (as we will see in the next section), overlaps with the well known period of persistent positive NAO anomalies (differences across the models are shown in figure 3.7, panel A - all time series have been normalized by calculating the anomalies and dividing by their interannual variability). Moreover, volume transport time series show a positive correlation at 6 or 5 year negative time lag, indicating that NAO variations are somehow driving AMOC variations (SODA presenting a slightly larger lead/lag time than ORAS5, ORAS5 - figure 3.7, panel B). In the paper by Putrasahan et al. (2019), it is shown

with MPI-ESM coupled model that, even if freshwater is still the major contributor to AMOC variability, enhancing atmospheric resolution from 1° to 0.5° can cause further freshening of the North Atlantic indirectly via winds variability. Indeed, reduction of winds causes changes in the wind-driven gyre circulation, modifying the salt transport across the basin. A sketch is depicted in figure 3.8. In particular, when the NAO is

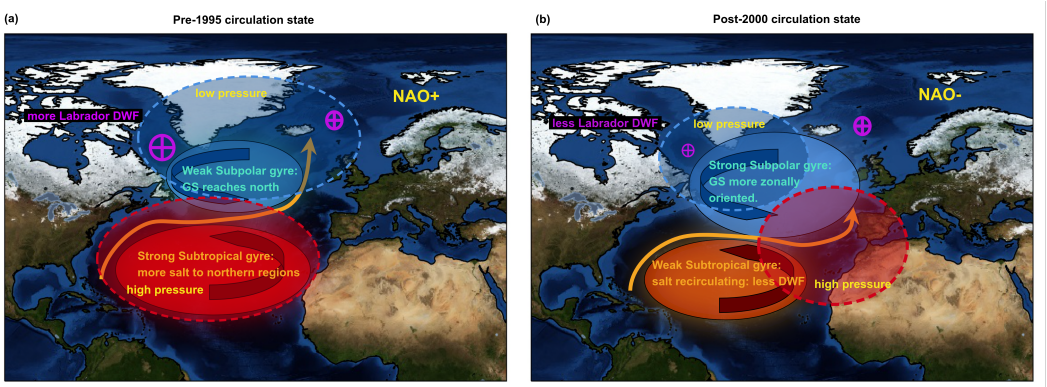

Figure 3.8. **(a)** Persistent positive NAO phase prior mid-1990s enhancing STG, allowing salty water to reach northern latitude - stronger Deep Convection in the first AMOC period, **(b)** oceanic response in correspondence to mostly negative or neutral NAO phase, where deep convection is reduced.

in its positive phase, it favours a stronger STG circulation, at the expenses of SPG, permitting in this way to propagate salt anomalies northward. Conversely, when the NAO shift to more negative or neutral conditions, the SPG circulation enhances, with the salt recirculating in tropical regions, triggering consequent reduction in DWF, thus indirectly affecting AMOC strength. Given the fact that EOF modes for wind stress components do not show any particular change, we decided to focus our efforts on DWF in high latitude seas, especially because of their well-established role on AMOC variability (Buckley and Marshall (2016)).

3.3.4 Labrador Sea DWF processes

Densification of near-surface waters and net downwelling from the upper ocean to mid depths have been widely accepted as the ocean response to buoyancy loss in high latitude seas, impacting significantly the AMOC variability (Johnson et al. (2019) and references therein). Moreover, numerical experiments have also shown that such remote effects can influence the mid-long term variability of deep water convection and production in this sub-basin for the entire North Atlantic (Straneo (2006), Polo et al. (2014)).

This section explores the impact of Labrador Sea deep convection on the AMOC variability.

With the Gulf Stream weakening from one period to the other (fig. 3.6), there's less advection of heat and freshwater from the subtropical to subpolar regions, changing buoyancy of water masses, mixed layer depths and ocean-atmosphere fluxes (these latter being also NAO driven) in the high latitude seas.

Indeed, looking at Figure 3.9, which shows, respectively, from top to bottom

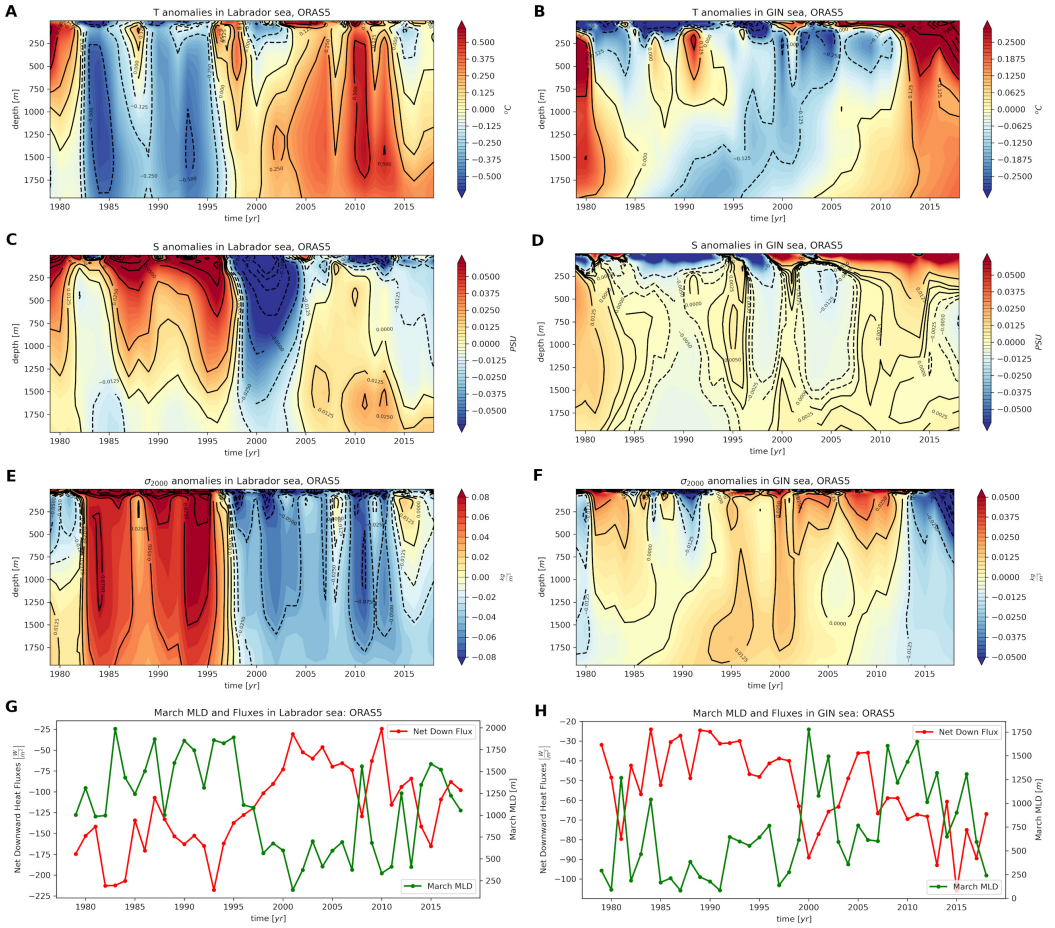

Figure 3.9. Labrador [125°W, 120°W, 55°N, 60°N] **(A, C, E, G)** and Nordic [170°W, 5°E, 72°N, 77°N] **(B, D, F, H)** seas from ORAS5: Temperature **(A, B)**, Salinity **(C, D)**, σ_{2000} **(E, F)** anomalies depth vs time Hovmoller plots. March MLD (0.01 density-based criterion) and yearly-averaged surface net downward heat fluxes are shown in **(G, H)**.

temperature, salt, σ_{2000} anomalies and March MLD together with net downward heat fluxes, both temperature and salinity anomalies patterns combine into a pattern for density which is characterized by a flip from positive anomalies in the first period to negative anomalies in the second period in the Labrador Sea interior. In particular, in the early period, the densities in Labrador and GIN seas (figure 3.9 **(E)**, **(F)**) have similar variability, and in the later periods, the density anomalies in these two seas are out of phase. This phase shift seems to have a deep temperature-driven origin, rather than a salt origin (see fig. 3.9 **(A)**, **(B)**, where near the surface temperature patterns are in phase, while under thousand meters they become out of phase - the salt patterns in fig. 3.9 **(C)**, **(D)** remaining out of phase mostly at all depths above 2000m).

These temperature (and hence density) flipping patterns are consistent with less buoyant waters in the first period than in the second in Labrador Sea, minimizing in a vigorous way the sinking mechanism responsible for western DWF that is consistent with Karspeck et al. (2017), showing same patterns of variability in ORAS4 and in situ measurements from Yashayaev (2007), with the largest change occurs between 1995 and 2000.

The temperature and salinity anomalies at depth demonstrate that there are warm and salty water's intrusions in the Labrador Sea, around 1980 and 2000, alternating with freshwater as previously observed also in other reanalysis products (see the analysis on SODA carried out in the period 1958 to 2005 by Häkkinen et al. (2011)). These have been connected to wind stress curl variability and NAO variations, which provide a mechanism by which strong positive (negative) wind stress curl anomalies over the subpolar (subtropical) gyre region enhance the strength of subpolar (subtropical) gyre, at the expenses of subtropical (subpolar) gyre, inhibiting (allowing) the advection of salt anomalies toward the high latitudes.

During the weak AMOC period, weak positive (negative) wind stress curl anomalies over the subpolar (subtropical) gyre are presented, enhancing the strength of subtropical at the expenses of subpolar gyre strength and extension, favouring the intrusion of salt anomalies toward the eastern part of the Atlantic (fig. 3.6 **(D)**), consistently with Häkkinen et al. (2011). We notice that the Hovmoller diagram of salt in figure 3.6 **(D)** (sea surface salinity at 47°N) is not directly representative of the Labrador Sea salinity itself, but more of the incoming/outcoming salt within the regions further north (i.e. Labrador on the western part, Nordic Seas on the eastern part). Indeed, water at 47°N, as suggested by BSF has to encircle the SPG cyclonically before eventually circling in the Labrador and nordic seas.

Also, by looking at EOF 2 and 3 of the wind stress components in ORAS5 data (fig. 3.4 **(C)**, **(D)**, **(E)**, **(F)**) we found positive correlations with the AMOC leading mode, with correlation coefficient and p value percentage respectively of (0.184, 0.744) for the PC2 on zonal wind stress and (0.164, 0.688) for the meridional component, and (-0.107, 0.491) for the zonal and (0.264, 0.9) for the meridional component for PC3. Long persistence of positive NAO phases have been reported to be closely connected with the AMOC slowdown during the mid-1990s Robson et al. (2014), with the ocean providing a lag response to atmospheric processes. This process brought salt to the GIN sea, which has been released in the second period, preventing the AMOC from a complete shutdown.

Surface heat fluxes can also play a role in modulating the deep convection

processes. The time series of net downward heat flux anomalies shows the same variability as the AMOC, being characterized by negative anomalies prior to the mid-1990s, and by positive anomalies afterwards. The reduced radiative energy influx in the second period through the ocean's surface, driven mainly by the atmosphere, can be thought to be one of the triggering factors for deep water formation reduction, having nonlinear and complex feedback on the AMOC variability as already stated above. Indeed, EOF analysis has shown significant correlations between modes of variability of the AMOC from 20° N to 65° N with subsurface temperature and density in the North Atlantic, and these correlations are strongly linked to the net downward surface heat fluxes, western boundary currents, deep convection and subpolar gyre variability (Huang et al. (2012)).

Therefore, the switch from positive (negative) to negative (positive) anomalies for density (net downward heat fluxes and temperature) can be viewed as a drastic reduction in the pushing action exerted on the AMOC by the Labrador Sea North Atlantic Deep Water (NADW) formation. This NAO driven change in buoyancy, owing to a tilting behaviour of the Gulf Stream, is responsible for the less apparent but present shift in the upper mid ocean contribution for the dynamical decomposition shown by fig. 3.2. At the same time, continuation of DWF in GIN Sea (fig. 3.9 **(B)**, **(D)**, **(F)**, **(H)**) prevents the AMOC from a complete shutdown.

3.3.5 Stability Regime Indicator

While in most climate models there are predictions but no consensus on the AMOC slowdown or shutdown, the sharp regime change of the AMOC could be related to the multistability of the AMOC in the two periods, which we decided to assess by comparing with GREP members, which have a shorter time extent but are virtually closer to ORAS5 (from the point of view of the ocean model, horizontal and vertical resolutions, assimilated data and forcing). We thus relied on the indicator defined in section 2.1.3 to interpret the change of the AMOC as a modification of circulation regime. In an overall view, the mean over the whole dataset time coverage yields a stable AMOC, with a positive value for $\Delta M_{ov} = 0.15Sv$. However, splitting into two periods the calculation, a different description in terms of the AMOC stability regime arises: it passes indeed from a stable to an unstable regime prior and after mid-1990s (see figure 3.10 for its stability diagram representation). Particularly, during the first period, we found a stable regime, with value for $\Delta M_{ov} = 0.36Sv$, while in the second we found a value for $\Delta M_{ov} = -0.06Sv$.
For the second period, a divergence of the AMOC-induced freshwater transport ($\Delta M_{ov} < 0$) indicates an unstable regime of the Atlantic Overturning. This unstable regime arises in response to buoyancy perturbations due to positive feedback with salinity advection, as shown by the Labrador Sea in figure 3.9. Our results are consistent with an unstable AMOC shown in Liu et al. (2017) and references therein, when comparing reanalyses (unstable AMOC) and CMIP models (stable AMOC). This criterion from box models ignores the freshwater transport by the gyre circulation (Gent (2018)), which is shown (Mecking et al. (2017)) to be twice as large as the overturning transport at 33°S. Moreover, the representation based on zonally averaged quantities filters out all the possible east-west variabilities. For this reason, we tried to face the question from an alternative point of view, i.e. looking at Surface

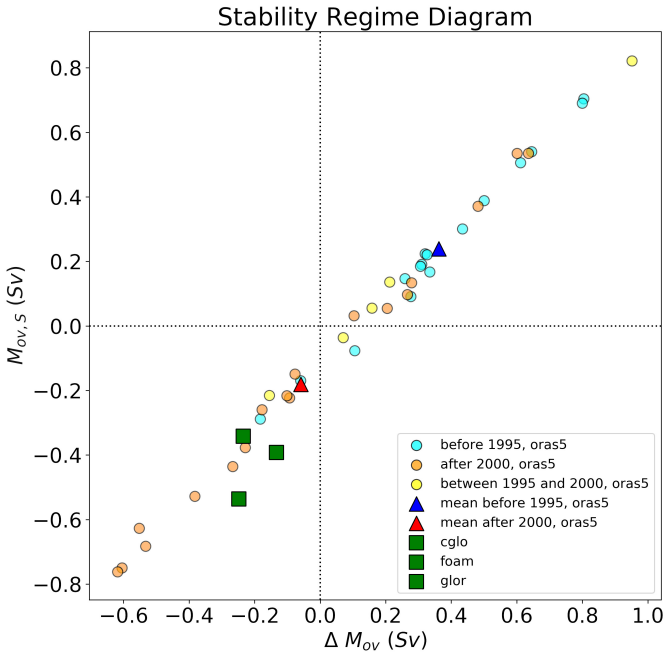

Figure 3.10. Stability regime diagram for the AMOC in ORAS5 and in CMEMS.

Kinetic Energy Extreme Events, which is discussed in the next section.

3.3.6 Surface Kinetic Energy Extreme Events

All the previous analyses have shown that the declining signal in the mid-1990s of the AMOC, which is related to the weakening of the deep convection, may induce significant modifications in the Gravitational Potential Energy (GPE) (Wunsch and Ferrari (2004)). To maintain the energy balance of the ocean circulation, this loss of buoyancy (GPE) needs to be compensated by energy gain elsewhere in the Kinetic Energy (Kuhlbrodt et al. (2007)). We thus defined a kinetic-energy based diagnostic that tries to search for this balancing mechanism. We supposed that there's a link between the stability regime change and the redistribution of Surface Kinetic Energy Extreme Events (SKE-EEs), which are defined as the surface kinetic energy at each location that exceeds by three times the standard deviation (following lines of Seneviratne et al. (2012)) based on the following formula,

$$N = \sum_{n=t_1}^{t_n} \Theta\left(|\mathcal{K}_n| - 3\sigma_K\right) \tag{3.6}$$

where N represents the extreme surface kinetic energy, $\mathcal{K}_n$ is the value of surface kinetic energy at the time n (defined as $\mathcal{K}_n = \frac{1}{2}\left(u_n^2 + v_n^2\right)$), σ_K is the standard deviation of the time series on the time extension of the signal, and Θ is the Heaviside step function, which equals one if its argument is higher than zero and

equal to zero otherwise. We split the counting of SKE-EEs into two time periods as before. We have shown that the volume transport sharp decline is closely related to a partially inhibited Labrador Sea deep convection. In particular, within this semi-enclosed basin, there's a conversion of GPE into KE through DWF, so reduced buoyancy anomalies would reduce the energy reservoir for the AMOC strength. We look at SKE-EEs to understand the redistribution of the energy, noticing that the reduction in the volume transport (and its cascade effect on Labrador Sea DWF) triggered the onset for surface SKE-EEs redistribution in the North Atlantic domain. In the first period, with higher volume transport and the AMOC is in its stable regime, there are more SKE-EEs in the Labrador Sea. In the second period, when the volume transport of the AMOC is reduced and in its unstable regime, which admits multiple equilibria, there's more eddy activity in the European Sector of the North Atlantic, as can be noticed from Figure 3.11A: this could be something happening also at small scales in the Mediterranean Sea (Schroeder et al. (2016)), with salt redistributing across the east-west direction.

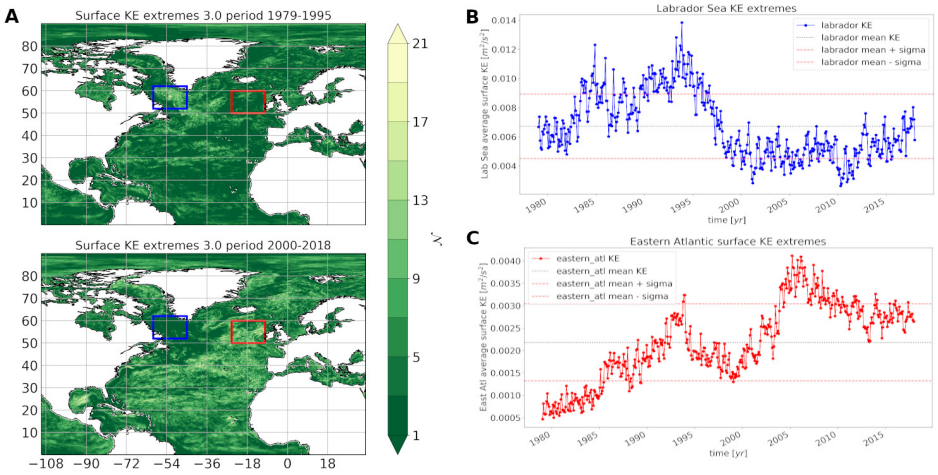

Figure 3.11. **(A)** Surface Kinetic Energy extremes count for the two periods. Standardized anomalies are extracted from the KE field, and the colormap shows the number of values which exceed 3 times the standard deviation in the two periods, **(B)**: spatial average of KE in the Labrador Sea box [-60° W, -45° W, 52° N, 62° N], **(C)**: spatial average of KE in the eastern Atlantic Box [-25° W, -10° W, 50° N, 60° N].

This triggering is still visible but less pronounced by doing the spatial mean on the respective boxes, as can be noticed in Figure 3.11B, 3.11C, where the threshold for the detection of the extreme events has to be lowered to one standard deviation, because of the spatial average which tends to smooth out fluctuations in the maxima and minima of the series. The tilt of the Gulf Stream path is synchronized with the time series for SKE-EEs redistribution: from the energetic viewpoint, it's like there's a displacement of eddy activity from the west to the east part of the North Atlantic, balancing the loss in the south to north mass transport. This activation of the eastern part of the Atlantic is indeed coherent with an observed eastward redistribution of the salinity advection along the North Atlantic Current and Evaporation-Precipitation (E-P) balance, which has been addressed to the intensification of the subpolar gyre

with a positive NAO phase (Stendardo et al. (2016)). In the same paper, it has been observed an anomalous interannual variability of the salinity over the last 20 years (they look at the period 1993-2012), which is not directly driven by changes in the E-P forcing (Stendardo et al. (2016) figure 13 therein). This SKE-EEs redistribution could, in principle, provide a mechanism to modify the salt advection, reducing salt in the area where the precipitation is dominant (west of Mid Atlantic Ridge) and increasing it in the area where there is more evaporation (east of Mid Atlantic Ridge).

3.3.7 Flux-Adjustment induced hysteresis cycle of the AMOC

Figure 3.12 shows normalized anomalies of AMOC strength vs Labrador Sea heat fluxes.

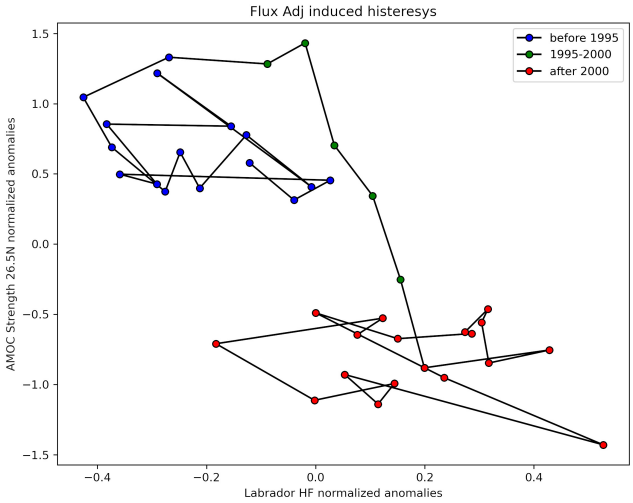

Figure 3.12. Normalized anomalies of AMOC Strength vs Labrador Sea heat fluxes.

These anomalies were constructed by subtracting the monthly climatology from each month, dividing by the standard deviation of the time series along the temporal dimension. Colour coded temporal evolution shows that the arrangement of the scatter plot of these anomalies resembles half of the hysteresis cycle induced by flux-adjustment in the Labrador Sea (Figure 4 of Rahmstorf (1996)), and ORAS5 has been treated with heat flux adjustment procedure to reduce the bias on SST in regions where there are strong gradients (Figure 7 of Tietsche et al. (2020)). This adjustment, carried out in an area sensible for DWF, could have over-amplified an underlying NAO-induced the AMOC shift.

3.3.8 Restriction to the CMEMS period and analysis of the OHC at the global scale

We have carried on the analysis assuming that the AMOC strength change is a genuine dynamical process taking place between two stationary states. Indeed there are few uncertainties about this shift of regime, all of which could be issued to the many technical details of the reanalysis production (parametrizations of subgrid physical processes, data assimilation scheme, even the data ingested in the assimilation procedure, or the flux adjustment procedure used to reduce the bias in regions where there are high-temperature gradients). The use of the stability indicator could be either too weak to be sure if this process is a bona fide new physical process or something else (see (Gent (2018)) for an interesting comment about this point). Moreover, the comparison with GREP members is possible only on the period starting from 1993 onward, and only later with in-situ data (i.e. data from the RAPID-MOCHA section). In the framework of the C3S_511, it has been possible to assess that, despite the presence of the AMOC regime change, ORAS5 still performs well when compared with other state-of-the-art ocean reanalysis products.

Ocean Heat Content: top 300m, top 700m, top 2000m, top to bottom

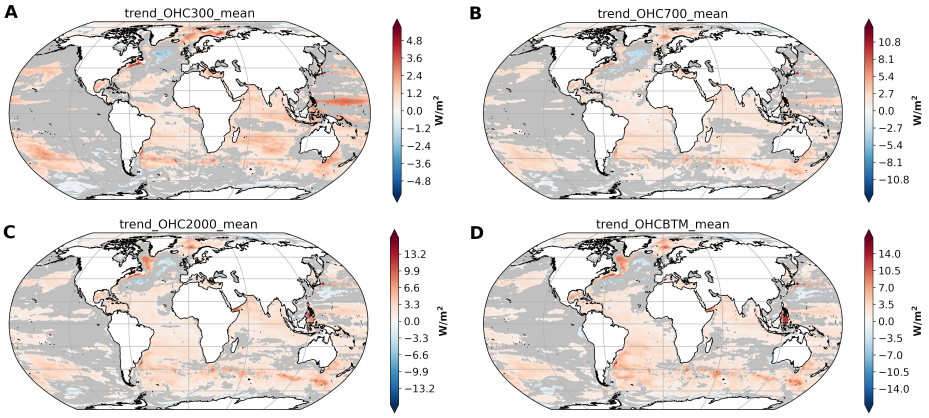

Figure 3.13. Trend slopes for OHC at different depths: Ensemble mean. **(A)** the upper 300m contribution, **(B)** the upper 700m contribution, **(C)** the upper 2000m contribution, **(D)** top to bottom integration. The extremes in the colorbar have been set different for the sake of visibility.

Figure 3.13 shows the trend slope map estimated with the methods discussed in previous sections for the ensemble mean of CMEMS data (ORAS5 included). The linear trends of the OHC from 1993 to 2018 shows a general warming signal globally, with cooling trends located in the North Atlantic Ocean, the Southern Ocean and the eastern Pacific Ocean. Notice that the linear trends that do not pass the 95% significance level are shaded in silver: this is applied to all the linear trend analysis in this paper.
The linear trend in different ensemble members show similar patterns with warming signals in most areas, especially in the eastern Tropical Pacific, the Indian Ocean and Mediterranean Sea (figure 3.13). Cooling signals are located in the North Atlantic,

Southern Ocean and the western Pacific Ocean. The amplitude of the linear trend is different in terms of distinct ensemble members, and again, increases with depth (not shown for conciseness).

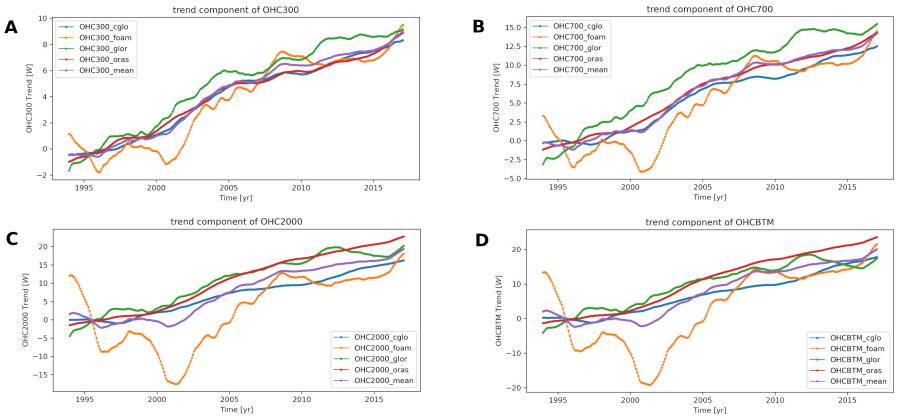

Figure 3.14. Trend components estimated for each member and for the ensemble mean. **(A)** the upper 300m contribution, **(B)** the upper 700m contribution, **(C)** the upper 2000m contribution, **(D)** top to bottom integration.

depth/model	CGLO	FOAM	GLOR	ORAS	ensmean
OHC300	0.40±0.01	0.45±0.05	0.47±0.02	0.38±0.01	0.42±0.02
OHC700	0.60±0.036	0.69±0.12	0.80±0.04	0.65±0.02	0.69±0.04
OHC2000	0.77±0.04	1.02±0.40	1.07±0.07	1.12±0.03	0.95±0.09
OHCbtm	0.84±0.05	1.20±0.46	0.97±0.08	1.15±0.03	1.01±0.11

Table 3.2. Summary of trends and standard deviation expressed in W/m^2 for all the depths, errors estimated with a bootstrap procedure as described in the text.

Figure 3.14 and Table 3.2 collect the landscape for globally integrated trends. All the ensemble members show increasing trends from 1993 to 2018, including OHC300, OHC700, OHC2000 and OHCBTM, with different trends amplitude. The disagreement is mainly expressed in interannual variability with FOAM extremely different from the rest of the members. Spatial pattern differences in the linear trend maps between single members and ensemble mean showed that the main discrepancies are mainly located at western boundary areas and in the southern ocean region (not shown).
However, the order of magnitude of the increasing trend will reach 1022 $Joules/year$, equivalently to about 1 W/m^2 that is coherent with the value deduced from the more recent scientific literature (Meyssignac et al. (2019)).

OHC at different depths in the Atlantic-Mediterranean composite domain

Looking at the restricted domain of the Atlantic-Mediterranean as a whole system, differences across the members become more prominent when the considered depths are greater. All members agree on the general pattern for the slope of linear trends

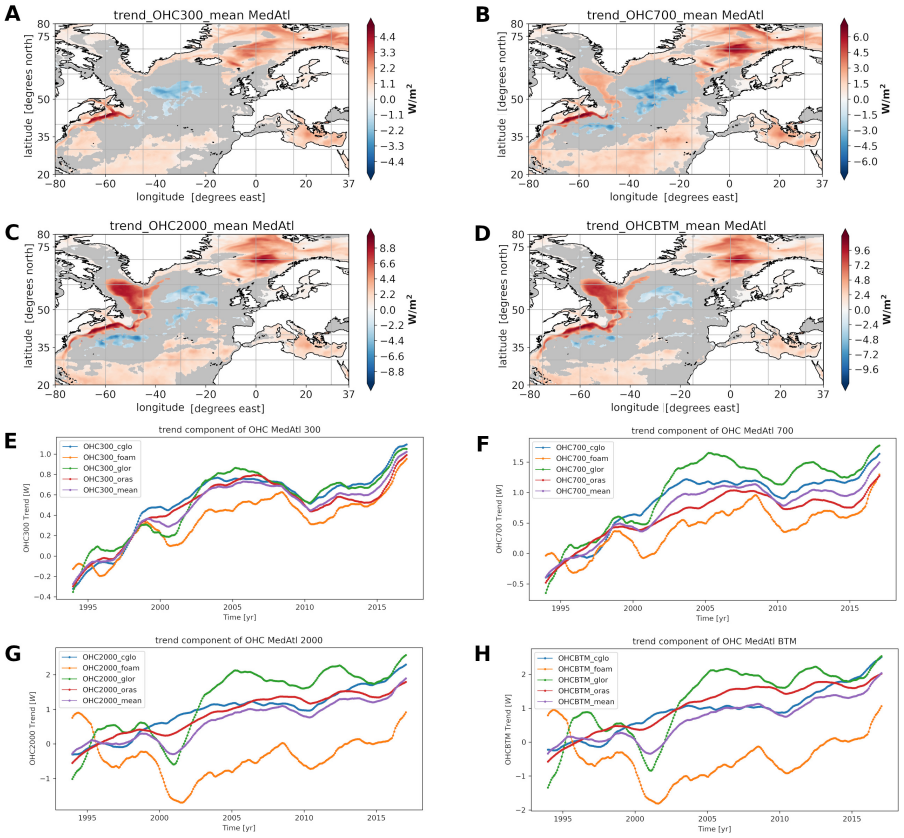

Figure 3.15. From top to bottom: Mean slope of the trend in the selected domain. Different extremes in the colorbar have been used for the sake of visibility. It is possible to notice that the pattern is more or less the same for all depths, but with different rates (the higher the greater the depth is). Trend components for the connected domain Atlantic+Mediterranean. In general, all the different members agree on the positive trend. Differences become more evident increasing the depth considered.

shown in Figure 3.15A, 3.15B, 3.15C, 3.15D, (we reported only the mean across the ensemble for brevity). A general warming trend characterizes almost the whole domain, with Nordic Seas and the Mediterranean as warming spots with different rates. The only exception is for the central part of the North Atlantic. For the upper layer (300m and 700m), the Mediterranean and Norwegian Sea have similar warming trends, higher than what happens in the Labrador Sea; for the deep-layer contributions (2000m and top to bottom), warming trends in the Labrador and the Norwegian Sea become comparable, and higher than that in the Mediterranean Sea. Time series of OHC trend components are shown in Figure 3.15E, 3.15F, 3.15G, 3.15H: as stated above, showing that for the upper layer (top 300m and 700m) the spread across ensemble members is far less pronounced than in the case of deep-layer contributions. This fact can be attributed to the lack of deep data to ingest in the models through assimilation of temperature profiles: parametrizations become more relevant in contributing to the spread across models when deep-layer contributions are considered (not shown). We calculated the trends for this restricted North Atlantic - Mediterranean domain, whose results are reported in Table 3.3. These

depth/model	CGLO	FOAM	GLOR	ORAS	ensmean
OHC300	0.039±0.006	0.030±0.006	0.035±0.007	0.032±0.004	0.034±0.005
OHC700	0.058±0.008	0.042±0.012	0.073±0.011	0.049±0.005	0.053±0.008
OHC2000	0.084±0.007	**0.029±0.026**	0.102±0.030	$0.082 pm 0.007$	0.071±0.014
OHCbtm	0.086±0.006	**0.030±0.028**	0.098±0.034	0.096±0.007	0.072±0.013

Table 3.3. Summary of trends and standard deviation expressed in W/m^2 for all the depths, errors estimated with a bootstrap procedure as described in the text. These results refer to the case of the restricted domain of Atlantic and Mediterranean Sea. Bold values indicate where the Mann-Kendall confirmed the hypothesis of no trend.

regional OHC trends account for about the 10-15% of the global ones, at least in the case of CGLO, GLOR, ORAS5, FOAM, except that in FOAM for the deep-layer contributions (2000m and top to bottom), this ratio reaches the 35-40% (Table 3.2 and 3.3). Higher differences between FOAM and other members could be associated with the different sea ice model, the shorter assimilation window, the lack of forcing in Sea Ice Concentration in FOAM.

3.4 Concluding remarks

EOF analyses have shown significant correlations between SST, OHC and AMOC leading modes, presenting marked decadal to multidecadal variability and trends, besides the wind stress pattern being more rapidly varying and connected with shorter timescales (less than a month) variations. One notable feature of all variables, especially the AMOC transport in all ensemble members of ORAS5, is a regime change before and after 1995. The first regime, taking place before 1995, is of more intense circulation while the other one, with diminished AMOC strength, taking place after 2000, presents significant links with DWF in the Labrador Sea, GS path variations. At the same time, the subpolar/subtropical gyre exchange, as well as salt anomalies and kinetic energy east-west redistribution, are associated with this regime shift. Clearly, these factors, associated with AMOC changes, are not mutually independent and can also have mutual feedbacks. For example, future investigations should be devoted to understanding the role of regional seas, such as the Mediterranean Sea (Calmanti et al. (2006)). Mass, heat and salt transport through Gibraltar strait has non trivial consequences on Gulf Stream dynamics (De Coetlogon et al. (2006)), and more in general on North Atlantic regional climate (Keeley et al. (2012), Lozier and Stewart (2008), Polo et al. (2014)). Nonetheless, understanding better the local and remote effect of wind forcing on shorter timescales would require temporal resolution out of reach if we consider the currently released reanalysis products (Yang (2015)).
Our interpretation for the AMOC shift in ORAS5 can be summarized by the following chain of processes: heat flux reduction due partially to persistent pre-1995 positive NAO (Luo et al. (2010), Lohmann et al. (2009), Yang (2015), Pohlmann et al. (2013)) phase and also to flux-adjustment carried out to reduce biases in strong SST gradients regions (as also partly touched by Tietsche et al. (2020)) triggers changes in temperature and salt, hence density, of the Labrador sea. These density variations affect western Subpolar Gyre (SPG) variability, which causes the tilt of the Gulf Stream (GS) path and, at the same time, inhibit salt intrusions toward the eastern part of the North Atlantic. In this way, Nordic Seas stay active in terms of Deep Water Formation thanks to this salt recirculation, preventing the AMOC from a complete shutdown. The ocean circulation changes regime in response to atmospheric NAO variations, this in a maybe too fast but consistent way. Despite the impossibility to discard or confirm this interpretation with observations, actual further quantification of the typical timescales on which these phenomena take place, or if they have a multidecadal periodicity, would require longer simulation and coupled runs (see Biastoch et al. (2008) for model experiments changing either the wind, or heat/freshwater forcings). Our opinion regarding the ORAS5 regime change is that pre-mid1990s positive NAO phase drive an enhancement of the STG, favoring intrusion of salt anomalies toward northern latitudes and feeding a strong DWF in Labrador and Nordic Seas; with the following negative or almost neutral NAO phase, the AMOC weakens, due to the fact that SPG gets stronger, inhibiting the salt propagation and reducing DWF. These processes maybe overamplified by the flux-adjustment in ORAS5. The reason for this is that ORAS4, ORAS5 and SODA show a general positive difference between the climatology of the stream function in the two periods considered, but do not agree on its exact magnitude.

In this view, we think our work's novelty resides in complementing the analysis done by Tietsche et al. (2020), through the further investigation of the connection between AMOC regime shift, GS variability and DWF in high latitude seas, and proposing a mechanism for AMOC variability which finds out the regime change to be the oceanic response to NAO-induced forcing, which in turn drive in a cascade process SPG-STG variations, GS path modification, DWF in the Western (Labrador Sea) and the Eastern (GIN Sea) northern North Atlantic. The effects of this regime change in circulation of the North Atlantic can be seen also in salt and kinetic energy redistribution across the basin.
Despite we are still lacking a confirmation or disregard about this stability regime change, OHC analysis at the global scale is in agreement with previous intercomparison studies in the latest period (from 1993 onward), and our regional analysis in the connected North Atlantic - Mediterranean domain showed that this region accounts for about the 10-15% of global warming trends.
Still today, there is an active debate on the sensitivity to surface buoyancy forcings, like freshwater or heat fluxes, nonetheless on the role of the boundary current on DWF: these are investigated with the help of GCM model experiments (Rahmstorf (1996), Swingedouw et al. (2006), Spence et al. (2008), Marzocchi et al. (2015)). These pieces of evidence should also serve as food for thought, especially when dealing with data that have undergone a flux-adjustment procedure, as in the case of the present manuscript.
The interpretation of North Atlantic variability as driven primarily by surface buoyancy forcings has been called into question, acknowledging the importance, on shorter timescales, of the stochastic contribution given by the atmospheric forcing (Hasselmann (1976), Monahan et al. (2008)). In the present analyses, the role of wind stress variations seems not to have a sensible impact on longer-timescales dynamics. Whether or not short term variations can affect longer timescales is still a matter of debate and deserve suitable model experiments.
Quantifying aspects such as those stated above for understanding climate stability is challenging, both because of the scarcity of measurement (systems like basin-wide sections are pretty recent - Hirschi et al. (2003)) and also fundamental unresolved questions. An invaluable tool in the development of these research topics is given by ocean reanalyses, whose improvement process has to go hand in hand both with fundamental research on data assimilation (Storto et al. (2019)) and evaluation/validation/quality control of different products with respect to satellite data (Yang et al. (2021)). However, further studies with new data and new data analysis methodologies are needed to correctly capture the existing connection between the North Atlantic, the Mediterranean and their mutual role in the global climate system. Despite the importance of North Atlantic for being one of the hotspots of surface buoyancy loss, further studies on the other pole, i.e., Southern Hemisphere, as the other principal region for buoyancy gain of surface waters (Cessi (2019)), should be considered to investigate AMOC changes.

4

Small Scale Processes - Wave Vortex interactions

"Masagatsu
Agatsu
Katsu
Ayabe",
i.e.
"The greatest victory
is the one over yourself"

Mohrihei Ueshiba,
The Founder of Aikido

As discussed in the introduction, resolution of global general circulation models (GCM) is still limited to about 25 km for the ocean component at a global scale, which implies the heavy use of parameterizations of sub-grid physics. Thus, the effect of the small scales on large scale dynamical features of the ocean is still a matter of open fundamental research. Our aim in this chapter is to study the effect of smaller scales in a numerical setup which is able to focus directly those scale of motions which have to be parameterized in an ocean GCM. With this leitmotiv in mind, this chapter will be focused on trying to disentangle the mutual role of waves and vortexes in the energy transfer across scales in a simplified framework, i.e. a stratified turbulent flow in a rotating, non-unitary aspect ratio, tri-periodical domain. After a first introduction on the motivations, we will recall some basics on the theory of turbulence; then, after reviewing some previous literature results, we will summarize a state of the art decomposition used to disentangle waves from vortices in outputs from direct numerical simulation. The novelty of our approach is to use this decomposition to force wither vortices or waves within our simulations from the beginning.

4.1 Ocean Turbulence

Turbulence is one of the most fascinating and complex problem of classical physics. The energetic, irregular, chaotic, rotational and eddying state of a fluid is

often generically classified as a turbulent flow, and it is a nearly ubiquitous feature of oceanic motions, immediately below the sea surface as well as at greater depths. Turbulent motions are characterized by irregular and chaotic fluctuations of its state variables (e.g. velocities, temperature, pressure, density - which define the dynamics and thermodynamics of the flow) around their mean value.
Due to these highly fluctuating and irregular nature, when a fluid is in a turbulent state it has far greater ability to transfer momentum, heat or other tracers than in a laminar state, whereas transfers take place only via molecular diffusion alone (if we consider directions perpendicular to the mean flow), being the flow composed of ordered fluid sheets sliding one above each other. Due to the presence of nonlinear terms in the equations of motions, its dynamics involves a wide range of spatial and temporal scales.
Moreover, when turbulence is well developed (i.e. the flow has become independent from the forcing which generated it, restoring symmetries of the governing equations in a statistical sense, Frisch (1995)), chaotic behavior can take place in the system's evolution: even if the governing equations are deterministic (i.e. knowing with infinite precision the initial condition one could *exactly* reproduce the same dynamic evolution), close but not equal initial conditions will generate trajectories in phase space which soon diverge one from each other. Strong coupling across scales when nonlinear terms are non-negligible, and chaotic dynamics make the coupling between climate and turbulence even harder to achieve: significant predictions require not only large computing powers, but also large ensembles (i.e. many simulations starting from close initial conditions) in order to extract statistically valid results.
Fortunately, when dealing with small scales and turbulence, the latter problem can be partly overcame by running one simulation for a long enough time, such that the system can be considered statistically steady, assuming ergodicity.

4.2 Motivation

Scaling laws for energy spectra in the wave-number domain are a precious tool in understanding the partition of energy across different spatial scales, but oceanic motions take place also on a wide range of timescales. Ferrari and Wunsch (2009) provided an estimate of the energy spectrum derived from instruments on different mooring sites (we show one example in fig. 4.1), which show common features both at different locations and depths:

- all estimates show a low-frequency flat band at frequencies corresponding to periods longer than 1000 hours (about 40 days);
- between a frequency range $[100, 1000]$ hours (corresponding to about $[4, 40]$ days) the spectrum falls into a power law regime, with different scaling exponents depending on the location and the considered depth - this band has been identified as the geostrophic eddy range;
- energy accumulates on tidal frequencies, showing significant peaks mostly at all depths and locations;

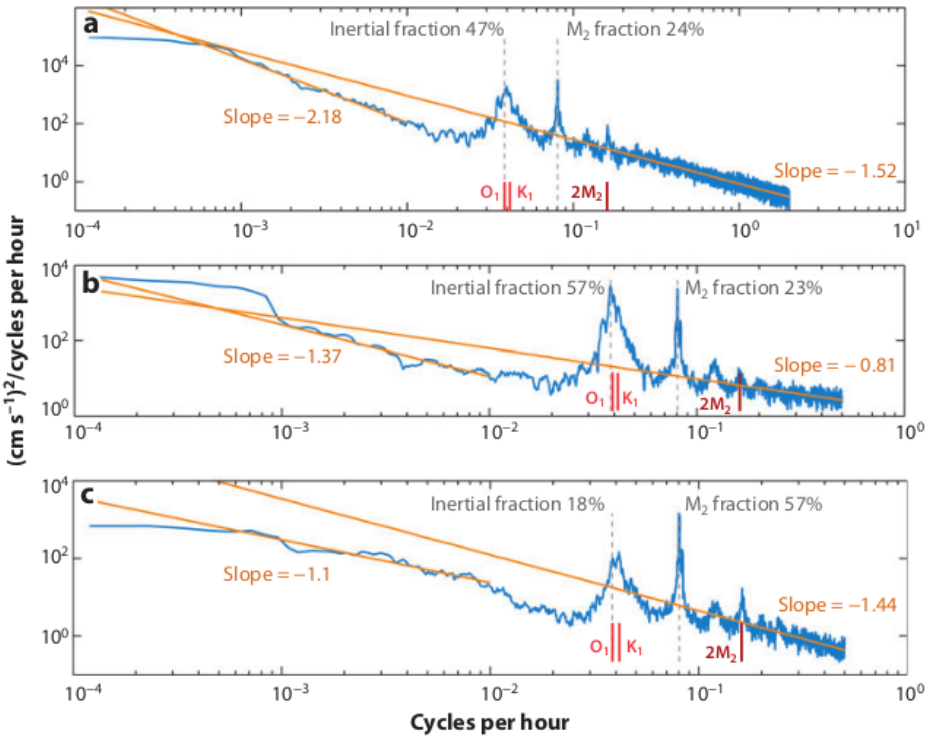

Figure 4.1. Figure 1 of Ferrari and Wunsch (2009): kinetic energy spectral estimates in the frequency domain from instruments on a mooring over the Mid-Atlantic Ridge near 27°N, at different depths: (a) 128m, (b) 1500m and (c) 3900m (near the bottom). Orange lines provide least square fit of power laws for periods between 10 and 2 hours, and 100 to 1000 hours. Inertial, principal semidiurnal M_2 and diurnal O_1, K_1 tidal peaks are marked by dashed vertical grey lines, together with their label where necessary. The first overtone $2M_2$ of the semidiurnal tide is also shown. Note the differing axis scales.

- for frequencies greater than the inertial Coriolis parameter $\sigma > f$, there is another power law with a different scaling exponent, identified as internal wave band - these high-frequency motions are not in geostrophic balance.

These results are very important, since they provide a proof of deviations from the Garrett and Munk empirical derivation for the spectrum of inertial-gravity waves. The large work by Polzin and Lvov (2011) re-opened the discussion on this empirical model, which is about 45 years old, and still widely used, though lacking of a first-principle derivation. One of the last modifications of this empirical model (GM76) assumes that it is possible to write the wavenumber-frequency spectral energy density in an open-ocean site as a separable function of the frequency and the vertical wavenumber alone:

$$E(\mathbf{k},\sigma) = E(k_z,\sigma) = \mathcal{E} A\left(\frac{k_z}{k_z^*}\right) B\left(\sigma\right), \tag{4.1}$$

with $\mathcal{E}$ is the total energy and A, B are expressed via the following functional form:

$$A\left(\frac{k_z}{k_z^*}\right) = \frac{2}{\pi}\frac{k_z^{*-1}}{\left[1+\left(\frac{k_z}{k_z^*}\right)^2\right]}, \qquad B\left(\sigma\right) = \frac{2f}{\pi}\frac{1}{\sigma\sqrt{\sigma^2-f^2}}, \tag{4.2}$$

i.e. the A and B scale respectively as k_z^{-2} and σ^{-2} for high wavenumber and frequency. Our general approach, behind this motivation to characterize energy pathways across scales when inertial-gravity waves are present in the system, will be thus to start from the UV side of the spectrum and simulate an open ocean situation directly focusing on small-scales in the system dynamics, i.e. without introducing any parameterization at all.
As already stated in the introduction, simultaneous presence of rotation and stratification effects significantly affects the flow dynamics (with the simultaneous presence of vortical and wave motions) depending on their relative strength, introducing additional scale of motions to deal with. In particular, strong rotation rates favor the development of nonlinear energy transfer toward the large scales, while internal waves, generated as large-scale features propagate into the ocean, transferring via nonlinear wave-wave interactions the surface forcing energy input to smaller scales, at which they brake and dissipate (Ferrari and Wunsch (2009)): their representation in OGCMs still is at an early stage, being these motions either parameterized or totally missing. In particular, up to the current understanding, shreds of evidences that the role of waves motions are subdominant at all scales are present, the interplay between vortices and waves far from being completely understood. That's why we are dealing with two main questions:

- It is possible to force only wave or vortical motions directly from the beginning?
- If the answer to this first question is yes, what are the respective roles of nonlinear turbulent motions (vortices) and rotation/stratification effects (waves)?

With these questions in mind, we will proceed, in the following sections, to review some known results from the literature, and to define our forcing, through the use of a decomposition which so far has been used only to analyze and interpret simulations results, up to our knowledge.

4.3 Kolmogorov 1941 theory of turbulence in a nutshell

The transition to turbulence, when rotation and stratification effects are not taken into account, is governed by the value of a single non-dimensional parameter called Reynolds number Re. Indeed in this case eqs.(1.3) can be reduced to the following non-dimensional form

$$\frac{\partial \hat{\boldsymbol{u}}}{\partial \hat{t}} + \hat{\boldsymbol{u}} \cdot \hat{\boldsymbol{\nabla}} \hat{\boldsymbol{u}} = -\hat{\boldsymbol{\nabla}} \hat{p} + \frac{1}{Re} \hat{\nabla}^2 \hat{\boldsymbol{u}} + \hat{\boldsymbol{F}}, \tag{4.3a}$$

$$\hat{\boldsymbol{\nabla}} \cdot \hat{\mathbf{u}} = 0. \tag{4.3b}$$

In eqs. (4.3), $\boldsymbol{u} = (u, v, w)$ is the velocity field, p is a re-scaled pressure (i.e. divided by the constant reference density ρ_0), $\mathbf{F}$ is the forcing term on velocity field, and the hat indicate non-dimensional variables. Reynolds number Re accounts for the relative importance of the nonlinear to viscous term in the governing equations, and has the following expression in terms of characteristic velocity U_{rms}, length scale of the flow L_0, and fluid viscosity ν, which have been used to write eqs. (4.3):

$$\mathrm{Re} := \frac{U_{rms}\, L_0}{\nu}. \tag{4.4}$$

The viscous term, involving the Laplace operator, has a stabilizing effect on the flow, while the nonlinear one represents advection of velocity gradients. When the Reynolds number is large enough, the flow can be considered as turbulent, because nonlinear terms begin to dominate on larger and larger range of scales. Kolmogorov 1941 theory of turbulence (K41 hereafter) find its roots in the well celebrated Richardson's cascade picture (Frisch (1995)):

"Big whirls have little whirls that feed on their velocity,
And little whirls have lesser whirls and so on to viscosity
– in the molecular sense."

This picture is formalized identifying important scales of motion, which are respectively

- the largest available scale $L_0 \sim k_0^{-1}$, comparable to the domain size;
- the forcing scale $L_f \sim k_f^{-1}$, i.e. the typical length scales on which energy is injected in the system ($L_f \leq L_0$ - an L_f close to L_0 will preferably excite large scale motions);
- the smallest turbulent scale, called the Kolmogorov scale $\eta \sim k_\eta^{-1}$, which is the scale at which the effect of dissipation sets in, removing energy from the system.

Introducing these scales allows to define what it is usually called the "inertial range of scales" $\eta \ll \ell \ll L_f$, which is a range where forcing and dissipation terms are less important, with nonlinear terms dominating the dynamics. Moreover, within this range, an energy cascade is defined by the presence of a constant rate of energy transfer across scales, e.g. a flux whose order of magnitude is

$$\Pi(\ell) \sim \frac{E(\ell)}{\tau_\ell} \sim u_\ell^2 \frac{u_\ell}{\ell} = \epsilon, \tag{4.5}$$

which sustains the steady flow ($E(\ell)$, τ_ℓ being respectively the energy at scale ℓ, and the time for a structure whose typical velocity is u_ℓ to travel over a distance ℓ, ϵ is a finite positive constant).
This flux balance the rate at which energy is injected by the forcing

$$\epsilon_{in} = \langle \mathbf{u} \cdot \mathbf{F} \rangle . \tag{4.6}$$

and the rate at which energy is dissipated by the laplacian term

$$\epsilon_{out} = -\nu \left\langle \left(\frac{\partial u_j}{\partial x_i} \right)^2 \right\rangle , \tag{4.7}$$

where $\langle \cdot \rangle$ denotes spatial average over the entire volume. Writing down the equation for energy (which in this case is only kinetic) $E = \frac{1}{2}\langle \boldsymbol{u} \cdot \boldsymbol{u} \rangle$, we can see that in a steady-state, conservation of energy implies a balance between these two terms (Frisch (1995), chapter 6):

$$\partial_t E = \epsilon_{in} - \epsilon_{out}. \tag{4.8}$$

In the $Re \to \infty$ limit, viscosity is so small to be negligible, the flow being completely nonlinear. At the same time, the flow develops very intense spatial velocity gradients, in such a way that energy dissipation stays finite in this limit:

$$\lim_{\nu \to 0} \epsilon_{out} = \epsilon, \tag{4.9}$$

this phenomenon is called dissipative anomaly.

4.3.1 3D Energy spectrum and cascades

In his seminal 1941 papers (Kolmogorov (1941a), Kolmogorov (1941b), Kolmogorov (1941c)), Kolmogorov gave its definition of homogeneous and isotropic turbulence (independence from space-time translations and spatial rotations around a given axis), which is based on the probability distribution function for velocity increments, rather than on velocities themselves. This led him to establish the main predictions of K41 theory, formulated as similarity hypotheses, which imply scaling laws for the kinetic energy spectrum and structure functions.
The *first similarity hypothesis* is that for locally homogeneous and isotropic turbulence the distribution moments are entirely determined by the energy dissipation rate and viscosity, leading to a relation between these quantities and the Kolmogorov scale

$$\eta \sim \left(\frac{\nu^3}{\epsilon} \right)^{1/4} . \tag{4.10}$$

The *second similarity hypothesis* states that, within the inertial range $\eta \ll \ell \ll L_f$, the moments do not depend on ν. This leads to the so-called 2/3 law for second order structure function of velocity increments (Frisch (1995)):

$$S_2(\ell) \equiv \langle (\delta \boldsymbol{u}(\ell))^2 \rangle \sim (\epsilon \ell)^{2/3} , \quad \delta \boldsymbol{u}(\ell) \equiv \boldsymbol{u}(\boldsymbol{x} + \boldsymbol{\ell}) - \boldsymbol{u}(\boldsymbol{x}) , \quad \ell = |\boldsymbol{\ell}| , \tag{4.11}$$

and to the exact result of 4/5 law for the third order structure function of longitudinal velocity increments $\delta_\ell u = [\boldsymbol{u}(\boldsymbol{x} + \boldsymbol{\ell}) - \boldsymbol{u}(\boldsymbol{x})] \cdot \boldsymbol{\ell}$:

$$S_3(\ell) \equiv \langle (\delta_\ell u)^3 \rangle = -\frac{4}{5} \epsilon \ell. \tag{4.12}$$

Defining an isotropic energy spectrum $E(k)$ as

$$E(k) = \frac{1}{2} \int_{|\mathbf{k}|=k} |\mathbf{u}(\hat{\mathbf{k}})|^2 \, d\mathbf{k} \tag{4.13}$$

where $\mathbf{k} = k_0\mathbf{n}$, $\mathbf{n} \in \mathbb{Z}^3$, and $k_0 = \frac{2\pi}{L_0}$ being the smallest available wave-number, the 4/5 law allows to fix the scaling exponent of velocity increments, leading to the Kolmogorov energy spectrum, which scales as

$$E(k) = 2\pi k \langle |\hat{\boldsymbol{u}}(\boldsymbol{k})|^2 \rangle = C\epsilon^{2/3} k^{-5/3}, \qquad C = \text{const} \sim \mathcal{O}(1) \,. \tag{4.14}$$

A *direct cascade* of energy from the forcing injection to smaller scales and dissipation

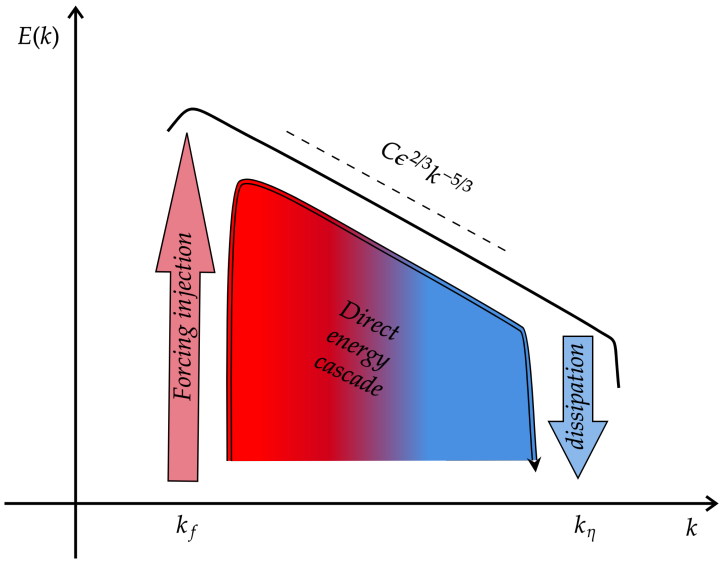

Figure 4.2. Schematic direct cascading spectrum of forced three-dimensional turbulence.

(schematically depicted in fig. 4.2) is a distinguishing character of 3D turbulence: the energy injected on a certain scale by the forcing is transferred toward smaller and smaller scales, till viscous dissipation acts to remove the energy, in such a way that a steady flow is maintained.

4.3.2 2D Energy spectrum and cascade

Given the low aspect ratio (i.e. the ratio of vertical to horizontal typical scales) of large and intermediate scale oceanic and atmospheric motions, it is worthwhile here to recall and wrap up some essential features of two-dimensional turbulence which are of geophysical interest. The classical theory of 2D turbulence stems from the seminal works of Kraichnan (1967), Batchelor (1969), Kraichnan and Montgomery (1980), which showed that its distinguishing character with respect to three dimensional turbulence arise from vorticity conservation along streamlines. Indeed, this is one of the cases where a reduction in the system's dimensions leads to the emergence of completely new phenomena. The governing equations in this case are

$$\frac{\partial \boldsymbol{v}}{\partial t} + \boldsymbol{v} \cdot \boldsymbol{\nabla}_h \boldsymbol{v} = -\frac{1}{\rho} \boldsymbol{\nabla}_h p + \nu \nabla_h^2 \boldsymbol{v} - \alpha \boldsymbol{v} + \boldsymbol{f}_{\boldsymbol{v}} \tag{4.15}$$

where $\boldsymbol{v} = (u, v)$ is the two dimensional velocity field of the flow, $\boldsymbol{\nabla}_h = (\partial_x, \partial_y)$, $\nabla^2 = \left(\partial^2_{xx} + \partial^2_{yy}\right)$ are gradient and laplacian operator in two dimensions, p is the pressure field, α is a large scale frictional damping coefficient which removes energy at large scales $L_\alpha \sim k_\alpha^{-1}$ (inserted to account for the fact that the flow is embedded in a 3D world), $\boldsymbol{f_v}$ is the forcing on velocity and all quantities depend only on x, y and t.
If we take constant density $\rho = 1$, the 2D version of the incompressibility condition $\boldsymbol{\nabla}_h \cdot \boldsymbol{v} = 0$ is automatically satisfied by introducing a scalar function $\psi(x, y, t)$ such that $\boldsymbol{v} = (\partial_y \psi, -\partial_x \psi)$ (the streamfunction).
Cross differentiating and subtracting eqs. 4.15 we can rewrite the governing equations in terms of the flow's vorticity (which is a scalar, in the sense of having only one nonzero component, perpendicular to the flow plane) $\omega_z = \partial_x v - \partial_y u = -\nabla^2_h \psi$:

$$\frac{\partial \omega_z}{\partial t} + \mathcal{J}\left(\omega_z, \psi\right) = \nu \nabla^2_h \omega_z - \alpha \omega_z + f_\omega, \tag{4.16}$$

in which the jacobian $\mathcal{J}\left(\omega_z, \psi\right) = \partial_x \omega_z \partial_y \psi - \partial_y \omega_z \partial_x \psi = \boldsymbol{v} \cdot \boldsymbol{\nabla}_h \omega_z$ and $f_\omega = \partial_x f_v - \partial_y f_u$ is the only nonzero component of the forcing vector curl. Moreover, the vortex stretching term vanishes, since its two dimensional analogue $\omega_z \boldsymbol{\nabla} \cdot \boldsymbol{v} = 0$ by the incompressibility condition. Eqs. (4.15), (4.16) are intended here to be supplied with periodic boundary conditions on a square domain.
In the inviscid, unforced and frictionless limit each fluid parcel conserves vorticity along its motion, and all integrals of the form $\int f(\omega_z) dxdy$ are inviscid invariants of the flow. Thus enstrophy $Z = 1/2 \langle \omega_z^2 \rangle = \frac{1}{2} \sum_{\boldsymbol{k}} \left|\hat{\omega}_z\left(\boldsymbol{k}\right)\right|^2$ and energy $E = 1/2 \langle \boldsymbol{v}^2 \rangle = 1/2 \langle \psi \omega_z \rangle = \frac{1}{2} \sum_{\boldsymbol{k}} \frac{\left|\hat{\omega}_z(\boldsymbol{k})\right|^2}{k^2}$ are quadratic conserved quantities.
When $\nu \neq 0$, the energy and enstrophy balance read:

$$\frac{dE}{dt} = -2\nu Z \equiv \epsilon_\nu\left(t\right), \tag{4.17}$$

$$\frac{dZ}{dt} = -2\nu \int dxdy \left|\boldsymbol{\nabla}_h \omega_z\right|^2 \equiv \eta_\nu\left(t\right). \tag{4.18}$$

Eq. (4.18) imply that the enstrophy cannot arbitrary grow in time (being bounded from above), contrary to three dimensional turbulence, where the vortex stretching term presence can arbitrary amplify Z, allowing for the existence of the dissipative anomaly. Thus in the two dimensional case we have:

$$\lim_{\nu \to 0} \epsilon_\nu\left(t\right) = \lim_{\nu \to 0} \frac{dE}{dt} = \lim_{\nu \to 0} -2\nu Z = 0, \tag{4.19}$$

which imply that energy is not dissipated by viscosity in fully developed 2D turbulence. Without a dissipation mechanism at small scales, the phenomenon of *inverse cascade* takes place, i.e. energy is transferred preferably to scales larger than the forcing. At the same time, being the vorticity gradients unbounded, one expects to find a *direct cascade* of enstrophy toward smaller scales (Boffetta and Ecke (2012)). In other words, we have now two inertial ranges $L_f \ll \ell \ll L_\alpha$, and $\eta \ll \ell \ll L_f$ in which scaling laws for energy spectra can be expected (schematically depicted in fig. 4.3). In terms of rates, the energy (enstrophy) friction rates ϵ_α (η_α) must balance the energy (enstrophy) injection and dissipation rates $\epsilon_I = \epsilon_{in} + \epsilon_\nu$ ($\eta_I = \eta_f + \eta_\nu$). Their ratio allows an estimate of the scales involved with the frictional damping

$L_\alpha^2 \equiv \epsilon_\alpha/\eta_\alpha$ and the dissipation $\eta^2 \equiv \epsilon_\nu/\eta_\nu$, and imposing the same type of relation at the forcing scale $L_f^2 \sim \epsilon_I/\eta_I$, the following relations can be established:

$$\frac{\epsilon_\nu}{\epsilon_\alpha} = \frac{\eta^2}{L_f^2}\frac{L_f^2}{L_\alpha^2}\frac{L_\alpha^2 - L_f^2}{L_f^2 - \eta^2}, \tag{4.20}$$

$$\frac{\eta_\nu}{\eta_\alpha} = \frac{L_\alpha^2 - L_f^2}{L_f^2 - \eta^2}, \tag{4.21}$$

which allow to determine the direction of cascades within their respective ranges. In the limit of extended direct inertial range $\eta \ll L_f$, one finds $\epsilon_\nu/\epsilon_\alpha \to 0$, which imply energy flowing to the large scales in an inverse cascade process. If in addition $L_\alpha \gg L_f$, one finds $\eta_\alpha/\eta_\nu \to 0$, i.e. enstrophy flows in a direct cascade process to scales smaller than the forcing. Writing in Fourier space the equation for kinetic energy changes

$$\partial_t E(k) = T(k) + F(k) - \nu k^2 E(k) - \alpha E(k), \tag{4.22}$$

where the term $T(k)$ accounts for the energy transfer due to nonlinear interactions, $F(k)$ is the forcing injection, and the other two remaining terms are respectively dissipation of energy due to viscosity and large scale friction.
One can define the energy and enstrophy fluxes from the nonlinear transfer term $T(k)$:

$$\Pi_E(k) = \int_k^\infty T(k')\,dk', \tag{4.23}$$

$$\Pi_Z(k) = \int_k^\infty k'^2 T(k')\,dk', \tag{4.24}$$

$\Pi_E(0) = \Pi_Z(0) = 0$ by conservation laws (4.17), (4.18).
Then in the range $k \ll k_f$, if large scales (small wave-numbers) dominate the spectrum of energy, the flux will behave as $\Pi_E(k) \sim \lambda_k k E(k)$, where the characteristic distortion frequency induced by eddies grows with their size $1/k$ as $\lambda_k \sim k^{\frac{2-\beta+1}{2}}$, and we are searching for a spectrum scaling $E(k) \sim k^{-\beta}$. Then by dimensional arguments it appears that, requiring to have a constant flux of energy toward large scales (or a power law for the k dependence of the spectrum), the only possibility is that $E(k)$ behaves as the Kolmogorov solution, i.e. fixing the exponent $\beta = 5/3$ (Boffetta and Ecke (2012)):

$$E(k) = C\epsilon_\alpha^{2/3} k^{-5/3} \qquad k_\alpha \ll k \ll k_f. \tag{4.25}$$

Meanwhile, requiring to have a constant enstrophy flux toward the small scale (estimated to be $\Pi_Z \sim \lambda_k k^3 E(k)$) we find $E(k)$ with a scaling exponent $\beta = 3$:

$$E(k) = C'\eta_\nu^{2/3} k^{-3}, \qquad k_f \ll k \ll k_\eta. \tag{4.26}$$

These scaling laws help to understand how the frictional and dissipative scale depend on their respective parameters, and thus in terms of flow features ($L_\alpha \simeq \epsilon_\alpha^{1/2}\alpha^{-3/2} \simeq U_{rms}/\alpha$ and $\eta \simeq \nu^{1/2}\eta_\nu^{-1/6}$).

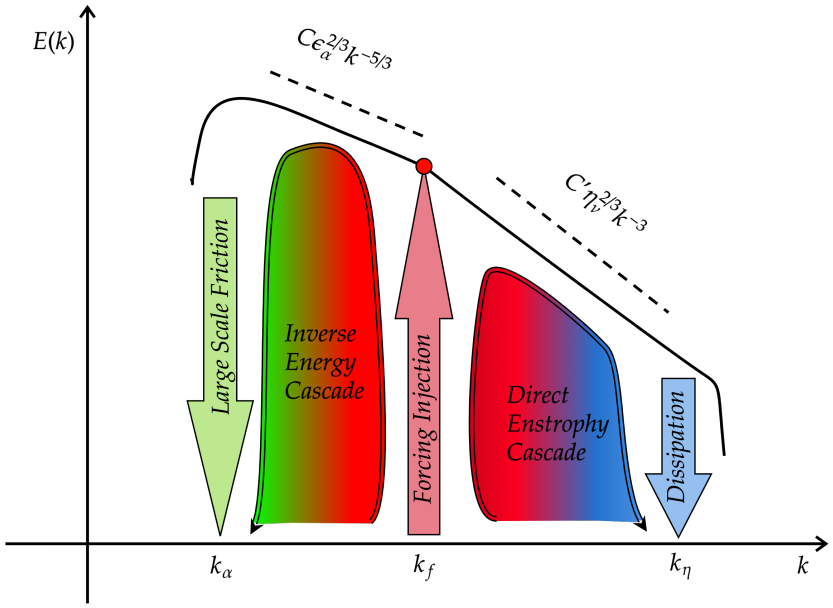

Figure 4.3. Schematic double cascading spectrum of forced two-dimensional turbulence.

4.3.3 Governing Equations

Since in the real world infinite computational powers are not already available to the scientific community, one common approach would be to rely on the approximations for which eqs. (1.3) hold, put in action a suitable parameterization of the unresolved scales in the motion, and proceed to simulate the ocean dynamics with an ocean model like NEMO, as briefly discussed in the introduction.
An other valid approach (which is the one we have in our mind here), is to avoid some of the approximations and run Direct Numerical Simulations (DNS) in a simplified domain (representing the open ocean far away from topographic boundaries), which allow to directly focus on those scales which are not resolved in a global GCM, studying their effect on intermediate to larger scales. The framework we refer to are incompressible Navier-Stokes equations in a rotating environment under the Boussinesq approximation, which can be written as:

$$\frac{\partial \boldsymbol{u}}{\partial t} + \boldsymbol{u}\cdot\boldsymbol{\nabla}\boldsymbol{u} + 2\boldsymbol{\Omega_0}\times\boldsymbol{u} = -\boldsymbol{\nabla}P + \nu\nabla^2\boldsymbol{u} - N\phi\,\boldsymbol{e}_3 + \boldsymbol{F}, \tag{4.27a}$$

$$\frac{\partial \phi}{\partial t} + \boldsymbol{u}\cdot\boldsymbol{\nabla}\phi = \kappa\nabla^2\phi + N\boldsymbol{e}_3\cdot\boldsymbol{u} + F_\phi, \tag{4.27b}$$

$$\nabla\cdot\mathbf{u} = 0. \tag{4.27c}$$

In these equations both the gravitational field $\mathbf{g} = -g\,\boldsymbol{e_3}$ and the rotation rate vector $\boldsymbol{\Omega_0} = \Omega_0\,\mathbf{e_3}$ are aligned to the z-axis. Here ϕ is a scalar field which has the dimension of a velocity, the parameter κ is the molecular diffusivity. Moreover, the gravity term is the only one in which density variations are retained, through the Brunt-Väisälä (BV) N frequency specified in detail below. Last but not least, F_ϕ,

the forcing on scalar field, which will be the object of a separate discussion in the following.
Let's specify a bit further the BV frequency N. Imagine to have a density profile within the fluid which is like

$$\rho_f = \rho_0 + \bar{\rho}(z) + \rho'(x, y, z, t) \tag{4.28}$$

with ρ_0 a reference value, $\bar{\rho}$ the time-independent linear background profile, and ρ' the density fluctuation. If we fix $\rho' = \gamma/N\phi$, then we have:

$$\rho_f = \rho_0 - \gamma\left(z - \frac{\phi(x, y, z, t)}{N}\right) \tag{4.29}$$

where $\gamma = -d\bar{\rho}(z)/dz$ is the mean density gradient. The BV frequency N is such that

$$N^2 = \left(-d\bar{\rho}(z)/dz\,\frac{g}{\rho_0}\right) = \frac{\gamma g}{\rho_0}, \tag{4.30}$$

and it has the dimensions of an inverse time. Indeed, displacing a fluid parcel from its original position in a stably stratified fluid, will trigger the action of buoyancy forces which pull it up or down (depending on the direction of original displacement), in the attempt to bring it back to it's original equilibrium position: a periodic motion takes place in response to the forces in play, and N is inversely proportional to the period of such oscillations.
In the inviscid unforced limit eqs. (4.27) conserve the total energy, i.e., the sum of the kinetic and potential contributions

$$E = \frac{1}{2}\langle|\mathbf{u}|^2\rangle + \frac{1}{2}\langle\phi^2\rangle\,, \tag{4.31}$$

where $\langle\cdot\rangle$ denotes spatial average over the entire volume.
In the limit of vanishing stratification $N \to 0$, the field ϕ decouples from the velocity field in (4.27), and the second of eqs. (4.27) becomes the equation for the evolution of a passive scalar field.
Writing the equations in non-dimensional form an additional dimensionless parameter, the Rossby number, characterize the flow

$$Ro := \frac{U_{rms}}{2\Omega_0 L_0}. \tag{4.32}$$

In particular, for $Ro \ll 1$ rotational terms dominate over nonlinear terms - large scale motions are commonly defined in oceanography as those significantly influenced by Earth's rotation (indeed motions in geostrophic equilibrium are those for which the rotational term balances exactly the pressure gradient term (Pedlosky (2013)), being possible to ignore all the remaining terms), the flow being composed of elongated vertical large scale vortical column structures.
When instead the rotation rate Ω is set to zero, the equations describe the purely stratified dynamics. The non-dimensional Froude number

$$Fr := \frac{U_{rms}}{N\,L_0} \tag{4.33}$$

distinguish the regime in which the stratification effects become dominant. Indeed, for $Fr \ll 1$ coupling with the scalar field is dominant, and the flow appears strongly stratified, i.e. composed by pancake-like vertically stacked fluid sheets of increasing density - the higher stratification, the stronger restoring forces acting on a fluid parcel displayed from its initial equilibrium position, resulting in vertical motions being strongly suppressed.
In the full case of eqns. (4.27), the Prandtl number appears beside Rossby, Froude and Reynolds numbers, defined as:

$$\mathrm{Pr} := \frac{\nu}{\kappa}. \tag{4.34}$$

For $Pr \ll 1$ the diffusive term acquire importance in the flow dynamics - we will set it to $\mathcal{O}(1)$ for the sake of simplicity, even if there are some variations with respect to this order of magnitude in the ocean.
Rotation and stratification introduce additional scales, which are respectively the Zeman scale $\ell_\Omega \sim U_{rms}/2\Omega_0 \sim k_\Omega^{-1}$ and the Ozmidov scale $\ell_N \sim U_{rms}/N \sim k_N^{-1}$, marking regions in which one process dominates over the other. For $\ell > \ell_\Omega$ ($\ell < \ell_N$) rotation (stratification) effects are non-negligible in the flow dynamics, when the respective rotation (stratification) term is compared to the nonlinear one. Indeed (as we shall see below) in the inviscid, unforced, linearized limit, the system admits solutions in term of waves with a frequency in between the Coriolis parameter $f = 2\Omega_0$ and the BV frequency N.

4.4 State of the art

The work of Smith et al. (1996) constitutes one of the first attempts to systematically study the problem. In this paper, the transition from 2D to 3D turbulence in a small aspect ratio domain for a forced rotating flow is investigated.
An additional nondimensional parameter, the aspect ratio $\delta = L_z/L_x = k_x/k_z$, adds up to the other set of dimensionless parameters characterizing the system dynamics - Reynolds and Rossby numbers in this case, which can be estimated also in terms of the forcing typical scale and injection rates as

$$Re = \epsilon_{in}^{1/3} k_f^{-4/3}/\nu, \qquad Ro = \left(\epsilon_{in} k_f^2\right)^{1/3}/f. \tag{4.35}$$

It came out from their analysis that a discriminant parameter is the relative scale of the force with respect to the slab domain depth $S = L_f/L_z = k_z/k_f$. The forcing is in turn either a 2D2C (two-dimensional, two-component) forcing, or a (3D3C) one (more detailed information given in the paper). Since they investigate the high Re and low δ limit, the parametric study is done in the (S, Ro) space.
At zero rotation rate ($Ro = \infty$), they found that the transition from a 2D (inverse cascade) and a 3D (direct cascade) takes place when S exceed a critical value $S_c \approx 0.5$. When the rotation rate is increased, the critical value S_c gets higher. This result seems to be robust across the different resolution they used.
Let's focus one moment on the way they calculate spectra. The traditional definition of the isotropic kinetic energy spectrum in Statistically Homogeneous Isotropic Turbulence (SHIT) is based on eqn. (4.13), in which $E(k)dk$ represent the energy

density of a spherical peel of radius k and width dk.
From this perspective, it is possible to define a pure 2D contribution passing to cylindrical coordinates and selecting the slice $k_z = 0$, which is referred as $E(k_h, k_z = 0)$ in Smith et al. (1996), Smith and Waleffe (1999), Smith and Waleffe (2002), with $k_h = \sqrt{k_x^2 + k_y^2}$.
An other possibility is to look at the energy integrated over k_z, and binned into rings on the plane perpendicular to the axis which rotation is aligned to. Horizontal and vertical direction are thus usually referred to the rotation axis of the system, and we will adopt the same convention in what follows.
Their forcing (either the 2D2C or the 3D3C) is a gaussian random function localized at small wave numbers (order 1), i.e. injecting energy on large scales (meaning $k_f \approx k_0$).
In their following work, Smith and Waleffe (1999) studied forced rotating turbulence again, but this time adding also the unitary aspect ratio domain case. The forcing is random, and centered about an intermediate wavenumber k_f. Their result show that energy is transferred to scales larger than the forcing if the rotation rate is strong enough (i.e. low Rossby number). The scaling properties of the energy spectrum are discussed:

1. they find a power-law behavior for the isotropic three-dimensional energy spectrum $E(k) \sim k^{-3}$ for $k_\eta \ll k \ll k_f$ (almost all of this energy comes from large scale 2D motions - anticyclonic vortices);

2. the 2D energy spectrum on the plane $E(k_h, k_z = 0) \sim k_h^{-3}$ for $k_h < k_f$;

3. decreasing aspect ratio or resolution of the box they found an inverse energy cascade regime, with a $-5/3$ scaling exponent of the 2D spectrum, which is robust even when the vertically integrated contribution is considered.

They concluded that the transfer of energy from small to large scales is anisotropic: only vertically independent horizontal motions are populated at scales larger than the forcing, arranged in the form of cyclonic vortical columns which tends to fill all the available vertical extent of the domain.
In Smith and Waleffe (2002), stratification effects are taken into account, with a scalar field coupled to the flow via the Brunt-Vaisala frequency N. An additional non-dimensional parameter adds up to the other in determining the flow regime (Froude number - whose estimate in terms of forcing injection scales and rate is $Fr = \left(\epsilon_f k_f^2\right)^{1/3} / N$).
This time the energy injection comes from a three dimensional random forcing localized at small scales (i.e. large wave numbers). The range of Freude numbers investigated is below a critical $\mathcal{O}(1)$ value below which an inverse energy cascade is present. Within this range, energy is transferred to scales larger than the forcing. It is found that the slow large scale dynamics is strongly connected to the N/f ratio:

- For $N/f \gg 1$, slow large scales consist of Vertically Sheared Horizontal Flows (VSHF), i.e. motions with $k_h \approx 0$, zero vertical vorticity and velocity, no potential vorticity;

- For $1/2 \leq N/f \leq 2$ slow geostrophic (i.e. motions with zero frequency) modes dominate the large scales dynamics, and no triadic interactions can take place.

At the same time, there are indications that a higher rotation rate favours the flow's tendency to be two-dimensional (inverse energy cascade development), whilst a larger degree of stratification favours a downscale energy cascade, suppressing inverse transfers.
Oceanographers commonly define geostrophic motions as those for which a large scale balance between the pressure gradient term and the Coriolis term of the governing equations hold true. In formulas, this mean having a divergence free, purely horizontal velocity field in which

$$\begin{cases} u = -\dfrac{1}{f\rho_0}\dfrac{\partial p}{\partial_y} \\ \\ v = \dfrac{1}{f\rho_0}\dfrac{\partial p}{\partial x} \end{cases} \tag{4.36}$$

Indeed this definition of geostrophic modes is consistent with the interpretation given by people studying turbulence (which intend zero-frequency motions to be in geostrophic balance).
Herbert et al. (2016) studied the partition of energy between waves and vortices in stratified turbulence, within a cubic, tri-periodical domain. With a $Re \approx 1000$, they

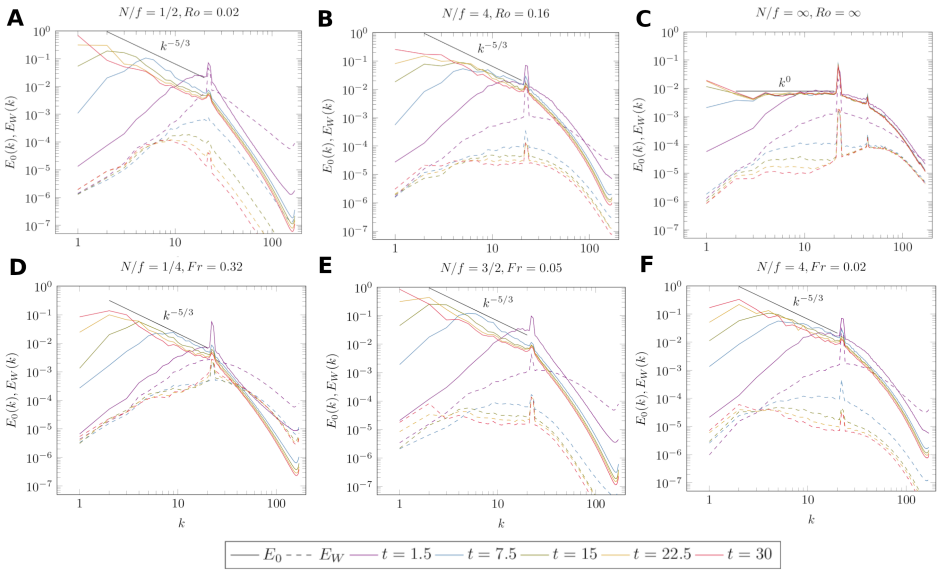

Figure 4.4. Figure from Herbert et al. (2016) (rearranged for our purposes). Vortical (solid lines) and wave (dashed lines) decomposition of the energy spectra, according to the decomposition in Bartello (1995). Fixed Fr=0.04 simulations in panels (**A**), (**B**), (**C**), rotation rate decreases from left to right. Panels (**D**), (**E**), (**F**) show fixed Ro = 0.08 runs, with stratification increasing from left to right. The inverse cascade decreases when stratification effects increase, till disappearing in the purely stratified runs. For $N/f \geq 2$ the fraction of energy in wave modes increases as well.

carried out simulations with $N/f \in [1/4, 20]$, together with purely stratified runs

(for which $N/f = \infty$), according two protocols: either they vary Rossby number at fixed Froude, or the converse. A main outcome of the paper is that they find slow, vortical modes dominating over fast, wave modes mostly at all scales and in all the range of parameters explored (see fig. 4.4). Robust signs of an inverse cascade, weakening when rotation is decreased and stratification is increased, disappearing in the purely stratified case, are present in the slow mode energy spectra.
Results are analyzed and interpreted via the use of a linear eigenmode decomposition originally used by Bartello (1995), which we will broadly discuss in the following section. It is possible to define potential vorticity as

$$\Pi = f\partial_z\phi - N\omega_z + \boldsymbol{\omega}\cdot\boldsymbol{\nabla}\phi \tag{4.37}$$

where $\omega_z = \partial_x v - \partial_y u$ is the vertical component of vorticity $\boldsymbol{\omega}$. This quantity is composed of a linear $\Pi_1 = f\partial_z\phi - N\omega_z$ and a nonlinear term $\Pi_2 = \boldsymbol{\omega}\cdot\boldsymbol{\nabla}\phi$. Because of these terms, the enstrophy is quartic in the dynamic variables, and not necessarily conserved as in 2D flows. They show also that this quantity reaches a stationary behavior in time and it is well approximated by its quadratic part $\mathcal{E}_2 = \int \Pi_1^2$, linking it to the inverse cascade presence. The inverse cascade disappearance is attributed to three major effects:

1. Because forcing projections on slow and fast modes are approximately equal, when $N/f \gg 2$ the fraction of energy in the waves increases - wave modes do not contribute to $\mathcal{E}_2$, leading to a weakening of the inverse cascade;

2. The more the system gets to a purely stratified situation, the more the energy goes into VSHF modes, which do not carry potential vorticity;

3. In the range of parameters where the inverse cascade weakens, arguments leading to the approximation of enstrophy by its quadratic part can break up.

In particular, the first point of the above list motivates our intent to search if, using the same decomposition used for their analysis, it is possible to change forcing projections on slow/fast modes, in such a way to understand where does the energy goes when only vortices, or only waves are forced in the simulation from start. Furthermore, this decomposition can be useful even in the analysis of GCM data, where the research for non-traditional decomposition methods to isolate flow features still represents an open topic of active research (see Buzzicotti et al. (2021) to learn about the use of a promising coarse grain method in alternative to traditional Fourier analyis).

4.5 Forcing either Vortexes or Waves via Normal Modes Decomposition

Normal modes decomposition like the one in Bartello (1995) has proven to be a powerful method to disentangle the relative contributions of vortexes and waves in analyzing outputs from direct numerical simulation of an incompressible fluid under the Boussinesq approximation (see Herbert et al. (2014), Brunner-Suzuki et al. (2014), Herbert et al. (2016), Oks et al. (2017), Li et al. (2020) and references

therein for some applications). Interesting alternative methodologies, such as wavenumber/frequency energy spectra have been used to detect waves in di Leoni et al. (2014), di Leoni and Mininni (2015) for system under rotation or stratification alone. In these cases, the major footprint of waves is an accumulation of energy along the dispersion relation curve, clearly visible in the frequency-wavenumber space. This procedure has the advantage to give a more comprehensive picture, but it requires higher capacity storage and computational resources. Indeed, it is required to save snapshots of the velocity field at high frequency and for a long enough simulation. Our starting point are eqs. (4.27), which we will discuss here denoting by $u_i(\boldsymbol{x}, t)$, $i = 1, 2, 3$ the velocity components along the direction x_i at time t. Time dependence of stratification has been neglected, resulting in constant N. Notice that we adopted Einstein's convention: otherwise stated, summation over repeated indices is implied. Expanding our set dynamical fields in Fourier components, neglecting forcing, dissipative and diffusive terms we can consider the linearized dynamics (details of the calculation are reported in the appendix A.1):

$$\begin{aligned} \partial_t \hat{u}_i(\mathbf{k}) &= f P_{ij}(\mathbf{k}) \varepsilon_{jl3} \hat{u}_l(\mathbf{k}) - N P_{i3}(\mathbf{k}) \hat{\phi}(\mathbf{k}) \,, \\ \partial_t \hat{\phi}(\mathbf{k}) &= N \hat{u}_3(\mathbf{k}) \,, \\ k^i \hat{u}_i(\mathbf{k}) &= 0 \,, \end{aligned} \tag{4.38}$$

In eqn. (4.38), we have introduced the projection operator $P_{ij}(\mathbf{k}) = (\delta_{ij} - k_i k_j / k^2)$ which serves to get rid of the pressure term, while ε_{jlk} is the Levi-Civita anti symmetric tensor.
This linearized system of equations admit solutions in the form of travelling waves, $\hat{u}_j(\mathbf{k}, t) \propto e^{i\,\sigma(\mathbf{k},t)\,t}$ and $\hat{\phi}(\mathbf{k}, t) \propto e^{i\,\sigma(\mathbf{k},t)\,t}$, characterized by the following dispersion relation:

$$\sigma^2(\mathbf{k}) = \frac{N^2 k_\perp^2 + f^2 k_{||}^2}{k^2}, \tag{4.39}$$

where $k_\perp^2 = k_h^2 = k_1^2 + k_2^2$, and $k_{||}^2 = k_3^2$ (mathematical details of one possible derivation of such dispersion relation are given in appendix A.2).

4.5.1 Linear Eigenmodes decomposition

The linearised system can be recast in the following ODE form :

$$\dot{\mathbf{X}}(\mathbf{k}) = \mathbf{L}(\mathbf{k}) \mathbf{X}(\mathbf{k}), \tag{4.40}$$

where $\mathbf{X} = \left(\hat{u}^{(1)}(\mathbf{k}), \hat{u}^{(2)}(\mathbf{k}), \hat{u}^{(3)}(\mathbf{k}), \hat{\phi}(\mathbf{k})\right)^T$ and $\mathbf{L}(\mathbf{k})$ is a linear operator which has the form (assuming $k^2 \neq 0, k_h^2 = k_1^2 + k_2^2 \neq 0, k_{||}^2 = k_3^2 \neq 0$)

$$\mathbf{L_k} = \begin{pmatrix} f\frac{k_1 k_2}{k^2} & f\left(1 - \frac{k_1^2}{k^2}\right) & 0 & N\frac{k_1 k_3}{k^2} \\ -f\left(1 - \frac{k_2^2}{k^2}\right) & -f\frac{k_1 k_2}{k^2} & 0 & N\frac{k_2 k_3}{k^2} \\ f\frac{k_2 k_3}{k^2} & -f\frac{k_1 k_3}{k^2} & 0 & -N\left(1 - \frac{k_3^2}{k^2}\right) \\ 0 & 0 & N & 0 \end{pmatrix} \tag{4.41}$$

In the case $k_\perp \neq 0$, $k_{||} \neq 0$, it exist a matrix $\mathbf{M}(\mathbf{k}) = (\mathbf{Z}_-(\mathbf{k}), \mathbf{Z}_0(\mathbf{k}), \mathbf{Z}_+(\mathbf{k}))$ which diagonalizes the matrix $\mathbf{L}(k)$, whose columns are the eigenvectors of this system, and has the following expression:

$$\mathbf{M}(\mathbf{k}) = \frac{1}{\sqrt{2}\sigma(\mathbf{k})\, k\, k_\perp} \begin{pmatrix} fk_2k_{||} - ik_1k_{||}\sigma(\mathbf{k}) & -\sqrt{2}Nk_2k_\perp & fk_2k_{||} + ik_1k_{||}\sigma(\mathbf{k}) \\ -fk_1k_{||} - ik_2k_{||}\sigma(\mathbf{k}) & \sqrt{2}Nk_1k_\perp & -fk_1k_{||} + ik_2k_{||}\sigma(\mathbf{k}) \\ ik_\perp^2\sigma(\mathbf{k}) & 0 & -ik_\perp^2\sigma(\mathbf{k}) \\ -Nk_\perp^2 & -\sqrt{2}fk_{||}k_\perp & -Nk_\perp^2 \end{pmatrix}. \tag{4.42}$$

In the above matrix, $k = \sqrt{k_1^2 + k_2^2 + k_3^2}$.
The vectors $\mathbf{Z}_-(\mathbf{k})$,$\mathbf{Z}_0(\mathbf{k})$ and $\mathbf{Z}_+(\mathbf{k})$ are mutually orthogonal, and normalized to unity:

$$\mathbf{Z}_r(\mathbf{k})^\dagger \mathbf{Z}_s(\mathbf{k}) = \delta_{rs} \tag{4.43}$$

where † denotes the transpose and complex conjugation. Although the matrix $\mathbf{M}(\mathbf{k})$ is rectangular, it satisfies the hermitian identity $\mathbf{M}(\mathbf{k})^\dagger \mathbf{M}(\mathbf{k}) = I_{3\times 3}$. Vectors $\mathbf{Z}_r(\mathbf{k})$ are the normal modes of the linearized dynamics:

$$\mathbf{L}(\mathbf{k})\mathbf{Z}_0(\mathbf{k}) = 0, \tag{4.44}$$

$$\mathbf{L}(\mathbf{k})\mathbf{Z}_+(\mathbf{k}) = i\sigma(\mathbf{k})\mathbf{Z}_+(\mathbf{k}) \tag{4.45}$$

$$\mathbf{L}(\mathbf{k})\mathbf{Z}_-(\mathbf{k}) = -i\sigma(\mathbf{k})\mathbf{Z}_-(\mathbf{k}), \tag{4.46}$$

consisting of one slow, zero-frequency mode $\mathbf{Z}_0(\mathbf{k})$ left invariant by the linearized dynamics and referred to as the *vortical* mode, and two fast, non-zero-frequency modes $\mathbf{Z}_\pm(\mathbf{k})$ which oscillate with frequency $\pm\sigma(\mathbf{k})$ referred to as the *waves*.
Any vector can be thus expressed as:

$$\mathbf{X}(\mathbf{k}) = A_0(\mathbf{k})\mathbf{Z}_0(\mathbf{k}) + A_-(\mathbf{k})\mathbf{Z}_-(\mathbf{k}) + A_+(\mathbf{k})\mathbf{Z}_+(\mathbf{k}). \tag{4.47}$$

It is possible to introduce projecting operators as follows:

$$\mathbf{P}_0(\mathbf{k}) = \mathbf{Z}_0(\mathbf{k})\mathbf{Z}_0(\mathbf{k})^\dagger, \tag{4.48}$$

$$\mathbf{P}_W(\mathbf{k}) = \mathbf{Z}_+(\mathbf{k})\mathbf{Z}_+(\mathbf{k})^\dagger + \mathbf{Z}_-(\mathbf{k})\mathbf{Z}_-(\mathbf{k})^\dagger, \tag{4.49}$$

where full expression in this case is:

$$\mathbf{P}_0(\mathbf{k}) = \frac{1}{\sigma^2(\mathbf{k})\, k^2} \begin{pmatrix} N^2k_2^2 & -N^2k_1k_2 & 0 & Nfk_{||}k_2 \\ -N^2k_1k_2 & N^2k_1^2 & 0 & -Nfk_{||}k_1 \\ 0 & 0 & 0 & 0 \\ Nfk_{||}k_2 & -Nfk_{||}k_1 & 0 & f^2k_{||}^2 \end{pmatrix} \tag{4.50}$$

$$\mathbf{P}_W(\mathbf{k}) = \frac{1}{\sigma^2(\mathbf{k})\, k^2\, k_\perp^2} \begin{pmatrix} k_{||}^2\left(f^2k_2^2 + k_1^2\sigma_{\mathbf{k}}^2\right) & k_1k_2k_{||}^2\left(\sigma_{\mathbf{k}}^2 - f^2\right) & -k_1k_{||}k_\perp^2\sigma_{\mathbf{k}}^2 & -k_2k_{||}k_\perp^2Nf \\ k_1k_2k_{||}^2\left(\sigma_{\mathbf{k}}^2 - f^2\right) & k_{||}^2\left(f^2k_1^2 + k_2^2\sigma_{\mathbf{k}}^2\right) & -k_2k_{||}k_\perp^2\sigma_{\mathbf{k}}^2 & k_1k_{||}k_\perp^2Nf \\ -k_1k_{||}k_\perp^2\sigma_{\mathbf{k}}^2 & -k_2k_{||}k_\perp^2\sigma_{\mathbf{k}}^2 & k_\perp^4\sigma_{\mathbf{k}}^2 & 0 \\ -k_2k_{||}k_\perp^2Nf & k_1k_{||}k_\perp^2Nf & 0 & N^2k_\perp^4 \end{pmatrix} \tag{4.51}$$

By using these projectors, which are mutually orthogonal $\mathbf{P}_0(\mathbf{k}) \oplus \mathbf{P}_W(\mathbf{k}) = \mathbf{I}_{4\times 4}$, we can take any vector and project it onto the specific manifold, $\mathbf{X}_0(\mathbf{k}) = \mathbf{P}_0(\mathbf{k})\mathbf{X}(\mathbf{k})$, and $\mathbf{X}_W(\mathbf{k}) = \mathbf{P}_W(\mathbf{k})\mathbf{X}(\mathbf{k})$, to obtain its form acting on the slow manifold only, or onto the fast manifold of the wave modes only (see below for the forcing vector).

From the general case ($N \neq 0, f \neq 0$)), we use the expression of $\mathbf{L}_\mathbf{k}$ as the starting point for discussing limiting cases of purely stratified dynamics ($N \neq 0, f = 0$) and of purely rotating one ($N = 0, f \neq 0$).

Limiting case 1: purely stratified flow ($N \neq 0, f = 0$)

For the purely stratified flow, we have $\sigma^2(\mathbf{k}) = \frac{N^2 k_\perp^2}{k^2}$

$$\mathbf{L_k} = \begin{pmatrix} 0 & 0 & 0 & N\frac{k_1 k_3}{k^2} \\ 0 & 0 & 0 & N\frac{k_2 k_3}{k^2} \\ 0 & 0 & 0 & -N(1-k_3^2/k^2) \\ 0 & 0 & N & 0 \end{pmatrix} \tag{4.52}$$

and

$$\mathbf{M}(\mathbf{k}) = \frac{1}{\sqrt{2}\sigma(\mathbf{k})\, k\, k_\perp} \begin{pmatrix} -ik_1 k_{||}\sigma(\mathbf{k}) & -\sqrt{2}Nk_2 k_\perp & ik_1 k_{||}\sigma(\mathbf{k}) \\ -ik_2 k_{||}\sigma(\mathbf{k}) & \sqrt{2}Nk_1 k_\perp & ik_2 k_{||}\sigma(\mathbf{k}) \\ ik_\perp^2\sigma(\mathbf{k}) & 0 & -ik_\perp^2\sigma(\mathbf{k}) \\ -Nk_\perp^2 & 0 & -Nk_\perp^2 \end{pmatrix} \tag{4.53}$$

whose columns are still the eigenvector of the system, $(\mathbf{Z}_-(\mathbf{k}), \mathbf{Z}_0(\mathbf{k}), \mathbf{Z}_+(\mathbf{k}))$, the slow mode being in hydrostatic balance only if $k_\perp = 0$, and they are the only ones contributing to potential enstrophy (Herbert et al. (2014)).

If $k_3 = k_{||} = 0$, making use of the incompressibility condition $k_1\hat{u}_{\mathbf{k}}^{(1)} + k_2\hat{u}_{\mathbf{k}}^{(2)} = 0$, the matrix of eqn. (4.41) reduces to:

$$\mathbf{L_k} = \begin{pmatrix} 0 & 0 & 0 & 0 \\ 0 & 0 & 0 & 0 \\ 0 & 0 & 0 & -N \\ 0 & 0 & N & 0 \end{pmatrix} \tag{4.54}$$

Which correspond to the purely stratified dynamics on the $k_\perp$ plane.

Notice that it is possible to pass to this limit simply by putting $k_{||} = 0$ in the matrix $\mathbf{M}(\mathbf{k})$ of eqn. (4.42), to obtain the change of basis which decomposes the dynamics on the slow-fast manifold:

$$\mathbf{M}(\mathbf{k}) = \frac{1}{\sqrt{2}k_\perp} \begin{pmatrix} 0 & -\sqrt{2}k_2 & 0 \\ 0 & \sqrt{2}k_1 & 0 \\ ik_\perp & 0 & -ik_\perp \\ -k_\perp & 0 & -k_\perp \end{pmatrix}. \tag{4.55}$$

In this case projection operators are the same obtained by letting $k_{||} = 0$ in the expressions of eqn. (4.50), (4.51):

$$\mathbf{P}_0(k) = \frac{1}{k_\perp^2} \begin{pmatrix} k_2^2 & -k_1 k_2 & 0 & 0 \\ -k_1 k_2 & k_1^2 & 0 & 0 \\ 0 & 0 & 0 & 0 \\ 0 & 0 & 0 & 0 \end{pmatrix} \tag{4.56}$$

$$\mathbf{P}_W(\mathbf{k}) = \begin{pmatrix} 0 & 0 & 0 & 0 \\ 0 & 0 & 0 & 0 \\ 0 & 0 & 1 & 0 \\ 0 & 0 & 0 & 1 \end{pmatrix}. \tag{4.57}$$

Fast modes in this case are waves propagating with the gravity wave frequency $\pm\sigma(\mathbf{k}) = \pm N$ on the $k_\perp$ plane, while the vortical mode is given by the vertical component of the vorticity field, which is constant in time.

Limiting case 2: purely rotating flow ($N = 0, f \neq 0$)

In the purely rotating case, we have $\sigma^2(\mathbf{k}) = \frac{f^2\, k_{||}^2}{k^2}$,

$$\mathbf{L_k} = \begin{pmatrix} f\frac{k_1 k_2}{k^2} & f\left(1 - \frac{k_1^2}{k^2}\right) & 0 & 0 \\ -f\left(1 - \frac{k_2^2}{k^2}\right) & -f\frac{k_1 k_2}{k^2} & 0 & 0 \\ f\frac{k_2 k_3}{k^2} & -f\frac{k_1 k_3}{k^2} & 0 & 0 \\ 0 & 0 & 0 & 0 \end{pmatrix} \tag{4.58}$$

and for the M matrix we have:

$$\mathbf{M}\,(\mathbf{k}) = \frac{1}{\sqrt{2}\sigma(\mathbf{k})\, k\, k_\perp} \begin{pmatrix} fk_2k_{||} - ik_1k_{||}\sigma(\mathbf{k}) & 0 & fk_2k_{||} + ik_1k_{||}\sigma(\mathbf{k}) \\ -fk_1k_{||} - ik_2k_{||}\sigma(\mathbf{k}) & 0 & -fk_1k_{||} + ik_2k_{||}\sigma(\mathbf{k}) \\ ik_\perp^2\sigma(\mathbf{k}) & 0 & -ik_\perp^2\sigma(\mathbf{k}) \\ 0 & -\sqrt{2}fk_{||}k_\perp & 0 \end{pmatrix}. \tag{4.59}$$

If we restrict ourselves only on the velocity fields space, slow modes exist only where the dispersion relation becomes trivial, i.e. for $k_{||} = 0$. These two dimensional modes are the so-called "two-dimensional three-component" modes, and play a role analogous to the vortical modes of the full rotating-stratified turbulence (Herbert et al. (2014)).
Since the rotation acts on the parallel direction, we can look at the sub-manifold $k_\perp = 0$, where the dispersion relation becomes $\sigma^2(k) = f^2$, and the linearized dynamics operator of eqn. (4.41) becomes (incompressibility condition results in having null vertical velocities):

$$\mathbf{L_k} = \begin{pmatrix} 0 & f & 0 & 0 \\ -f & 0 & 0 & 0 \\ 0 & 0 & 0 & 0 \\ 0 & 0 & 0 & 0 \end{pmatrix} \tag{4.60}$$

and the matrix of eigenvectors which diagonalizes the dynamics is then

$$\mathbf{M}\,(\mathbf{k}) = \frac{1}{\sqrt{2}} \begin{pmatrix} i & 0 & -i \\ 1 & 0 & 1 \\ 0 & 0 & 0 \\ 0 & -\sqrt{2} & 0 \end{pmatrix} \tag{4.61}$$

In this case projection operators are the same obtained by letting $k_\perp = 0$ in the expressions of eqn. (4.50), (4.51):

$$\mathbf{P}_0(\mathbf{k}) = \begin{pmatrix} 0 & 0 & 0 & 0 \\ 0 & 0 & 0 & 0 \\ 0 & 0 & 0 & 0 \\ 0 & 0 & 0 & 1 \end{pmatrix} \tag{4.62}$$

$$\mathbf{P}_W(\mathbf{k}) = \begin{pmatrix} 1 & 0 & 0 & 0 \\ 0 & 1 & 0 & 0 \\ 0 & 0 & 0 & 0 \\ 0 & 0 & 0 & 0 \end{pmatrix}. \tag{4.63}$$

The linearized dynamics keep the scalar field constant, and the two horizontal components of velocity oscillate with the frequency of inertial waves $\pm f$ out of the plane $k_{||} = 0$, being analogous to the VSHF modes of the full rotating-stratified scenario. In this situation, pancake structures of uniform 2D flows show up, often referred as shear modes. In contrast with the full rotating-stratified case, the slow modes exist only for $k_{||} = 0$, because the dispersion relation becomes trivially null.

In any of the above cases, due to the orthonormality between the columns (i.e. the eigenvectors), we have $\mathbf{M}^{\dagger}\mathbf{M} = \mathbf{I}_3$.
The matrix $\mathbf{M}(\mathbf{k})$ helps in decomposing the linearized dynamics in the subspace of slow and fast manifolds:

$$\mathbf{M}^{\dagger}\mathbf{L}\mathbf{M} = \begin{pmatrix} -i\sigma_{\mathbf{k}} & 0 & 0 \\ 0 & 0 & 0 \\ 0 & 0 & i\sigma_{\mathbf{k}} \end{pmatrix}.$$

4.5.2 Projecting the Forcing on the Slow or Fast manifold

In each of the given cases, it is possible to expand any vector $\hat{\mathbf{F}}(\mathbf{k}) = \left(\hat{F}_1, \hat{F}_2, \hat{F}_3, \hat{F}_\phi\right)^T$ within the linearised system basis constituted by the $\mathbf{Z}_{(i)}(\mathbf{k})$, by means of

$$\hat{\mathbf{F}}(k) = \sum_{i=0,\pm} A_i(\mathbf{k})\mathbf{Z}_i(\mathbf{k}), \tag{4.64}$$

where the amplitudes are given by the projection of the vector on the correspondent basis vector.
So, in the case of $k_{||} \neq 0, k_\perp \neq 0$ it is obtained, for the slow mode projection:

$$A_0(\mathbf{k}) = \frac{Nk_1\hat{F}_2(\mathbf{k}) - Nk_2\hat{F}_1(\mathbf{k}) - f\,k_{||}\hat{F}_\phi(\mathbf{k})}{k\sigma(\mathbf{k})} \tag{4.65}$$

and for the projections over the fast modes

$$A_{(\pm)}(\mathbf{k}) = \tag{4.66}$$
$$\frac{1}{\sqrt{2}\,k\,k_\perp}\left\{k_{||}\left[\frac{f}{\sigma(\mathbf{k})}\left(k_2\hat{F}_1(\mathbf{k}) - k_1\hat{F}_2(\mathbf{k})\right) \pm i\left(k_1\hat{F}_1(\mathbf{k}) + k_2\hat{F}_2(\mathbf{k})\right)\right] \mp i\,k_\perp^2\hat{F}_3(\mathbf{k}) - \frac{N}{\sigma(\mathbf{k})}k_\perp^2\hat{F}_\phi(\mathbf{k})\right\}$$

On the basis of previous comments, a vortex-only forcing is obtained by projecting the original forcing vector along the specific eigen-vector, $\hat{\mathcal{F}}(\mathbf{k}) = A_0(\mathbf{k})\mathbf{Z}_0(\mathbf{k}) = \hat{\mathbf{P}}_0(\mathbf{k})\hat{\mathbf{F}}(\mathbf{k})$.

If we do so, the vortical (slow manifold) components are related to the original ones via the following system:

$$\begin{cases} \hat{\mathcal{F}}_1(\mathbf{k}) = -\left(\dfrac{N\,f}{\sigma^2(\mathbf{k})}\right)\dfrac{k_2}{k^2}\left[\dfrac{N}{f}\left(k_1\hat{F}_2(\mathbf{k}) - k_2\hat{F}_1(\mathbf{k})\right) - k_{||}\hat{F}_\phi(\mathbf{k})\right] \\ \hat{\mathcal{F}}_2(\mathbf{k}) = \left(\dfrac{N\,f}{\sigma^2(\mathbf{k})}\right)\dfrac{k_1}{k^2}\left[\dfrac{N}{f}\left(k_1\hat{F}_2(\mathbf{k}) - k_2\hat{F}_1(\mathbf{k})\right) - k_{||}\hat{F}_\phi(\mathbf{k})\right] \\ \hat{\mathcal{F}}_3(\mathbf{k}) = 0 \\ \hat{\mathcal{F}}_\phi(\mathbf{k}) = -\left(\dfrac{Nf}{\sigma^2(\mathbf{k})}\right)\dfrac{k_{||}}{k^2}\left[k_1\hat{F}_2(\mathbf{k}) - k_2\hat{F}_1(\mathbf{k}) - \dfrac{f}{N}k_{||}\hat{F}_\phi(\mathbf{k})\right] \end{cases} \tag{4.67}$$

The forcing projected on wave modes is $\hat{\mathcal{W}}(\mathbf{k}) = A_-(\mathbf{k})\hat{\mathbf{Z}}_-(\mathbf{k}) + A_+(\mathbf{k})\hat{\mathbf{Z}}_+(\mathbf{k}) = \hat{\mathbf{P}}_W(\mathbf{k})\hat{\mathbf{F}}(\mathbf{k})$, which results in the following system for the forcing components:

$$\begin{aligned}
\hat{\mathcal{W}}_1(\mathbf{k}) &= \frac{1}{k^2\,\sigma^2(\mathbf{k})}\left[\frac{k_{||}^2}{k_\perp^2}\left(f^2k_2^2+\sigma^2(\mathbf{k})\,k_1^2\right)\hat{F}_1(\mathbf{k}) + \frac{k_{||}^2}{k_\perp^2}k_1k_2\left(\sigma^2(\mathbf{k})-f^2\right)\hat{F}_2(\mathbf{k}) - k_2\,k_{||}\,N\,f\hat{F}_\phi(\mathbf{k})\right] \\
&\quad -\frac{k_1\,k_{||}}{k^2}\hat{F}_3(\mathbf{k}) \\
\hat{\mathcal{W}}_2(\mathbf{k}) &= \frac{1}{k^2\,\sigma^2(\mathbf{k})}\left[\frac{k_{||}^2}{k_\perp^2}k_1\,k_2\left(\sigma^2(\mathbf{k})-f^2\right)\hat{F}_1(\mathbf{k}) + \frac{k_{||}^2}{k_\perp^2}\left(f^2\,k_1^2+\sigma^2(\mathbf{k})\,k_2^2\right)\hat{F}_2(\mathbf{k}) + k_1k_{||}Nf\hat{F}_\phi(\mathbf{k})\right] \\
&\quad -\frac{k_2\,k_{||}}{k^2}\hat{F}_3(\mathbf{k}) \\
\hat{\mathcal{W}}_3(\mathbf{k}) &= -\frac{k_1k_{||}}{k^2}\hat{F}_1(\mathbf{k}) - \frac{k_2k_{||}}{k^2}\hat{F}_2(\mathbf{k}) + \frac{k_\perp^2}{k^2}\hat{F}_3(\mathbf{k}) \\
\hat{\mathcal{W}}_\phi(\mathbf{k}) &= \left(\frac{N\,f}{\sigma^2(\mathbf{k})}\right)\frac{1}{k^2}\left[k_{||}\left(k_1\,\hat{F}_2(\mathbf{k}) - k_2\,\hat{F}_1(\mathbf{k})\right) + \frac{N}{f}\,k_\perp^2\hat{F}_\phi(\mathbf{k})\right]
\end{aligned} \tag{4.68}$$

Hence given any $4C3D$ vector $(\mathbf{F}, F_\phi)$, we can construct a forcing acting on the slow manifold or on the fast manifold only. This has in general a complex form as seen above.

Forcing on perpendicular modes only $k_{||} = 0$, $k_\perp \neq 0$

Now we want to analyse the specific form of the forcing if we consider for example only the wavenumbers perpendicular to the gravity/stratification direction or parallel to it.
For the case $k_{||} = 0$ we end up with

$$A_0(\mathbf{k}) = \frac{k_1\hat{F}_2(\mathbf{k}) - k_2\hat{F}_1(\mathbf{k})}{k_\perp}\,, \qquad A_\pm(\mathbf{k}) = \frac{1}{\sqrt{2}}\left(\mp\,i\,\hat{F}_3(\mathbf{k}) - \hat{F}_\phi(\mathbf{k})\right) \tag{4.69}$$

Then a forcing acting on the **Slow Mode** would be, from eqs.(4.67),

$$\begin{cases}
\hat{\mathcal{F}}_1(\mathbf{k}) = \dfrac{1}{k_\perp^2}\left(k_2^2\hat{F}_1(\mathbf{k}) - k_1\,k_2\,\hat{F}_2(\mathbf{k})\right) \\
\hat{\mathcal{F}}_2(\mathbf{k}) = \dfrac{1}{k_\perp^2}\left(-k_1k_2\hat{F}_1(\mathbf{k}) + k_1^2\hat{F}_2(\mathbf{k})\right) \\
\hat{\mathcal{F}}_3(\mathbf{k}) = 0 \\
\hat{\mathcal{F}}_\phi(\mathbf{k}) = 0
\end{cases} \tag{4.70}$$

That is it would be a 2D2C forcing acting only in the perpendicular plane, on the perpendicular components. So we recover what is indeed usually done e.g. to observe an inverse cascade in the system.

Differently a forcing acting on the **Fast wave modes**, but with $k_{||} = 0$, would be

$$\begin{cases}
\hat{\mathcal{W}}_1(\mathbf{k}) = 0 \\
\hat{\mathcal{W}}_2(\mathbf{k}) = 0 \\
\hat{\mathcal{W}}_3(\mathbf{k}) = \hat{F}_3(\mathbf{k}) \\
\hat{\mathcal{W}}^\phi(\mathbf{k}) = \hat{F}^\phi(\mathbf{k})
\end{cases} \tag{4.71}$$

This indicates that a 1C2D forcing acting only on the vertical component of the velocity and injecting energy on the horizontal wavenumbers only should *preferably* inject energy into the waves.

Forcing on parallel modes only $k_\perp = 0$, $k_{||} \neq 0$

Here we analyse the complementary situation of a forcing acting on the parallel modes only.
We find for the slow and fast modes amplitudes

$$A_0(\mathbf{k}) = -\hat{F}_\phi(\mathbf{k})\,, \qquad A_\pm(\mathbf{k}) = \frac{1}{\sqrt{2}}\left(\hat{F}_2(\mathbf{k}) \mp i\hat{F}_1(\mathbf{k})\right) \tag{4.72}$$

By repeating the game as above, a forcing on the **Slow Mode** would have the form

$$\begin{cases} \hat{\mathcal{F}}_1(\mathbf{k}) = 0 \\ \hat{\mathcal{F}}_2(\mathbf{k}) = 0 \\ \hat{\mathcal{F}}_3(\mathbf{k}) = 0 \\ \hat{\mathcal{F}}_\phi(\mathbf{k}) = \hat{F}_\phi(\mathbf{k}) \end{cases} \tag{4.73}$$

Hence there is no way to force the slow manifold acting on parallel modes only. Clearly we kind of knew it, but it is nice to derive it from *principles*.

As for the forcing on **fast-wave modes** and $k_\perp = 0$,

$$\begin{cases} \hat{\mathcal{W}}_1(\mathbf{k}) = \hat{F}_1(\mathbf{k}) \\ \hat{\mathcal{W}}_2(\mathbf{k}) = \hat{F}_2(\mathbf{k}) \\ \hat{W}_3(\mathbf{k}) = 0 \\ \hat{W}_\phi(\mathbf{k}) = 0 \end{cases} \tag{4.74}$$

So we can force the fast waves by applying a forcing acting on the horizontal components of the momentum and on the parallel modes only.
In particular our forcing $\mathbf{F} = (0, A\,\cos(k_{||}z - \omega t), 0)$, with $k_{||}$ being the gravest mode in the compact direction and $\omega \sim f$ is the forcing frequency (close to the one of inertial waves), fall in this kind.
We also note that setting $\omega = 0$, these reduced forcings (acting on $k_{||}$ or $k_\perp$ only) do not depend neither on the Coriolis frequency, f, nor on the Brunt-Väisälä frequency, N.

Forcing with $k_1 = k_2 = k_3 = k \neq 0$

Now we consider the case in which we act on modes with equal amplitude in the three directions, $\mathbf{k} = (k, k, k)$ and $|\mathbf{k}| = \sqrt{3}\,k$. The first thing to notice is that the frequency becomes independent from the value of the wavenumber k in this case. The slow and fast mode amplitudes become

$$A_0(\mathbf{k}) = \frac{N\hat{F}_2(\mathbf{k}) - N\hat{F}_1(\mathbf{k}) - f\hat{F}_\phi(\mathbf{k})}{\sqrt{2\,N^2 + f^2}} \tag{4.75}$$

$$A_\pm(\mathbf{k}) = \frac{1}{2\sqrt{3}}\left\{\sqrt{\frac{3f^2}{2N^2 + f^2}}\left(\hat{F}_1(\mathbf{k}) - \hat{F}_2(\mathbf{k})\right) \mp i\,\left(\hat{F}_1(\mathbf{k}) + \hat{F}_2(\mathbf{k})\right) + \right. \tag{4.76}$$

$$\left. \pm\; 2i\,\hat{F}_3(\mathbf{k}) - 2\frac{\sqrt{3N^2}}{2N^2 + f^2}\hat{F}_\phi(\mathbf{k})\right\} \tag{4.77}$$

By repeating the game as above, a forcing on the **Slow Mode** would have the form

$$\begin{cases} \hat{\mathcal{F}}_1(\mathbf{k}) = \dfrac{N\,f}{2\,N^2+f^2}\left[\dfrac{N}{f}\left(\hat{F}_1(\mathbf{k})-\hat{F}_2(\mathbf{k})\right)+\hat{F}_\phi(\mathbf{k})\right] \\ \hat{\mathcal{F}}_2(\mathbf{k}) = -\dfrac{N\,f}{2\,N^2+f^2}\left[\dfrac{N}{f}\left(\hat{F}_1(\mathbf{k})-\hat{F}_2(\mathbf{k})\right)-\hat{F}_\phi(\mathbf{k})\right] \\ \hat{\mathcal{F}}_3(\mathbf{k}) = 0 \\ \hat{\mathcal{F}}_\phi(\mathbf{k}) = \dfrac{N\,f}{2N^2+f^2}\left[\left(\hat{F}_1(\mathbf{k})-\hat{F}_{(2)}(\mathbf{k})\right)+\dfrac{f}{N}\hat{F}_\phi(\mathbf{k})\right] \end{cases} \tag{4.78}$$

While the a forcing acting on the **Fast Modes** would read:

$$\begin{cases} \hat{\mathcal{W}}_1(\mathbf{k}) = \dfrac{1}{2N^2+f^2}\left[\dfrac{N^2+2f^2}{3}\hat{F}_1(\mathbf{k})+\dfrac{N^2-f^2}{3}\hat{F}_2(\mathbf{k})-\dfrac{2N^2+f^2}{3}\hat{F}_3(\mathbf{k})-Nf\hat{F}_\phi(\mathbf{k})\right] \\ \hat{\mathcal{W}}_2(\mathbf{k}) = \dfrac{1}{2N^2+f^2}\left[\dfrac{N^2-f^2}{3}\hat{F}_1(\mathbf{k})+\dfrac{N^2+2f^2}{3}\hat{F}_2(\mathbf{k})-\dfrac{2N^2+f^2}{3}\hat{F}_3(\mathbf{k})+Nf\hat{F}_\phi(\mathbf{k})\right] \\ \hat{\mathcal{W}}_3(\mathbf{k}) = \dfrac{1}{2N^2+f^2}\left[-\dfrac{2N^2+f^2}{3}\left(\hat{F}_1(\mathbf{k})+\hat{F}_2(\mathbf{k})-2\hat{F}_3(\mathbf{k})\right)\right] \\ \hat{\mathcal{W}}_\phi(\mathbf{k}) = \dfrac{1}{2N^2+f^2}\left[-Nf\hat{F}_1(\mathbf{k})+Nf\hat{F}_2(\mathbf{k})+2N^2\hat{F}_\phi(\mathbf{k})\right]. \end{cases} \tag{4.79}$$

It is clear that in this almost general case, the forcing is quite complex, even if we take $F_\phi = 0$ as it is standard.

5

Conclusions and Future Perspectives

"If you can keep your head when all about you
Are losing theirs and blaming it on you
If you can trust yourself when all men doubt you,
But make allowance for their doubting too:
If you can wait and not be tired by waiting, ...
...you'll be a Man, my son!"

J. R. Kipling,
If

In this thesis we have followed the approach of looking at the ocean circulation from a very broad perspective, always searching for that necessary trade-off between simplified and complex models (see figure 5.1), starting with a focus on large scale

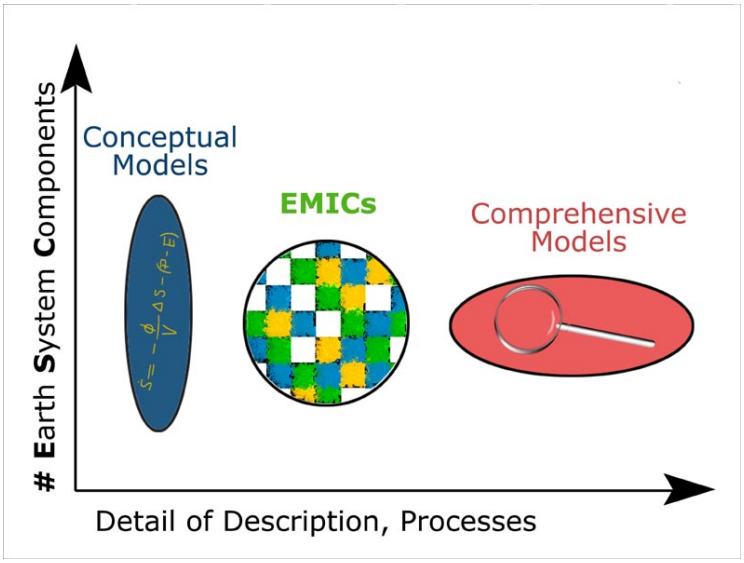

Figure 5.1. Simplified sketch of model's hierarchy when dealing with complex phenomena, such as the climate. Figure taken from Lohmann et al. (2003).

ocean circulation (looking both at the Stommel model and to state-of-the-art reanalyses), to arrive, enhancing the level of detail toward a closer look on smaller scales. That's why this thesis is composed by two parts: a first in which I have presented results stemming from the analysis of large scale Atlantic Meridional Overturning Circulation (AMOC) in state of the art reanalysis products, and a second part in which I studied, with a more theoretically oriented perspective, features of a rotating stratified turbulent flow.
In particular, regarding the first part we reviewed, characterized and interpreted the mid-long term variability of a crucial component of the Earth climate system, basing upon existing literature and the comparison between products. Comparing reanalyses which cover a period of about 40 years (from about 1979 to 2018), we can see that all of them agree on the presence of a pronounced mid-long term variability in the meridional volume transport of watermasses in the Atlantic Ocean. Different products show different amplitudes for this long term variability. Known facts from the literature suggested us that *there is one or more underlying physical mechanisms* behind this long term variability. The shorter time extent of the other data used - see Global Reanalysis multi-model Ensemble Products (GREP), in-situ measurements (e.g. (RAPID-MOCHA) Meridional Overturning Circulation and Heatflux Array, South Atlantic Moc Basin-wide Array) do not allow to discern which of the dataset is closer to reality. There is supporting evidence that this mid-long term variability is the oceanic response to persistent positive phase of North Atlantic Oscillation (NAO) prior mid-1990s (Robson et al. (2012), Robson et al. (2014), Häkkinen et al. (2011)), and we exploited its profound impacts on Gulf Stream (GS) front variability, as well on Deep Water Formation (DWF) in Labrador and Greenland-Iceland-Norwegian (GIN) seas, finding consistency between a phase of higher volume transport, stronger Gulf Stream (GS) and enhanced deep convection in Labrador sea prior to mid-1990s, followed by a phase of weakened circulation afterwards. The oceanic response to the atmosphere takes place via subpolar gyre (SPG) subtropical gyre (STG) variations, which are one at expense of the other and vice versa. Depending on the phase, salt intrusion toward north east are promoted or inhibited, and this has an effect on how deep convection can develop, affecting also the transport itself via the salt advection feedback (refer to figure 3.8).
In one of the datasets (ORAS5) the mid-long term variability is over-amplified with respect to the others, and we suggest that this is due to an excessively strong flux-adjustment, carried out in order to reduce Sea Surface Temperature (SST) biases along the front of Gulf Stream (GS), as described in Tietsche et al. (2020) (see figure 6(a), showing the control run, i.e. the run in which no data have been assimilated, with and without Sea Surface Temperature nudging). Our results confirmed the need of future research effort to understand and better characterize with sensitivity experiments the impact of data assimilation on large scale ocean circulation.

Internal-gravity waves are one of the processes which are thought to play a role in Atlantic Meridional Overturning Circulation (AMOC) variability (Johnson et al. (2019) and references therein), but space and timescales on which they act are out of reach of direct inclusion within a global ocean simulation up to the current situation. To this aim, in the second part of the thesis we studied with a more theoretically oriented perspective a way to disentangle, and ultimately selectively forcing only

waves or vortices in a rotating stratified turbulent flow. The study is carried out working with Navier-Stokes equations within the Boussinesq approximation, in a simpler statistically homogeneous domain, which neglects border, topographic effects. In a realistic ocean dynamics description, one is not able to select a type of forcing, because the drivers of Earth's climate system are fixed according to external factors, such as the action of the Sun and the Moon, wind and pressure variations, Earth rotation. At the current stage, we have verified that this forcing decomposition is coherent with what we already know from the literature, reproducing limiting cases of purely rotating/stratified flows. Future development of this last part will involve the implementation of this decomposition in the code, followed by direct numerical simulation, which will tell if well-established paradigms (such as the promotion of Vertically Sheared Horizontal Flow (VSHF) modes in the highly stratified case, or the impossibility to excite slow modes outside the $k_{||} = 0$ region in the purely rotating case) have to be reconsidered, and eventually reconnected with their real-world complex counterpart, in which there are topographic boundaries and realistic features. Nevertheless, the vortex-wave linear eigenmodes decomposition can be useful in analyzing open-ocean areas, for example to test how the energy is partitioned amongst different modes (fast or slow) with a fixed parameterization of the small-scale physics, as an alternative to well-established flow decompositions (Buzzicotti et al. (2021)).

Future research efforts will be also devoted to search if there are some high frequency data on which it is possible to carry out the wave-vortex decomposition outlined in the last chapter, to explore if there are signatures of internal waves on the ocean large scales. Last but not least, this thesis confirmed the need to design a suitable General Circulation Model (GCM) experiment to continue testing the Atlantic Meridional Overturning Circulation (AMOC) sensitivity to data assimilation, variations in the forcing factors, spatial and temporal resolution.

Here there's a point-by-point summary of the main conclusions from each chapter of this work, and a trace of future research directions.

- **Chapter 2** introduced the Atlantic Overturning, reviewing the literature, current understanding and open problems related to it. This gave us the opportunity to approach the problem from a broad perspective, which encompass simplified models (e.g. the Stommel 1961 model for thermohaline circulation), as well its complexity in a general ocean circulation model with data assimilation.

- **Chapter 3** described our efforts to understand and characterize the regime change characterizing ORAS5 data. Future work after this analysis should be dedicated to design a suitable model experiment, in order to test the sensitivity of Atlantic Meridional Overturning Circulation to data assimilation, variations in forcing factors, parameterizations and parameters of the model.

- **Chapter 4** gave us the chance to study Rotating Stratified Turbulent (RST) flows and its application to geophysical flows from a more theoretical perspective. After setting up and having explored the consistency of vortex-wave linear eigenmodes decomposition with well-known facts from the literature, this

chapter is still far from being conclusive. Future work should be dedicated to implement the decomposition numerically, and to carry out Direct Numerical Simulation (DNS) to exploit its consequences on the energy partition among different modes.

- **Future long-term perspectives** should involve research efforts act to characterize the sensitivity of Atlantic Overturning variability to forcing factors as well as to technical aspects such as the nudging of temperatures and to the impact of data assimilation. Another important pillar among future challenges is the fundamental understanding of small-scale effects - which are not explicitly resolved by Ocean General Circulation Models - on large scale patterns, and the last part of the thesis can be regarded as a very initial step toward this direction.
  Indeed by the joint use of models characterized by a different degree of complexity one can in principle explore mechanisms underlying a certain physically observed behavior, with the ultimate goal of adding details to the way in which we represent the climate system. In a long term perspective, with this view in mind, the use of linear eigenmodes decomposition could shed the light on new ways to develop alternative parameterizations (accounting for the effects of small scales on the largest one), that could be implemented in a model like the Nucleus European for the Modeling of the Ocean (NEMO).

Appendix A

Rotating Stratified Turbulence: some useful calculations

In this appendix we will track some calculation for the interested reader to follow step by step all the details of known results.

A.1 Writing the linearized system in Fourier space

As we said, the starting point are eqn. (4.27). The Fourier expansion read as e.g. for the ℓ-th velocity component

$$u_\ell(\mathbf{x},t) = \sum_{\mathbf{k}} \hat{u}^\ell_{\mathbf{k}}(t)\, e^{i\mathbf{k}\cdot\mathbf{x}} \tag{A.1}$$

we get that the action of any spatial derivative operator is just the multiplication by the corresponding component of the wave vector $\partial_\ell \to ik_\ell$. Notice that in eqn. A.1 $\hat{u}^\ell_{\mathbf{k}}(t) = \hat{u}^\ell(\mathbf{k},t)$. We will treat each term separately for the sake of clarity, collecting all together in the end. The time-derivative term, is

$$\partial_t \left(\sum_{\mathbf{k}} \hat{u}^\ell_{\mathbf{k}}(t)\, e^{i\mathbf{k}\cdot\mathbf{x}} \right) = \sum_{\mathbf{k}} \partial_t \hat{u}^\ell_{\mathbf{k}}(t)\, e^{i\mathbf{k}\cdot\mathbf{x}} \tag{A.2}$$

we can multiply by $e^{-i\mathbf{k}'\cdot\mathbf{x}}$ and integrate over the space, getting:

$$\frac{1}{V}\int \sum_{\mathbf{k}} \partial_t \hat{u}^\ell_{\mathbf{k}}(t)\, e^{i\mathbf{k}\cdot\mathbf{x}} e^{-i\mathbf{k}'\cdot\mathbf{x}}\, d\mathbf{x} = \frac{1}{V}\sum_{\mathbf{k}} \partial_t \hat{u}^\ell_{\mathbf{k}}(t) \int e^{i(\mathbf{k}-\mathbf{k}')\cdot\mathbf{x}}\, d\mathbf{x} =$$

$$= \sum_{\mathbf{k}} \partial_t \hat{u}^\ell_{\mathbf{k}}(t)\, \delta_{\mathbf{k},\mathbf{k}'} = \partial_t \hat{u}^\ell_{\mathbf{k}'}(t) \tag{A.3}$$

The same happens for the time-derivative term of the scalar field ϕ. Nonlinear terms are tricky to obtain, indeed we have:

$$u_j \partial_j u_\ell = \sum_{\mathbf{p}} \hat{u}^j_{\mathbf{p}} e^{i\mathbf{p}\cdot\mathbf{x}} \partial_j \left(\sum_{\mathbf{q}} \hat{u}^\ell_{\mathbf{q}} e^{i\mathbf{q}\cdot\mathbf{x}} \right) = \sum_{\mathbf{p}}\sum_{\mathbf{q}} \hat{u}^j_{\mathbf{p}} q_j \hat{u}^\ell_{\mathbf{q}} e^{i(\mathbf{p}+\mathbf{q})\cdot\mathbf{x}} \tag{A.4}$$

Again, multiplying by $e^{-i\mathbf{k}'\cdot\mathbf{x}}$ and integrating over the space, we get:

$$\frac{1}{V}\sum_{\mathbf{p}}\sum_{\mathbf{q}}\hat{u}^j_{\mathbf{p}}q_j\hat{u}^\ell_{\mathbf{q}}\int e^{i(\mathbf{p}+\mathbf{q}-\mathbf{k}')\cdot\mathbf{x}}\,d\mathbf{x}=\sum_{\mathbf{p}}\sum_{\mathbf{q}}\hat{u}^j_{\mathbf{p}}q_j\hat{u}^\ell_{\mathbf{q}}\delta_{\mathbf{p}+\mathbf{q},\mathbf{k}'} \tag{A.5}$$

Introducing the variable $\mathbf{s}=\mathbf{p}+\mathbf{q}$ we end up with

$$\mathbf{N\hat{L}T}=\sum_{\mathbf{s}}\sum_{\mathbf{q}}\hat{u}^j_{\mathbf{s}-\mathbf{q}}q_j\hat{u}^\ell_{\mathbf{q}}\delta_{\mathbf{s},\mathbf{k}'}=\sum_{\mathbf{q}}\hat{u}^j_{\mathbf{k}'-\mathbf{q}}q_j\hat{u}^\ell_{\mathbf{q}} \tag{A.6}$$

As a result, the set of equations in Fourier Space can be written by expanding each field as prescribed by eqn. (A.1):

$$\partial_t\hat{u}^\ell_{\mathbf{k}'}(t)+i\sum_{\mathbf{q}}\hat{u}^j_{\mathbf{k}'-\mathbf{q}}q_j\hat{u}^\ell_{\mathbf{q}}+f\varepsilon_{\ell jm}e^{(3)}_j\hat{u}^m_{\mathbf{k}'}=-ik'_\ell\hat{P}_{\mathbf{k}'}-Ne^{(3)}_\ell\hat{\phi}_{\mathbf{k}'}+[\widehat{\mathcal{D}_{u_\ell}(u_\ell)}]_{\mathbf{k}'}+\hat{F}^\ell_{\mathbf{k}'} \tag{A.7}$$

$$\partial_t\hat{\phi}_{\mathbf{k}'}+i\sum_{\mathbf{q}}\hat{u}^j_{\mathbf{k}'-\mathbf{q}}q_j\hat{\phi}_{\mathbf{q}}=[\widehat{\mathcal{D}_\phi(\phi)}]_{\mathbf{k}'}+Ne^{(3)}_j\hat{u}^j_{\mathbf{k}'}+\hat{F}^\phi_{\mathbf{k}'}\,, \tag{A.8}$$

$$ik'_\ell\hat{u}^\ell_{\mathbf{k}'}=0 \tag{A.9}$$

The pressure term can be expressed by multiplying eqn. (A.7) by ik'_ℓ and using the incompressibility condition (A.9): this yields, if the forcing is divergenceless

$$-k'_r\sum_{\mathbf{q}}\hat{u}^j_{\mathbf{k}'-\mathbf{q}}q_j\hat{u}^r_{\mathbf{q}}+if\varepsilon_{rjm}k'_re^{(3)}_j\hat{u}^m_{\mathbf{k}'}=k'^2\hat{P}_{\mathbf{k}'}-iNk'_z\hat{\phi}_{\mathbf{k}'} \tag{A.10}$$

Which gives the following expression for pressure, where the laplacian operator in fourier space can be inverted (i.e. for $k^2\neq 0$):

$$\hat{P}_{\mathbf{k}'}=-\frac{k'_r}{k'^2}\sum_{\mathbf{q}}\hat{u}^j_{\mathbf{k}'-\mathbf{q}}q_j\hat{u}^r_{\mathbf{q}}-i\left(\frac{f\left(k'_1\hat{u}^{(2)}_{\mathbf{k}'}-k'_2\hat{u}^{(1)}_{\mathbf{k}'}\right)-Nk'_3\hat{\phi}_{\mathbf{k}'}}{k'^2}\right) \tag{A.11}$$

We can write our governing equations in Fourier space in compact form, as follows (time-dependence is omitted to keep notation light):

$$\begin{aligned}\partial_t\hat{u}_i(\mathbf{k}) &= -\frac{i}{2}\mathcal{P}_{ijl}\sum_{\mathbf{p}+\mathbf{q}=\mathbf{k}}\hat{u}_j(\mathbf{p})\hat{u}_l(\mathbf{q})+fP_{ij}(\mathbf{k})\varepsilon_{jl3}\hat{u}_l(\mathbf{k})-NP_{i3}(\mathbf{k})\hat{\phi}(\mathbf{k})\\ &\quad -\nu\,k^2\hat{u}_i(\mathbf{k})+P_{ij}(\mathbf{k})\hat{F}_j(\mathbf{k})\,, &\text{(A.12)}\\ \partial_t\hat{\phi}(\mathbf{k}) &= -i\sum_{\mathbf{p}+\mathbf{q}=\mathbf{k}}k^j\hat{u}_j(\mathbf{p})\hat{\phi}(\mathbf{q})+N\hat{u}_3(\mathbf{k})-\kappa k^2\hat{\phi}(\mathbf{k})+\hat{F}_\phi(\mathbf{k})\,, &\text{(A.13)}\\ k^i\hat{u}_i(\mathbf{k}) &= 0\,. &\text{(A.14)}\end{aligned}$$

In the above eqs., we have introduced the projection operator $\mathcal{P}_{ijl}(\mathbf{k})=k_jP_{il}(\mathbf{k})+k_lP_{ij}(\mathbf{k})$, where $P_{ij}(\mathbf{k})=(\delta_{ij}-k_ik_j/k^2)$ is the incompressibility projector, to get rid of the pressure term.

A.2 Derivation of the dispersion relation for inertial-gravity waves

In this section we are going to demonstrate that eqs. 4.38 admit solution with dispersion relation given by 4.39 . In order to do so, let's start by rewriting explicitly each equation:

$$\begin{cases} \partial_t \hat{u}_1(\mathbf{k}) = f\frac{k_1 k_2}{k^2}\hat{u}_1(\mathbf{k}) + f\left(1-\frac{k_1^2}{k^2}\right)\hat{u}_2(\mathbf{k}) + N\frac{k_1 k_3}{k^2}\hat{\phi}(\mathbf{k}) \\ \partial_t \hat{u}_2(\mathbf{k}) = -f\left(1-\frac{k_2^2}{k^2}\right)\hat{u}_1(\mathbf{k}) - f\frac{k_1 k_2}{k^2}\hat{u}_2(\mathbf{k}) + N\frac{k_2 k_3}{k^2}\hat{\phi}(\mathbf{k}) \\ \partial_t \hat{u}_3(\mathbf{k}) = f\frac{k_3 k_2}{k^2}\hat{u}_1(\mathbf{k}) - f\frac{k_3 k_1}{k^2}\hat{u}_2(\mathbf{k}) + -N\left(1-\frac{k_3^2}{k^2}\right)\hat{\phi}(\mathbf{k}) \\ \partial_t \hat{\phi}(\mathbf{k}) = N\hat{u}_3(\mathbf{k}) \\ k_1\hat{u}_1(\mathbf{k}) + k_2\hat{u}_2(\mathbf{k}) + k_3\hat{u}_3(\mathbf{k}) = 0 \end{cases} \tag{A.15}$$

We can take the fourth of eqs. A.15 and calculate its 4-time derivative, using the rest of equations to obtain the following chain of identities:

$$\partial_t^4\hat{\phi}(\mathbf{k}) = N\partial_t^3\hat{u}_3(\mathbf{k}) = -Nf\left[-\frac{k_3 k_1}{k^2}\partial_t^2\hat{u}_2(\mathbf{k}) + \frac{k_3 k_2}{k^2}\partial_t^2\hat{u}_1(\mathbf{k}) - \frac{N}{f}\left(1-\frac{k_3^2}{k^2}\right)\partial_t^2\hat{\phi}(\mathbf{k})\right]$$

which can be rearranged as

$$\left(\partial_t^4 + N^2\frac{k_\perp^2}{k^2}\partial_t^2\right)\hat{\phi}(\mathbf{k}) =$$

$$-Nf\frac{k_3 k_1}{k^2}\left[-f\left(1-\cancel{\frac{k_2^2}{k^2}}\right)\partial_t\hat{u}_1(\mathbf{k}) - \cancel{f\frac{k_1 k_2}{k^2}\partial_t\hat{u}_2(\mathbf{k})} + \cancel{N\frac{k_2 k_3}{k^2}\partial_t\hat{\phi}(\mathbf{k})}\right] +$$

$$+Nf\frac{k_3 k_2}{k^2}\left[\cancel{f\frac{k_1 k_2}{k^2}\partial_t\hat{u}_1(\mathbf{k})} + f\left(1-\cancel{\frac{k_1^2}{k^2}}\right)\partial_t\hat{u}_2(\mathbf{k}) + \cancel{N\frac{k_1 k_3}{k^2}\partial_t\hat{\phi}(\mathbf{k})}\right] \Rightarrow$$

$$\Rightarrow \left(\partial_t^4 + N^2\frac{k_\perp^2}{k^2}\partial_t^2\right)\hat{\phi}(\mathbf{k}) = Nf^2\frac{k_3}{k^2}\partial_t\left(k_1\hat{u}_1 + k_2\hat{u}_2\right) = -Nf^2\frac{k_3^2}{k^2}\partial_t\hat{u}_3(\mathbf{k})$$

which leads to the following relation, involving only the scalar field:

$$\left(\partial_t^4 + N^2\frac{k_\perp^2}{k^2}\partial_t^2 + f^2\frac{k_\parallel^2}{k^2}\partial_t^2\right)\hat{\phi}(\mathbf{k}) = 0. \tag{A.16}$$

At this point, going in frequency space by means of a temporal Fourier transform,

$$\hat{\phi}(\mathbf{k},t) = \frac{1}{\sqrt{2\pi}}\int \hat{\phi}(\mathbf{k},\sigma)\, e^{-i\sigma t}\, d\sigma$$

and using the completeness of this basis, we can get the desired dispersion relation:

$$\left(\sigma^4 - N^2\frac{k_\perp^2}{k^2}\sigma^2 - f^2\frac{k_\parallel^2}{k^2}\sigma^2\right) = 0.$$

which simply yields the dispersion relation expressed by eq. 4.39. Notice that this derivation, though maybe not so physical, brings to the same result of the standard derivation, which can be found in the textbook of Gill (2016), chapter 8, page 256.

A.3 Technical Details: *Complete* description

Direct Numerical Simulation of turbulent flows are heavy from the computational point of view, due mainly to nonlinear terms of the governing equations.
Complete is based on a fully dealiased parallel pseudospectral algorithm with second order Adam–Bashforth time-stepping. Originally developed by Federico Toschi, Alessandro Corbetta, Luca Biferale, many other collaborators have been working on this code, which has never been really strictly documented. In this section we will try to detail the steps to solve our physical problem. Pseudo-spectral methods strongly reduce computational costs: all convolutions are carried out as algebraic products in Fourier Space, the rest of calculations being done in the Real Space. The advantage becomes evident when one considers the structure of the Navier-Stokes Equations, in which all the spatial wave-numbers are coupled one with each other through the nonlinear term Orszag and Patterson Jr (1972), Pope (2001).
The structure of the data is a 3D array of `structs`, which in the real space is something like

$$u\,[x]\,[y]\,[z]\,.\,\{vx, vy, vz\}\,.$$

In the complex space there's a further `struct` level, i.e. the Real and Imaginary part.
Parallel 3D Fast Fourier Transform Pekurovsky (2012) is employed (P3DFFT), and the parallelization is different from Real to Fourier space:

- Real space: parallelized directions are x and y;
- Fourier space: parallelized directions are y and z.

Only within this section, we will assume rotation and stratification aligned toward the x-direction of the simulation domain. In the next sections, when we will discuss physical, rather than technical aspects, rotation and stratification will be aligned with the z-axis as usual.

Parallel Structure - Cubic and Slab Domain

We will consider in this paragraph how memory is organized between different parallel processes, in order to understand what happens when considering domains with non unitary aspect ratios. When considering a cubic domain of unitary aspect ratio, dimensions of the grid-spacing along different dimension are all equal. This mean that $\Delta x = \Delta y = \Delta z$, and the same can be said about grid-spacing in Fourier space. With reference to figure A.1, if we imagine to have a cubic 64^3 domain in real space, and we split our parallelization on four processes, the distribution of modes in Fourier space follows as:

- processor 0 will contain $k_z \in [0, 16)\,,\ k_y \in [0, 32)$ - the local (1,0,0) index will point to mode $(k_x = 1, k_y = 0, k_z = 0)$;
- processor 1 will contain $k_z \in [16, 32]\,,\ k_y \in [0, 32)$ - the local (1,0,0) index will point to mode $(k_x = 1, k_y = 0, k_z = 16)$;
- processor 2 will contain $k_z \in [0, 16)\,,\ k_y \in [-32, -1]$ - the local (1,0,0) index will point to mode $(k_x = 1, k_y = -32, k_z = 0)$;

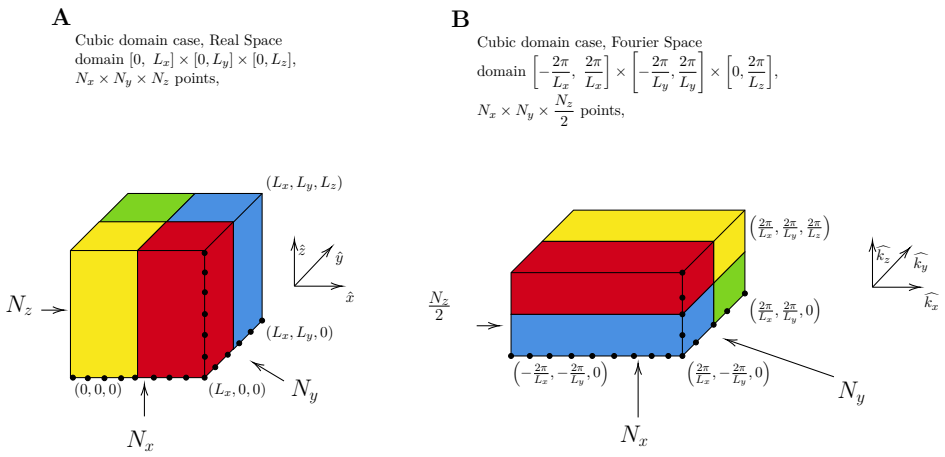

Figure A.1. Direction of the parallelization in the x-space vs the k-space in a cubic domain case (unitary aspect ratio). Color code is processor 0, processor 1, processor 2, processor 3.

- processor 3 will contain $k_z \in [16, 32]\,,\ k_y \in [-32, -1]$ - the local (1,0,0) index will point to mode $(k_x = 1, k_y = -32, k_z = 16)$.

Let's now turn our attention to the case in which the domain is a slab with $L_x = 1000\,, L_z = 100$. The grid-spacing is fixed as in the cubic case, having $\Delta x = \Delta y = \Delta z$ equal to 1 meter, for example. What is different in this case is the grid-spacing in k-space:

$$\Delta k_x = \frac{2\pi}{L_x} \qquad \Delta k_z = \frac{2\pi}{L_z} \tag{A.17}$$

from which we can observe that, having imposed the slab domain with $L_x \gg L_z$, this will imply that $\Delta k_z \gg \Delta k_x$.
If we imagine a real oceanic situation, in which the vertical length scale is about two order of magnitude smaller than the horizontal scale, this will result in a k-space grid-spacing which in the vertical direction is about two order of magnitude greater than the horizontal one.
This fact constitute a major constraint on the modes which is possible to excite and resolve in the simulation, depending on how the forcing is designed: for example in our case (we will see the details in next sections), this will have only components on a direction perpendicular to the rotation axis (or the compressed dimension), which will depend on the vertical wavenumber, in such a way to excite only very large scales vertical motions. Further details will be given in the sections below (see paragraph on the forcing in section A.3.1).
A debug flag permits to reconstruct the distribution of modes along different processors [1]. For example, if we have a $32 \times 64 \times 64$ domain, with rotation aligned on the x-axis of the simulation, running on 4 processors we will have the same distribution of modes as in the cubic case, except that the grid spacing along the compact dimension is changed:

[1] The option *DEBUG_WAVENUMBERS* permits to write the name of the processor and the wavenumber it contains, both on integer and parallelized directions on a file named $k.p_{idx}.p_{idy}$, where p_{idx}, p_{idy} are respectively the id of processors along parallel directions.

- $\Delta k_z = 2\Delta k_x = 2\Delta k_y, \quad \Delta k_x = 1;$

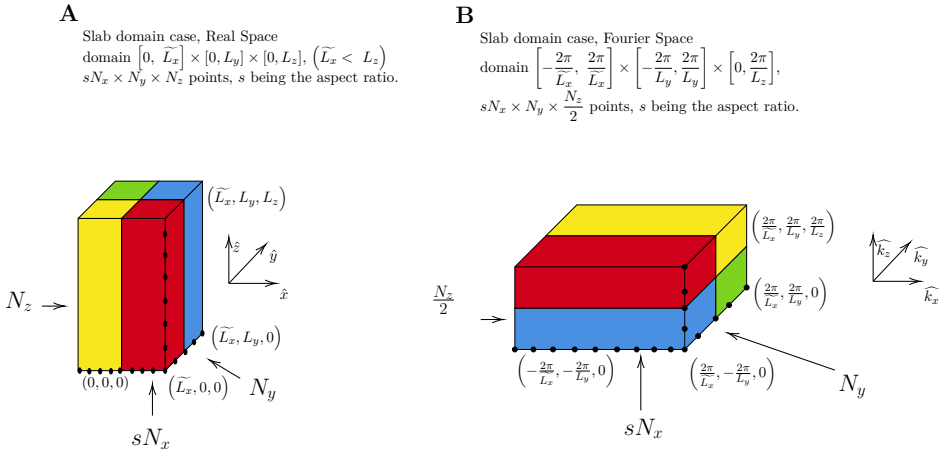

Figure A.2. Direction of the parallelization in the x-space vs the k-space in a slab domain case (non unitary aspect ratio). Color code is processor 0, processor 1, processor 2, processor 3.

The routine which intialize the wavenumbers is such that on x and y we have both negative and positive wavenumbers, while in z only positive wavenumber are present. The situation is depicted in an example in figure A.2.
In figures A.1, A.2, we choosed to represent the situation as in the simulation setup: the rotation and stratification are aligned along the x-axis, and the slab-domain is created by shrinking the cubic domain along the x-direction.

A.3.1 How the various terms are calculated in the code

Looking at the structure of the main code, which is enclosed in *Complete/euler/-main.c*, we can see that the code is divided in `STEPS`. The code works on the vector potential **b** (and its complex Fourier counterpart **cb**), which is related to the eulerian velocity field by

$$\mathbf{u} = \nabla \times \mathbf{b}. \tag{A.18}$$

All the initial steps are used to initialize and de-alias Patterson Jr and Orszag (1971) the fields, depending on compilation flags used, till `STEP G`, where the initialized field is copied onto the nonlinear term.
Before moving on, some reference has to be made to wave vectors. They are defined in the routine *Complete/initks.c*, and each wave-vector is from 0 to $N_{k_i} - 1$, where k_i stands for the given direction. For example, the wave-vector along the x-direction is a vector going from 0 to $N_{k_x} - 1$, filled with positive integers from 0 to $\frac{\texttt{size}(x)}{2} - 1$, and with negative integers from $\frac{\texttt{size}(x)}{2}$ to $\texttt{size}(x)$. After `STEP G` the call to the routine *Complete/nlt.c* follows. After the call to this function, which does the main part of the calculation, the dealiasing of the nonlinear term, followed by the first temporal step made with euler scheme is carried out in `STEP J`, `STEP K` (next advances in time are done with second order Adams-Bashforth Butcher and Goodwin (2008) implicit scheme).

the routine nlt.c

In this routine (`STEP A`), the velocity field is calculated making the curl of the vector potential, which is done recasting eqn. (A.18) in Fourier Space (the tilde denotes Fourier-transformed fields):

$$\tilde{\mathbf{u}} = i\mathbf{k} \times \tilde{\mathbf{b}}, \tag{A.19}$$

which imply that, respectively we found for the real

$$\Re(\tilde{\mathbf{u}}) = -\mathbf{k} \times \Im\left(\tilde{\mathbf{b}}\right) \tag{A.20}$$

and imaginary part

$$\Im(\tilde{\mathbf{u}}) = \mathbf{k} \times \Re(\tilde{\mathbf{u}}). \tag{A.21}$$

Then, vorticity is calculated (`STEP B`) as $\mathbf{w} = -\nabla^2\mathbf{b}$, which again in Fourier space reads as

$$\tilde{\mathbf{w}} = k^2\tilde{\mathbf{b}}. \tag{A.22}$$

Inverse transform is used to return to Real space (`STEP C`). Now $\mathbf{b}$ contains the vorticity vector in real space.
If the rotation flag is enabled, external rotation is added to the vorticity field and the construction of the nonlinear term begin

$$\mathbf{NLT} = \mathbf{u} \times \mathbf{w} \tag{A.23}$$

is computed (`STEP E`), together with the scalar field, which is treated by calculating the normalized product of $\mathbf{u}\phi$, placing in a temporary array

$$\mathbf{u}_{scal} = \mathbf{u}\phi \tag{A.24}$$

Now (`STEP F`) is time to turn to k-space with a direct transform: $\tilde{\mathbf{NLT}}$ contains the Fourier transform of eqn. (A.23).
The nonlinear term, complete of rotational part is calculated in real space in `STEP G` as:

$$\mathbf{b}_{nl} = \Delta^{-1}(\nabla \times \mathbf{NLT}), \tag{A.25}$$

which is casted in Fourier space as

$$\tilde{\mathbf{b}}_{nl} = \frac{i\mathbf{k} \times \tilde{\mathbf{NLT}}}{k^2}. \tag{A.26}$$

If the flag for the scalar is active, also the term $\nabla \cdot \mathbf{u}_{scal}$ is calculated: the addition of the term $\tilde{\mathbf{N}} \cdot \tilde{\mathbf{u}}$ conclude the calculation of the nonlinear term for the scalar field: in formulae

$$\tilde{\phi}_{nl} = i\mathbf{k} \cdot \tilde{\mathbf{u}}_{scal} + \tilde{\mathbf{N}} \cdot \tilde{\mathbf{u}} \tag{A.27}$$

If the boussinesq flag is active too, the boussinesq term

$$\Delta^{-1}(\nabla \times (-\phi(N_x, N_y, N_z))) \tag{A.28}$$

is added to the nonlinear term calculated above in Fourier Space, which means the addition of a term like

$$\frac{\mathbf{k} \times \mathbf{N}}{k^2}\phi,$$

which, depending on the choice of initial parameters, can have components on whatever direction, and complete the budget of terms when Boussinesq equation is written in terms of vorticity. We recall in our setup rotation and stratification are aligned along the x-axis. Note that, separating the components of the complex field we have the addition of terms which are respectively with opposite sign respect to the ones in eqn.(A.20), (A.21): for the real part

$$\frac{\mathbf{k} \times \mathbf{N} \Im\left(\tilde{\phi}\right)}{k^2}, \tag{A.29}$$

whilst for the imaginary part

$$-\frac{\mathbf{k} \times \mathbf{N} \Re\left(\tilde{\phi}\right)}{k^2}. \tag{A.30}$$

Indeed it can be verified that the vorticity form on the equation (4.27), excluding the viscosity and diffusivity and forcing terms can be written as

$$\frac{\partial \mathbf{w}}{\partial t} = \left[(\mathbf{w} + 2\mathbf{\Omega}) \cdot \nabla\right] \mathbf{u} - (\mathbf{u} \cdot \nabla)(\mathbf{w} + 2\mathbf{\Omega}) + \nabla \times \mathbf{N}\phi. \tag{A.31}$$

the forcing routine

We decided to set up a forcing like

$$\mathbf{F} = \left(0, A \cos\left(k_x^0 x - \omega t\right), 0\right) \tag{A.32}$$

in which k_x^0 is the gravest mode in the compact direction, and the forcing frequency ω is close to the Coriolis parameter we are imposing on the system. The forcing routine works in Fourier space (and it's done just by the master process, given it's simplicity), and it is called after the nonlinear term. Then there's the advance in time and the whole loop start again (some diagnostics to calculate some observables are in the middle when necessary and will not be described for the moment).

Bibliography

Abraham, J. P., Baringer, M., Bindoff, N., Boyer, T., Cheng, L., Church, J., Conroy, J., Domingues, C., Fasullo, J., Gilson, J., et al. (2013). A review of global ocean temperature observations: Implications for ocean heat content estimates and climate change. *Reviews of Geophysics*, 51(3):450–483.

Adcroft, A., Campin, J.-M., Dutkiewicz, S., Evangelinos, C., Ferreira, D., Forget, G., Fox-Kemper, B., Heimbach, P., Hill, C., Hill, E., et al. (2018). Mitgcm documentation. *Release checkpoint67a-12-gbf23121*, 19.

Alkhayuon, H., Ashwin, P., Jackson, L. C., Quinn, C., and Wood, R. A. (2019). Basin bifurcations, oscillatory instability and rate-induced thresholds for atlantic meridional overturning circulation in a global oceanic box model. *Proceedings of the Royal Society A*, 475(2225):20190051.

Andrews, D. and Mcintyre, M. E. (1976). Planetary waves in horizontal and vertical shear: The generalized eliassen-palm relation and the mean zonal acceleration. *Journal of the Atmospheric Sciences*, 33(11):2031–2048.

Balan Sarojini, B., Gregory, J., Tailleux, R., Bigg, G., Blaker, A., Cameron, D., Edwards, N., Megann, A., Shaffrey, L., and Sinha, B. (2011). High frequency variability of the atlantic meridional overturning circulation. *Ocean Science*, 7(4):471–486.

Balmaseda, M. A., Mogensen, K., and Weaver, A. T. (2013a). Evaluation of the ecmwf ocean reanalysis system oras4. *Quarterly journal of the royal meteorological society*, 139(674):1132–1161.

Balmaseda, M. A., Trenberth, K. E., and Källén, E. (2013b). Distinctive climate signals in reanalysis of global ocean heat content. *Geophysical Research Letters*, 40(9):1754–1759.

Bartello, P. (1995). Geostrophic adjustment and inverse cascades in rotating stratified turbulence. *Journal of the atmospheric sciences*, 52(24):4410–4428.

Batchelor, G. K. (1969). Computation of the energy spectrum in homogeneous two-dimensional turbulence. *The Physics of Fluids*, 12(12):II–233.

Bauer, P., Stevens, B., and Hazeleger, W. (2021). A digital twin of earth for the green transition. *Nature Climate Change*, 11(2):80–83.

Biastoch, A., Böning, C. W., Getzlaff, J., Molines, J.-M., and Madec, G. (2008). Causes of interannual–decadal variability in the meridional overturning circulation of the midlatitude north atlantic ocean. *Journal of climate*, 21(24):6599–6615.

Boffetta, G. and Ecke, R. E. (2012). Two-dimensional turbulence. *Annual review of fluid mechanics*, 44:427–451.

Bower, A., Lozier, S., Biastoch, A., Drouin, K., Foukal, N., Furey, H., Lankhorst, M., Rühs, S., and Zou, S. (2019). Lagrangian views of the pathways of the atlantic meridional overturning circulation. *Journal of Geophysical Research: Oceans*, 124(8):5313–5335.

Broecker, W. S. (1991). The great ocean conveyor. *Oceanography*, 4(2):79–89.

Brunner-Suzuki, A.-M. E., Sundermeyer, M. A., and Lelong, M.-P. (2014). Upscale energy transfer by the vortical mode and internal waves. *Journal of Physical Oceanography*, 44(9):2446–2469.

Bryan, F. (1986). High-latitude salinity effects and interhemispheric thermohaline circulations. *Nature*, 323(6086):301–304.

Buckley, M. W. and Marshall, J. (2016). Observations, inferences, and mechanisms of the atlantic meridional overturning circulation: A review. *Reviews of Geophysics*, 54(1):5–63.

Butcher, J. C. and Goodwin, N. (2008). *Numerical methods for ordinary differential equations*, volume 2. Wiley Online Library.

Buzzicotti, M., Storer, B. A., Griffies, S. M., and Aluie, H. (2021). A coarse-grained decomposition of surface geostrophic kinetic energy in the global ocean. *arXiv preprint arXiv:2106.04157*.

Calmanti, S., Artale, V., and Sutera, A. (2006). North atlantic moc variability and the mediterranean outflow: a box-model study. *Tellus A: Dynamic Meteorology and Oceanography*, 58(3):416–423.

Carton, J. A., Penny, S. G., and Kalnay, E. (2019). Temperature and salinity variability in the soda3, ecco4r3, and oras5 ocean reanalyses, 1993–2015. *Journal of Climate*, 32(8):2277–2293.

Castellana, D., Baars, S., Wubs, F. W., and Dijkstra, H. A. (2019). Transition probabilities of noise-induced transitions of the atlantic ocean circulation. *Scientific reports*, 9(1):1–7.

Casulli, V. (1999). A semi-implicit finite difference method for non-hydrostatic, free-surface flows. *International journal for numerical methods in fluids*, 30(4):425–440.

Cessi, P. (2019). The global overturning circulation. *Annual review of marine science*, 11:249–270.

Cheng, L., Trenberth, K. E., Fasullo, J., Boyer, T., Abraham, J., and Zhu, J. (2017). Improved estimates of ocean heat content from 1960 to 2015. *Science Advances*, 3(3):e1601545.

Cheng, L. and Zhu, J. (2015). Influences of the choice of climatology on ocean heat content estimation. *Journal of Atmospheric and Oceanic Technology*, 32(2):388–394.

Cherry, S. (1997). Some comments on singular value decomposition analysis. *Journal of Climate*, 10(7):1759–1761.

Chidichimo, M., Piola, A., Meinen, C., Perez, R., Campos, E., Dong, S., Lumpkin, R., and Garzoli, S. (2021). Brazil current volume transport variability during 2009–2015 from a long-term moored array at 34.5° s. *Journal of Geophysical Research: Oceans*, 126(5):e2020JC017146.

De Coetlogon, G., Frankignoul, C., Bentsen, M., Delon, C., Haak, H., Masina, S., and Pardaens, A. (2006). Gulf stream variability in five oceanic general circulation models. *Journal of physical oceanography*, 36(11):2119–2135.

Delworth, T. L. and Zeng, F. (2016). The impact of the north atlantic oscillation on climate through its influence on the atlantic meridional overturning circulation. *Journal of Climate*, 29(3):941–962.

di Leoni, P. C., Cobelli, P. J., Mininni, P. D., Dmitruk, P., and Matthaeus, W. (2014). Quantification of the strength of inertial waves in a rotating turbulent flow. *Physics of Fluids*, 26(3):035106.

di Leoni, P. C. and Mininni, P. D. (2015). Absorption of waves by large-scale winds in stratified turbulence. *Physical Review E*, 91(3):033015.

Dijkstra, H. A. (2007). Characterization of the multiple equilibria regime in a global ocean model. *Tellus A: Dynamic Meteorology and Oceanography*, 59(5):695–705.

Efron, B. and Tibshirani, R. J. (1994). *An introduction to the bootstrap*. CRC press.

Ferrari, R. and Ferreira, D. (2011). What processes drive the ocean heat transport? *Ocean Modelling*, 38(3-4):171–186.

Ferrari, R. and Wunsch, C. (2009). Ocean circulation kinetic energy: Reservoirs, sources, and sinks. *Annual Review of Fluid Mechanics*, 41.

Fontela, M., García-Ibáñez, M. I., Hansell, D. A., Mercier, H., and Pérez, F. F. (2016). Dissolved organic carbon in the north atlantic meridional overturning circulation. *Scientific reports*, 6(1):1–9.

Frisch, U. (1995). *Turbulence: The Legacy of AN Kolmogorov*. Cambridge University Press.

Gent, P. R. (2018). A commentary on the atlantic meridional overturning circulation stability in climate models. *Ocean Modelling*, 122:57–66.

Gent, P. R. and Mcwilliams, J. C. (1990). Isopycnal mixing in ocean circulation models. *Journal of Physical Oceanography*, 20(1):150–155.

Gill, A. E. (2016). *Atmosphere—ocean dynamics*. Elsevier.

Gouretski, V. and Reseghetti, F. (2010). On depth and temperature biases in bathythermograph data: Development of a new correction scheme based on analysis of a global ocean database. *Deep Sea Research Part I: Oceanographic Research Papers*, 57(6):812–833.

Häkkinen, S., Rhines, P. B., and Worthen, D. L. (2011). Warm and saline events embedded in the meridional circulation of the northern north atlantic. *Journal of Geophysical Research: Oceans*, 116(C3).

Hasselmann, K. (1976). Stochastic climate models part i. theory. *tellus*, 28(6):473–485.

Herbert, C., Marino, R., Rosenberg, D., and Pouquet, A. (2016). Waves and vortices in the inverse cascade regime of stratified turbulence with or without rotation. *Journal of Fluid Mechanics*, 806:165–204.

Herbert, C., Pouquet, A., and Marino, R. (2014). Restricted equilibrium and the energy cascade in rotating and stratified flows. *arXiv preprint arXiv:1401.2103*.

Hirschi, J., Baehr, J., Marotzke, J., Stark, J., Cunningham, S., and Beismann, J.-O. (2003). A monitoring design for the atlantic meridional overturning circulation. *Geophysical Research Letters*, 30(7).

Huang, B., Xue, Y., Kumar, A., and Behringer, D. W. (2012). Amoc variations in 1979–2008 simulated by ncep operational ocean data assimilation system. *Climate dynamics*, 38(3):513–525.

IOC et al. (2015). The international thermodynamic equation of seawater–2010: calculation and use of thermodynamic properties.[includes corrections up to 31st october 2015].

Jackson, L., Dubois, C., Forget, G., Haines, K., Harrison, M., Iovino, D., Köhl, A., Mignac, D., Masina, S., Peterson, K., et al. (2019). The mean state and variability of the north atlantic circulation: A perspective from ocean reanalyses. *Journal of Geophysical Research: Oceans*, 124(12):9141–9170.

Jochum, M., Briegleb, B. P., Danabasoglu, G., Large, W. G., Norton, N. J., Jayne, S. R., Alford, M. H., and Bryan, F. O. (2013). The impact of oceanic near-inertial waves on climate. *Journal of Climate*, 26(9):2833–2844.

Johnson, H. L., Cessi, P., Marshall, D. P., Schloesser, F., and Spall, M. A. (2019). Recent contributions of theory to our understanding of the atlantic meridional overturning circulation. *Journal of Geophysical Research: Oceans*, 124(8):5376–5399.

Jolliffe, I. (2003). Principal component analysis. *Technometrics*, 45(3):276.

Joyce, T. M. and Zhang, R. (2010). On the path of the gulf stream and the atlantic meridional overturning circulation. *Journal of Climate*, 23(11):3146–3154.

Jung, O., Sung, M.-K., Sato, K., Lim, Y.-K., Kim, S.-J., Baek, E.-H., Jeong, J.-H., and Kim, B.-M. (2017). How does the sst variability over the western north atlantic ocean control arctic warming over the barents–kara seas? *Environmental Research Letters*, 12(3):034021.

Kalnay, E., Kanamitsu, M., Kistler, R., Collins, W., Deaven, D., Gandin, L., Iredell, M., Saha, S., White, G., Woollen, J., et al. (1996). The ncep/ncar 40-year reanalysis project. *Bulletin of the American meteorological Society*, 77(3):437–472.

Kanzow, T., Cunningham, S., Johns, W. E., Hirschi, J. J., Marotzke, J., Baringer, M., Meinen, C., Chidichimo, M., Atkinson, C., Beal, L., et al. (2010). Seasonal variability of the atlantic meridional overturning circulation at 26.5 n. *Journal of Climate*, 23(21):5678–5698.

Karspeck, A., Stammer, D., Köhl, A., Danabasoglu, G., Balmaseda, M., Smith, D., Fujii, Y., Zhang, S., Giese, B., Tsujino, H., et al. (2017). Comparison of the atlantic meridional overturning circulation between 1960 and 2007 in six ocean reanalysis products. *Climate Dynamics*, 49(3):957–982.

Keeley, S., Sutton, R., and Shaffrey, L. (2012). The impact of north atlantic sea surface temperature errors on the simulation of north atlantic european region climate. *Quarterly Journal of the Royal Meteorological Society*, 138(668):1774–1783.

Kelly, K. A. (1988). Comment on "empirical orthogonal function analysis of advanced very high resolution radiometer surface temperature patterns in santa barbara channel" by gse lagerloef and rl bernstein. *Journal of Geophysical Research: Oceans*, 93(C12):15753–15754.

Kendall, M. (1975). *Multivariate analysis*. Number BOOK. Charles Griffin.

Kjellsson, J. and Zanna, L. (2017). The impact of horizontal resolution on energy transfers in global ocean models. *Fluids*, 2(3):45.

Kolmogorov, A. N. (1941a). the local structure of turbulence in incompressible viscous fluid for very large reynolds numbers. *Cr Acad. Sci. URSS*, 30:301–305.

Kolmogorov, A. N. (1941b). on degeneration (decay) of isotropic turbulence in an incompressible viscous liquid. In *Dokl. Akad. Nauk SSSR*, volume 31, pages 538–540.

Kolmogorov, A. N. (1941c). dissipation of energy in the locally isotropic turbulence. *CR Acad. Sci. URSS*, 32:16–18.

Kraichnan, R. H. (1967). Inertial ranges in two-dimensional turbulence. *The Physics of Fluids*, 10(7):1417–1423.

Kraichnan, R. H. and Montgomery, D. (1980). Two-dimensional turbulence. *Reports on Progress in Physics*, 43(5):547.

Kuhlbrodt, T., Griesel, A., Montoya, M., Levermann, A., Hofmann, M., and Rahmstorf, S. (2007). On the driving processes of the atlantic meridional overturning circulation. *Reviews of Geophysics*, 45(2).

Lee, T., Awaji, T., Balmaseda, M. A., Greiner, E., and Stammer, D. (2009). Ocean state estimation for climate research. *Oceanography*, 22(3):160–167.

Lenton, T. M., Held, H., Kriegler, E., Hall, J. W., Lucht, W., Rahmstorf, S., and Schellnhuber, H. J. (2008). Tipping elements in the earth's climate system. *Proceedings of the national Academy of Sciences*, 105(6):1786–1793.

Levitus, S., Antonov, J. I., Boyer, T. P., Baranova, O. K., Garcia, H. E., Locarnini, R. A., Mishonov, A. V., Reagan, J., Seidov, D., Yarosh, E. S., et al. (2012). World ocean heat content and thermosteric sea level change (0–2000 m), 1955–2010. *Geophysical Research Letters*, 39(10).

Levitus, S., Antonov, J. I., Boyer, T. P., Locarnini, R. A., Garcia, H. E., and Mishonov, A. V. (2009). Global ocean heat content 1955–2008 in light of recently revealed instrumentation problems. *Geophysical Research Letters*, 36(7).

Li, T., Wan, M., Wang, J., and Chen, S. (2020). Spectral energy transfers and kinetic-potential energy exchange in rotating stratified turbulence. *Physical Review Fluids*, 5(12):124804.

Liu, W. and Liu, Z. (2013). A diagnostic indicator of the stability of the atlantic meridional overturning circulation in ccsm3. *Journal of Climate*, 26(6):1926–1938.

Liu, W., Xie, S.-P., Liu, Z., and Zhu, J. (2017). Overlooked possibility of a collapsed atlantic meridional overturning circulation in warming climate. *Science Advances*, 3(1):e1601666.

Liu, W., Xie, S.-P., and Lu, J. (2016). Tracking ocean heat uptake during the surface warming hiatus. *Nature communications*, 7(1):1–9.

Lohmann, G., Butzin, M., Grosfeld, K., Knorr, G., Paul, A., Prange, M., Romanova, V., and Schubert, S. (2003). The bremen earth system model of intermediate complexity (bremic) designed for long-term climate studies. model description, climatology, and applications. *Technical Report, Bremen University, Bremen, Germany.*

Lohmann, K., Drange, H., and Bentsen, M. (2009). Response of the north atlantic subpolar gyre to persistent north atlantic oscillation like forcing. *Climate dynamics*, 32(2-3):273–285.

Lozier, M. S. and Stewart, N. M. (2008). On the temporally varying northward penetration of mediterranean overflow water and eastward penetration of labrador sea water. *Journal of Physical Oceanography*, 38(9):2097–2103.

Luo, D., Zhu, Z., Ren, R., Zhong, L., and Wang, C. (2010). Spatial pattern and zonal shift of the north atlantic oscillation. part i: A dynamical interpretation. *Journal of Atmospheric Sciences*, 67(9):2805–2826.

Luo, H., Castelao, R. M., Rennermalm, A. K., Tedesco, M., Bracco, A., Yager, P. L., and Mote, T. L. (2016). Oceanic transport of surface meltwater from the southern greenland ice sheet. *Nature Geoscience*, 9(7):528–532.

Madec, G., Bourdallé-Badie, R., Bouttier, P.-A., Bricaud, C., Bruciaferri, D., Calvert, D., Chanut, J., Clementi, E., Coward, A., Delrosso, D., et al. (2017). Nemo ocean engine.

Mann, H. B. (1945). Nonparametric tests against trend. *Econometrica: Journal of the econometric society*, pages 245–259.

Marotzke, J. and Willebrand, J. (1991). Multiple equilibria of the global thermohaline circulation. *Journal of physical oceanography*, 21(9):1372–1385.

Martin, S. (2014). *An introduction to ocean remote sensing*. Cambridge University Press.

Marullo, S., Artale, V., and Santoleri, R. (2011). The sst multidecadal variability in the atlantic–mediterranean region and its relation to amo. *Journal of Climate*, 24(16):4385–4401.

Marzocchi, A., Hirschi, J. J.-M., Holliday, N. P., Cunningham, S. A., Blaker, A. T., and Coward, A. C. (2015). The north atlantic subpolar circulation in an eddy-resolving global ocean model. *Journal of Marine Systems*, 142:126–143.

McWilliams, J. C. (2016). Submesoscale currents in the ocean. *Proceedings of the Royal Society A: Mathematical, Physical and Engineering Sciences*, 472(2189):20160117.

Mecking, J., Drijfhout, S., Jackson, L., and Andrews, M. (2017). The effect of model bias on atlantic freshwater transport and implications for amoc bi-stability. *Tellus A: Dynamic Meteorology and Oceanography*, 69(1):1299910.

Meyssignac, B., Boyer, T., Zhao, Z., Hakuba, M. Z., Landerer, F. W., Stammer, D., Köhl, A., Kato, S., L'ecuyer, T., Ablain, M., et al. (2019). Measuring global ocean heat content to estimate the earth energy imbalance. *Frontiers in Marine Science*, 6:432.

Millero, F. J. (2010). History of the equation of state of seawater. *Oceanography*, 23(3):18–33.

Moat, B. I., Smeed, D. A., Frajka-Williams, E., Desbruyères, D. G., Beaulieu, C., Johns, W. E., Rayner, D., Sanchez-Franks, A., Baringer, M. O., Volkov, D., et al. (2020). Pending recovery in the strength of the meridional overturning circulation at 26° n. *Ocean Science*, 16(4):863–874.

Monahan, A. H., Alexander, J., and Weaver, A. J. (2008). Stochastic models of the meridional overturning circulation: time scales and patterns of variability. *Philosophical Transactions of the Royal Society A: Mathematical, Physical and Engineering Sciences*, 366(1875):2525–2542.

Nikurashin, M. and Ferrari, R. (2013). Overturning circulation driven by breaking internal waves in the deep ocean. *Geophysical Research Letters*, 40(12):3133–3137.

Nikurashin, M. and Vallis, G. (2011). A theory of deep stratification and overturning circulation in the ocean. *Journal of Physical Oceanography*, 41(3):485–502.

Nikurashin, M. and Vallis, G. (2012). A theory of the interhemispheric meridional overturning circulation and associated stratification. *Journal of Physical Oceanography*, 42(10):1652–1667.

Oks, D., Mininni, P. D., Marino, R., and Pouquet, A. (2017). Inverse cascades and resonant triads in rotating and stratified turbulence. *Physics of Fluids*, 29(11):111109.

Orszag, S. A. and Patterson Jr, G. (1972). Numerical simulation of three-dimensional homogeneous isotropic turbulence. *Physical Review Letters*, 28(2):76.

Palmer, M., Roberts, C., Balmaseda, M., Chang, Y.-S., Chepurin, G., Ferry, N., Fujii, Y., Good, S., Guinehut, S., Haines, K., et al. (2017). Ocean heat content variability and change in an ensemble of ocean reanalyses. *Climate Dynamics*, 49(3):909–930.

Patterson Jr, G. and Orszag, S. A. (1971). Spectral calculations of isotropic turbulence: Efficient removal of aliasing interactions. *The Physics of Fluids*, 14(11):2538–2541.

Pedlosky, J. (2013). *Geophysical fluid dynamics*. Springer Science & Business Media.

Pekurovsky, D. (2012). P3dfft: A framework for parallel computations of fourier transforms in three dimensions. *SIAM Journal on Scientific Computing*, 34(4):C192–C209.

Perezhogin, P. A. (2020). Testing of kinetic energy backscatter parameterizations in the nemo ocean model. *Russian Journal of Numerical Analysis and Mathematical Modelling*, 35(2):69–82.

Pezzulli, S., Stephenson, D., and Hannachi, A. (2005). The variability of seasonality. *Journal of Climate*, 18(1):71–88.

Pickart, R. S. and Spall, M. A. (2007). Impact of labrador sea convection on the north atlantic meridional overturning circulation. *Journal of Physical Oceanography*, 37(9):2207–2227.

Pohlmann, H., Smith, D. M., Balmaseda, M. A., Keenlyside, N. S., Masina, S., Matei, D., Müller, W. A., and Rogel, P. (2013). Predictability of the mid-latitude atlantic meridional overturning circulation in a multi-model system. *Climate dynamics*, 41(3-4):775–785.

Polo, I., Robson, J., Sutton, R., and Balmaseda, M. A. (2014). The importance of wind and buoyancy forcing for the boundary density variations and the geostrophic component of the amoc at 26° n. *Journal of Physical Oceanography*, 44(9):2387–2408.

Polzin, K. L. and Lvov, Y. V. (2011). Toward regional characterizations of the oceanic internal wavefield. *Reviews of geophysics*, 49(4).

Pope, S. B. (2001). Turbulent flows.

Preisendorfer, R. W. and Mobley, C. D. (1988). Principal component analysis in meteorology and oceanography. *Developments in atmospheric science*, 17.

Putrasahan, D., Lohmann, K., von Storch, J.-S., Jungclaus, J. H., Gutjahr, O., and Haak, H. (2019). Surface flux drivers for the slowdown of the atlantic meridional overturning circulation in a high-resolution global coupled climate model. *Journal of Advances in Modeling Earth Systems*, 11(5):1349–1363.

Rahmstorf, S. (1995). Bifurcations of the atlantic thermohaline circulation in response to changes in the hydrological cycle. *Nature*, 378(6553):145–149.

Rahmstorf, S. (1996). On the freshwater forcing and transport of the atlantic thermohaline circulation. *Climate Dynamics*, 12(12):799–811.

Robson, J., Hodson, D., Hawkins, E., and Sutton, R. (2014). Atlantic overturning in decline? *Nature Geoscience*, 7(1):2–3.

Robson, J., Ortega, P., and Sutton, R. (2016). A reversal of climatic trends in the north atlantic since 2005. *Nature Geoscience*, 9(7):513–517.

Robson, J., Sutton, R., Lohmann, K., Smith, D., and Palmer, M. D. (2012). Causes of the rapid warming of the north atlantic ocean in the mid-1990s. *Journal of Climate*, 25(12):4116–4134.

Roquet, F., Madec, G., Brodeau, L., and Nycander, J. (2015). Defining a simplified yet "realistic" equation of state for seawater. *Journal of Physical Oceanography*, 45(10):2564–2579.

Sandström, J. W. (1908). *Dynamische versuche mit meerwasser*.

Schroeder, K., Chiggiato, J., Bryden, H., Borghini, M., and Ismail, S. B. (2016). Abrupt climate shift in the western mediterranean sea. *Scientific reports*, 6(1):1–7.

Sen, P. K. (1968). Estimates of the regression coefficient based on kendall's tau. *Journal of the American statistical association*, 63(324):1379–1389.

Seneviratne, S., Nicholls, N., Easterling, D., Goodess, C., Kanae, S., Kossin, J., Luo, Y., Marengo, J., McInnes, K., Rahimi, M., et al. (2012). Changes in climate extremes and their impacts on the natural physical environment.

Smith, L. M., Chasnov, J. R., and Waleffe, F. (1996). Crossover from two-to three-dimensional turbulence. *Physical review letters*, 77(12):2467.

Smith, L. M. and Waleffe, F. (1999). Transfer of energy to two-dimensional large scales in forced, rotating three-dimensional turbulence. *Physics of fluids*, 11(6):1608–1622.

Smith, L. M. and Waleffe, F. (2002). Generation of slow large scales in forced rotating stratified turbulence. *Journal of Fluid Mechanics*, 451(1):145–168.

Spence, J. P., Eby, M., and Weaver, A. J. (2008). The sensitivity of the atlantic meridional overturning circulation to freshwater forcing at eddy-permitting resolutions. *Journal of Climate*, 21(11):2697–2710.

Stendardo, I., Rhein, M., and Hollmann, R. (2016). A high resolution salinity time series 1993–2012 in the north atlantic from argo and altimeter data. *Journal of Geophysical Research: Oceans*, 121(4):2523–2551.

Stommel, H. (1948). The westward intensification of wind-driven ocean currents. *Eos, Transactions American Geophysical Union*, 29(2):202–206.

Stommel, H. (1961). Thermohaline convection with two stable regimes of flow. *Tellus*, 13(2):224–230.

Storto, A., Alvera-Azcárate, A., Balmaseda, M. A., Barth, A., Chevallier, M., Counillon, F., Domingues, C. M., Drevillon, M., Drillet, Y., Forget, G., et al. (2019). Ocean reanalyses: recent advances and unsolved challenges. *Frontiers in Marine Science*, 6:418.

Storto, A., Yang, C., and Masina, S. (2016). Sensitivity of global ocean heat content from reanalyses to the atmospheric reanalysis forcing: A comparative study. *Geophysical Research Letters*, 43(10):5261–5270.

Straneo, F. (2006). On the connection between dense water formation, overturning, and poleward heat transport in a convective basin. *Journal of Physical Oceanography*, 36(9):1822–1840.

Swingedouw, D., Braconnot, P., and Marti, O. (2006). Sensitivity of the atlantic meridional overturning circulation to the melting from northern glaciers in climate change experiments. *Geophysical research letters*, 33(7).

Talley, L. D. (2011). *Descriptive physical oceanography: an introduction*. Academic press.

Tietsche, S., Balmaseda, M., Zuo, H., Roberts, C., Mayer, M., and Ferranti, L. (2020). The importance of north atlantic ocean transports for seasonal forecasts. *Climate Dynamics*, 55(7):1995–2011.

Treasure, A. M., Roquet, F., Ansorge, I. J., Bester, M. N., Boehme, L., Bornemann, H., Charrassin, J.-B., Chevallier, D., Costa, D. P., Fedak, M. A., et al. (2017). Marine mammals exploring the oceans pole to pole: a review of the meop consortium. *Oceanography*, 30(2):132–138.

Trenary, L. and DelSole, T. (2016). Does the atlantic multidecadal oscillation get its predictability from the atlantic meridional overturning circulation? *Journal of Climate*, 29(14):5267–5280.

Tziperman, E., Toggweiler, J., Bryan, K., and Feliks, Y. (1994). Instability of the thermohaline circulation with respect to mixed boundary conditions: Is it really a problem for realistic models? *Journal of Physical Oceanography*, 24(2):217–232.

Vallis, G. K. (2019). *Essentials of atmospheric and oceanic dynamics*. Cambridge University Press.

Wang, Z., Brickman, D., and Greenan, B. J. (2019). Characteristic evolution of the atlantic meridional overturning circulation from 1990 to 2015: An eddy-resolving ocean model study. *Deep Sea Research Part I: Oceanographic Research Papers*, 149:103056.

Weijer, W., Cheng, W., Drijfhout, S. S., Fedorov, A. V., Hu, A., Jackson, L. C., Liu, W., McDonagh, E., Mecking, J., and Zhang, J. (2019). Stability of the atlantic meridional overturning circulation: A review and synthesis. *Journal of Geophysical Research: Oceans*, 124(8):5336–5375.

Willis, J. K., Roemmich, D., and Cornuelle, B. (2004). Interannual variability in upper ocean heat content, temperature, and thermosteric expansion on global scales. *Journal of Geophysical Research: Oceans*, 109(C12).

WMO (2017). Wmo guidelines on the calculation of climate normals.

Wood, R. A., Rodríguez, J. M., Smith, R. S., Jackson, L. C., and Hawkins, E. (2019). Observable, low-order dynamical controls on thresholds of the atlantic meridional overturning circulation. *Climate Dynamics*, 53(11):6815–6834.

Wunsch, C. (2005). Thermohaline loops, stommel box models, and the sandström theorem. *Tellus A: Dynamic Meteorology and Oceanography*, 57(1):84–99.

Wunsch, C. and Ferrari, R. (2004). Vertical mixing, energy, and the general circulation of the oceans. *Annu. Rev. Fluid Mech.*, 36:281–314.

Yang, C., Leonelli, F. E., Marullo, S., Artale, V., Beggs, H., Nardelli, B. B., Chin, T. M., De Toma, V., Good, S., Huang, B., et al. (2021). Sea surface temperature intercomparison in the framework of the copernicus climate change service (c3s). *Journal of Climate*, 34(13):5257–5283.

Yang, J. (2015). Local and remote wind stress forcing of the seasonal variability of the atlantic meridional overturning circulation (amoc) transport at 26.5 n. *Journal of Geophysical Research: Oceans*, 120(4):2488–2503.

Yashayaev, I. (2007). Hydrographic changes in the labrador sea, 1960–2005. *Progress in Oceanography*, 73(3-4):242–276.

Zhang, R., Sutton, R., Danabasoglu, G., Kwon, Y.-O., Marsh, R., Yeager, S. G., Amrhein, D. E., and Little, C. M. (2019). A review of the role of the atlantic meridional overturning circulation in atlantic multidecadal variability and associated climate impacts. *Reviews of Geophysics*, 57(2):316–375.

Zuo, H., Balmaseda, M. A., Mogensen, K., and Tietsche, S. (2018). *OCEAN5: the ECMWF Ocean Reanalysis System and its Real-Time analysis component*. European Centre for Medium Range Weather Forecasts.

Zuo, H., Balmaseda, M. A., Tietsche, S., Mogensen, K., and Mayer, M. (2019). The ecmwf operational ensemble reanalysis–analysis system for ocean and sea ice: a description of the system and assessment. *Ocean Science*, 15(3).